UNIVERSITY OF CALIFORNIA,
IRVINE

Predicting Phase State and Viscosity of Secondary Organic Material and Their Impact on Amine Uptake by Atmospheric Particles

DISSERTATION

submitted in partial satisfaction of the requirements
for the degree of

DOCTOR OF PHILOSOPHY

in Chemistry

by

Wing-Sy Wong DeRieux

Dissertation Committee:
Associate Professor Manabu Shiraiwa, Chair
Professor James N. Smith
Professor Sergey Nizkorodov

2019

DEDICATION

To Charlie and Drew for all their love, support and perspective
during the long days and endless nights

"If you aren't in over your head, how do you know how tall you are?"
-T.S. Eliot

"In order to arrive there,
To arrive where you are, to get from where you are not,
You must go by a way wherein there is no ecstasy.
In order to arrive at what you do not know
You must go by a way which is the way of ignorance.
In order to possess what you do not possess
You must go by the way of dispossession.
In order to arrive at what you are not
You must go through the way in which you are not.
And what you do not know is the only thing you know
And what you own is what you do not own
And where you are is where you are not."

-T.S. Eliot, Four Quartets

"Nevertheless, she persisted"
-Senator Mitch McConnell referring to Senator Elizabeth Warren

TABLE OF CONTENTS

Page

LIST OF FIGURES

Page

LIST OF TABLES

Page

ACKNOWLEDGMENTS

I would like to express my deepest and most heartfelt appreciation to my committee chair, Professor Manabu Shiraiwa. His boundless energy, insight, brilliance and dedication are impossible to miss. Without his support, persistent help and determination to challenge his students, this dissertation would not have been possible.

I would like to thank my committee members, Professor Sergey Nizkorodov and Professor James N. Smith, who held me to high standards, and pushed me to improve and consider the impact of my work. In addition to being exceptional scientists and faculty members, I also found them to be truly admirable people who care about everyone in our community.

The work presented in this dissertation is truly a collaborative effort. My contributions would not have been possible without the work of our collaborators: Professor Julia Laskin, Professor Alexander Laskin, Professor Allan K. Bertram, Professor Chak K. Chan, Professor Andreas Zuend, Dr. Sandra L. Blair, Dr. Yangxi Chu, Dr. Peng Lin, Dr. Mijun Song, Hayley S. Glicker, Yuanzhou Huang, Adrian M. Maclean, and Natalie R. Smith. It was a pleasure and a privilege to work with each of you.

In addition, thank you to Dr. Pascale Lakey and Dr. Ying Li who patiently – and seemingly effortlessly – provided everyday guidance and support in addition to inspiring me with their knowledge and work ethic. Thank you also to the other members of the Shiraiwa group, Brian Hwang, Ting Fang and Jin-Lai Wei who were always available for questions, discussion, and tips about great restaurants.

My deepest appreciation to my husband and son (Drew and Charlie), my parents (Cho-Mei and Kwan-Hung) and extended family (Brenda, Chuck and Margaret) for all their love and support. I am also incredibly grateful for friends, near and far who provided support through this very long and intense process. This dissertation would not have been possible without you.

An important thank you to Professor Yann Schrodi, who helped me make the transition back to full-time student and was a very supportive master's thesis advisor at CSUN. Finally, thank you to Mr. McCluskey and Mr. McElroy at Conestoga Senior High School who first introduced me to physics and chemistry so many years ago.

I thank the Proceedings of the National Academy for Sciences, the American Chemical Society and Copernicus Publications for permission to include copyrighted figures as part of my dissertation. I also thank Copernicus Publications for permission to include chapter two of my dissertation, which was originally published in Atmospheric Chemistry and Physics, and chapter four, which has been published in Atmospheric Chemistry and Physics Discussions. Financial support was provided by the Department of Energy (DE-SC0018349) and the University of California, Irvine, the National Science Foundation (AGS-1654104).

CURRICULUM VITAE

EDUCATION

University of California	Ph.D.	Chemistry	Irvine, CA	2019
California State University	M.S.	Chemistry	Northridge, CA	2013
Harvard University	A.B.	Physics	Cambridge, MA	1995

RESEARCH AND TEACHING EXPERIENCE

UCI Department of Chemistry Irvine, CA
Ph.D. Research January 2017-June 2019
Advisor: Manabu Shiraiwa. Review literature and analyze experimental data to construct kinetic models for formation of secondary organic aerosols and multiphase atmospheric processes. Experience with Matlab and Igor Pro.

UCI Department of Chemistry Irvine, CA
Ph.D. Research January 2014-December 2016
Advisor: Alan Heyduk. Utilized organic and inorganic synthetic techniques to synthesize coordination complexes stabilized by redox-active pincer ligands. Analyzed results using multinuclear NMR, EPR, single crystal X-ray crystallography, UV/Vis/NIR, FTIR and electrochemical experiments. Experienced with Turbomole, Easyspin, glove box and Schlenk techniques.

UCI Department of Chemistry Irvine, CA
General Chemistry (H2LA, H2B, 1A, 1C), Teaching Assistant September 2013
Organic Chemistry (51A, 51LB, 51LC), Teaching Assistant -December 2016
Reviewed course concepts. Oversaw, instructed and graded students on laboratory techniques.

CSUN Department of Chemistry and Biochemistry Northridge, CA
Master's Thesis Research June 2009-June 2013
Advisor: Yann Schrodi. Utilized organic and inorganic synthetic techniques to access new coordination and organometallic compounds stabilized by pincer ligand systems. Analyze results using multinuclear NMR, single crystal X-ray crystallography and FTIR. Experience with glove box and Schlenk techniques.

CSUN Department of Chemistry and Biochemistry Northridge, CA
Inorganic Chemistry (401L), Teaching Assistant January 2012-May 2012
Supervised, instructed and graded students in inorganic synthesis and characterization techniques.

CSUN Department of Chemistry and Biochemistry Northridge, CA
Organic Chemistry II (334L), Teaching Assistant January 2010-June 2013
Organic Chemistry I (333L), Teaching Assistant September 2010-June 2013
Supervised, instructed and graded students in organic synthesis and characterization techniques.

PUBLICATIONS

Song, M.; Maclean, A. M.; Huang, Y.; Smith, N. R.; Blair, S. L.; Laskin, J.; Laskin, A.; DeRieux, W.S.W.; Li, Y.; Shiraiwa, M.; Nizkorodov, S. A.; Bertram, A. K.: Liquid-liquid phase separation and viscosity within secondary organic aerosol generated from diesel fuel vapors, Atmos. Chem. Phys. Discuss., in review, 2019.

DeRieux, W.S.W.; Li, Y.; Lin, P.; Laskin, J.; Laskin, A.; Bertram, A. K.; Nizkorodov, S. A.; Shiraiwa, M.: Predicting the glass transition temperature and viscosity of secondary organic material using molecular composition, Atmos. Chem. Phys., 18, 6331-6351, 2018.

DeRieux, W.S.W.; Wong, A.; Schrodi, Y.: Synthesis and characterization of iron complexes based on bis-phosphinite PONOP and bis-phosphite PONOP pincer ligands. J. Organomet. Chem., 772-773, 60-67, 2014.

PRESENTATIONS/POSTERS

"Predicting the glass transition temperature and viscosity of secondary organic material using molecular composition." W. -S. W. DeRieux, Y. Li, P. Lin, J. Laskin, A. Laskin, A. K. Bertram, S. A. Nizkorodov and M. Shiraiwa. 35th Informal Symposium on Kinetics and Photochemical Processes in the Atmosphere in Pasadena, CA, March 30, 2018, *Poster*.

"Predicting the glass transition temperature and viscosity of secondary organic material using molecular composition." W. -S. W. DeRieux, Y. Li, P. Lin, J. Laskin, A. Laskin, A. K. Bertram, S. A. Nizkorodov and M. Shiraiwa. UC Chemical Symposium in Lake Arrowhead, CA, March 26-28, 2018, *Poster*.

"Predicting the glass transition temperature and viscosity of secondary organic material using molecular composition." W. -S. W. DeRieux, Y. Li, P. Lin, J. Laskin, A. Bertram, S. Nizkorodov and M. Shiraiwa. 36th AAAR Annual Conference in Raleigh, NC. October 16-20, 2017, *Poster*.

"Studies of iron coordination with bis-phosphinite PONOP and bis-phosphite PONOP pincer ligands: Toward the development of iron alkylidene complexes." W. DeRieux and Y. Schrodi, 244th ACS National Meeting in Philadelphia, PA, August 19, 2012, *Presentation*.

"Finding Alternatives to Ruthenium for Olefin Metathesis Catalysts." W. W. DeRieux and Y. Schrodi. CSUN 15th Annual Student Research & Creative Works Symposium in Northridge, CA, February 18, 2011, *Presentation.*

OTHER RESEARCH EXPERIENCE

National Optical Astronomy Observatory Tucson, AZ
Research Assistant, Research Experiences for Undergraduates June 1994-August 1994
Advisor: David De Young. Analyzed data from the Hubble Space Telescope for creation of a mathematical model of the elliptical galaxy NGC6251.

Harvard-Smithsonian Center for Astrophysics Cambridge, MA
Research Assistant June 1992-May 1994
Advisor: Jonathan E. Grindlay. Constructed key components of a balloon-borne hard X-ray-imaging telescope and performed data analysis.

HONORS/AWARDS

Graduate Opportunity Fellowship, UCI Graduate Division, 2013-2018.
Competitive Edge participant, UCI Graduate Division, Summer 2013.
Honorable Mention, California Pre-Doctoral Scholarship Program, August 2012.
Outstanding Graduate Teaching Assistant, CSUN Dept of Chemistry and Biochemistry, 2012.
Thesis Support Award, CSUN Office of Graduate Studies, December 2010.

OTHER EXPERIENCE

Infusion Systems, LLC Sylmar, CA
Engineer September 2004-June 2009
Oversaw pharmaceutical compatibility and biocompatibility studies for an implantable pain medication pump. Analyzed results using HPLC, ICP-MS, SEM/EDX and FTIR. Performed in-house materials testing according to ASTM international standards. Wrote validation reports for submission to the FDA.

The School for Field Studies Salem, MA
Institutional Relations Manager July 2002-February 2004
Coordinated institutional outreach and support for an international environmental field research and education non-profit organization.

Harvard Law School Cambridge, MA
Administrative Assistant, Graduate Program October 1996-March 2002
Provided program and administrative support to an academic office serving international students and visiting scholars. Screened applications to the Master's Program. Coordinated student orientation and weekly colloquium series.

City Year Boston, MA
Corps Member September 1995-June 1996
Created and coordinated science curriculum for students in an urban fifth grade classroom while serving full-time in Boston's urban youth corps. Completed community and school improvement projects as part of a diverse team of ten volunteers.

ABSTRACT OF THE DISSERTATION

Predicting Phase State and Viscosity of Secondary Organic Material
and Their Impact on Amine Uptake by Atmospheric Particles

By

Wing-Sy Wong DeRieux

Doctor of Philosophy in Chemistry

University of California, Irvine, 2019

Associate Professor Manabu Shiraiwa, Chair

Atmospheric aerosol particles affect air pollution, public health, and radiative forcing of climate. Their phase state and morphology have far ranging effects on gas uptake, particle phase rate of reaction and aging. Recent reports have demonstrated that atmospheric particles may exist in semi–solid or glassy solid states. The phase transition between these two states occurs at the glass transition temperature (T_g). The goal of Chapters 2 and 4 of this work was to predict the phase state and viscosity of secondary organic aerosol (SOA) mixtures. A modeling approach to predict viscosity as a function of ambient temperature and relative humidity (RH) that uses a parameterization for estimating T_g of organic compounds from molecular composition is presented. The method is applied to α–pinene and isoprene SOA using marker compounds and toluene and diesel-derived SOA using high–resolution mass spectrometry (HRMS) data. Predictions agree well with measured viscosities. Finally, the viscosity of biomass burning SOA is predicted with two sets of HRMS data collected using different ionization techniques, electrospray ionization and atmospheric pressure photoionization, on the same samples. The use of different ionization techniques leads to a difference of ~10^2 in predicted viscosity at low RH.

Next, measurements of the reactive uptake of dimethylamine (DMA) by ammonium sulfate (AS) and mixed AS–sucrose particles at different RH are simulated with the kinetic multi–layer model of gas particle interactions (KM-GAP) in Chapter 3. Investigations into the role of amines in new particle formation and nano–particle growth are essential to our understanding of cloud condensation nuclei. KM-GAP is well suited to elucidating the mechanisms underlying amine uptake as it explicitly treats the temporal evolution of all species from the gas phase to the particle. Particle mass growth over time and its humidity dependence is successfully reproduced for all experimental samples. Uptake in the mixed AS–sucrose particles is limited by diffusion of DMA and AS through a viscous sucrose–rich shell at lower RH. Uptake coefficients increase when RH increases, but decrease when the molar fraction of sucrose increases at fixed RH. The model is extrapolated to emulate atmospheric conditions. At RH greater than or equal to 70% for liquid particles, amine uptake can lead to a mass increase of approximately 20 to 60%.

Chapter 1

INTRODUCTION

1.1: Overview of troposphere and atmospheric aerosols

Characterization of atmospheric aerosol particles in the troposphere is a major research focus due to their contribution to air pollution and health effects, and uncertainty about the impact of atmospheric particles on radiative forcing.[15-18] Extending approximately 10-15 km above the Earth's surface, the troposphere is the lowest layer of the atmosphere and has the most direct impact on life on Earth. Humans experience conditions in the troposphere as weather and climate. In addition to the primary gaseous components (N_2, O_2, argon and CO_2) that comprise over 99.9% of dry air, the troposphere contains trace gases, particles, and emissions from both biogenic processes, related to animals and vegetation, and anthropogenic sources such as automobiles and power plants.[19, 20]

Many components of the troposphere comprise more than one phase and can be described collectively as aerosols, a term which refers to a heterogeneous system in which condensed phase particles are dispersed throughout a gas.[21] The particles are small – ranging in size from a few nanometers to tens of micrometers in diameter – and their physical properties are influenced by ambient temperature, relative humidity, solar radiation and other environmental factors. Additionally, the composition of the aerosol particles can be altered by heterogeneous reactions between the gas and condensed phases.[22]

Depending on their size, aerosol particles may remain suspended in the air for hours or days. As such, they can be inhaled or ingested by humans and other animals and this exposure can negatively affect respiratory and cardiovascular systems, contributing to allergies, lung cancer and other diseases.[19, 23, 24] Particles in the atmosphere also scatter or absorb light and can significantly reduce visibility, creating phenomenon such as urban haze.[15, 25, 26] The ability of aerosols to affect the passage of light is at the heart of why aerosol particles are an important

consideration in how the Earth's atmosphere interacts with solar radiation. In general, aerosol particles are reflective, and will direct incoming light from the sun back out into space.[17, 18, 27] If aerosol particles contain compounds that absorb light, however, such as the organic compounds referred to as 'brown carbon,' they will absorb solar radiation, leading to an increase in the temperature of the atmosphere and a positive radiative forcing effect.[28-30] Aerosol particles can also act as nuclei for ice and cloud condensation, influencing weather and cloud formation, but also interact with both solar and long wave radiation.[1, 31-33]

Aerosol particles are frequently a mixture of inorganic and organic components.[22, 34] The main inorganic components are salts of ammonium (NH_4^+) and sodium (Na^+) with sulfate (SO_4^{2-}), nitrate (NO_3^-) and chloride (Cl^-) originating from dust, soot and minerals in sea spray. For atmospheric aerosol particles with diameters smaller than 1 μm, it is estimated that organic compounds can account for 50-90% of the mass.[35, 36] Directly emitted organics, or primary organics, are volatile organic compounds (VOCs) emitted directly from sources. Primary organics may undergo gas–phase oxidation, oligomer formation in the particle phase, degradation or other types of transformation to form secondary organics. If secondary organics are sufficiently oxidized, their volatility may become low enough to also enter the condensed phase leading to the formation of secondary organic aerosols (SOAs).[1]

1.2: Aerosol particle phase state

Recently reported experimental observations of laboratory–generated and collected ambient aerosol particles have demonstrated that atmospheric aerosol particles are likely to exist in semi–solid or glassy solid states.[9, 10, 37-41] The condensed phase of an aerosol can range from

liquid droplets to semi–solid or solid particles and the composition and consistency may vary depending on the precursor, geographic location and time of day.[1, 34, 42] If aerosol particles are liquid, thermodynamic factors will be the primary influence in uptake, diffusion and partitioning processes.[43, 44] The liquid phase is characterized by dynamic viscosity (η) values below 10^2 Pa s. In this regime, aerosol particles would be expected to exhibit mixing times in the range of 10^{-3}–10^{-9} seconds and the partitioning of oxidation products between the gas and particle phases would reach equilibrium almost instantaneously (Figure 1.1).[45]

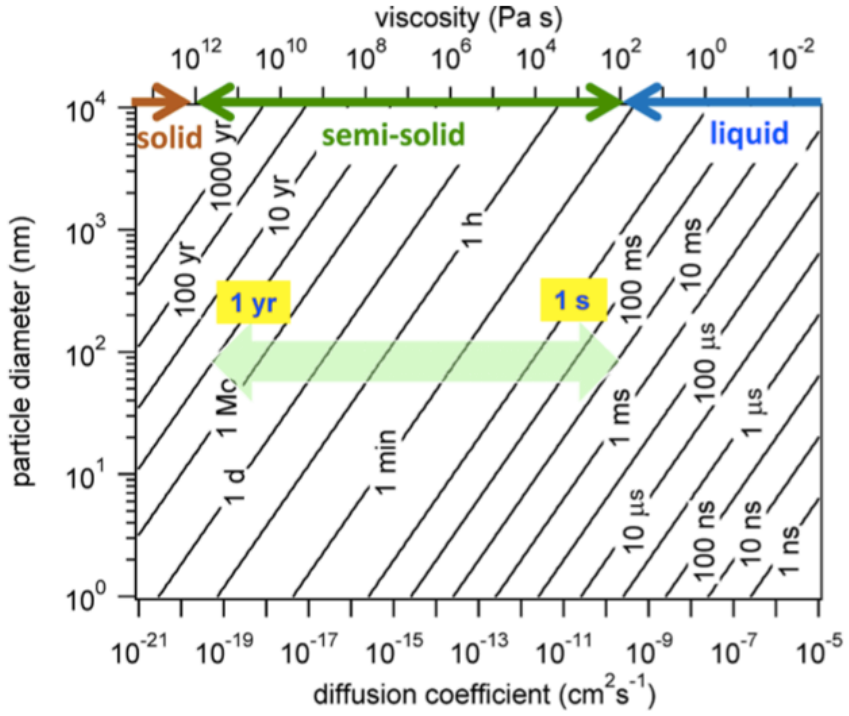

Figure 1.1. Characteristic time of bulk diffusion (τ_{cd}) in liquid, semi-solid, and solid particles as a function of diffusion coefficient and particle diameter. In the size range of the atmospheric aerosol accumulation mode ($d_p = 10^2$ nm), τ_{cd} in semi-solid particles varies from seconds to year (light green arrow). Reproduced from Shiraiwa et al., (2011).[1]

In the semi–solid ($10^2 < \eta < 10^{12}$) and solid ($\eta > 10^{12}$) phases, however, viscosity increases dramatically and characteristic mixing times extend by orders of magnitude to minutes (~10^2 s) and years (~10^7 s). Solid particles in the atmosphere may take crystalline form or appear glassy. Because of the many compounds present in SOA, crystalline solids are less likely to develop.[5, 35, 37, 46] Instead, such mixtures tend to form glasses: non–ordered amorphous solids that

are distinguished from semi–solids or liquids by their high viscosity ($\eta > 10^{12}$ Pa s) and physical characteristics that make them appear solid.[5, 47] Crystalline solids go through a first–order phase transition to reach a state of thermodynamic equilibrium with the accompanying liquid phase. Glass formation, however, is a non-equilibrium process in which the molecular motion of a compound slows as the temperature lowers to the point where translational motion (flow) and diffusion through the compound decrease signifcantly.[5]

Glasses exhibit the mechanical properties of solids, but unlike a crystalline solid, there is no long–range order in a glass. Well mixed, low viscosity, liquid particles are ergodic systems, meaning that collecting data on a number of points throughout the particle will provide equivalent information to collecting data for a single point in the system over an extended period of time.[48, 49] In such conditions, each molecule has the translational freedom to flow to any point within the particle. When glass formation occurs, flow is restricted as the system becomes non-ergodic. This loss of ergodicity is one of the defining characteristics of a

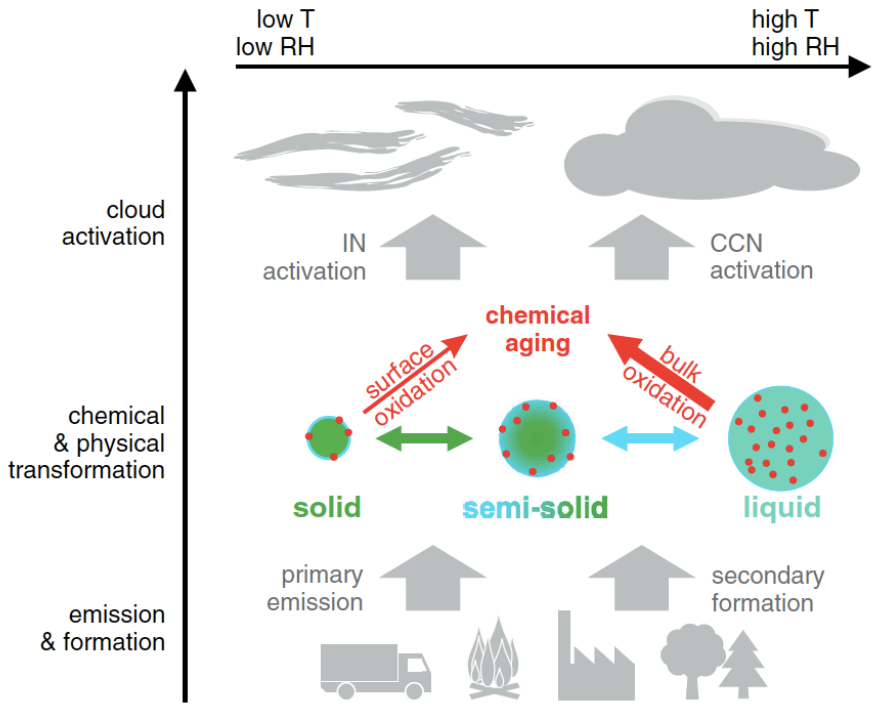

Figure 1.2. The phase state of amorphous organic aerosol varies depending on environmental conditions and source. Oxidation leads to chemical aging. Aged aerosol particles may participate in cloud activation or nucleate ice. Reproduced from Shiraiwa et al., (2011).[1]

glass. Translational motion could still occur over a sufficiently long time period. In addition, because a glass is not in a state of thermodynamic equilibrium, glass formation is heavily influenced by kinetic factors, such as the rate at which a particle is cooled or heated. The composition of the particle is also extremely important as the temperature range at which glass formation occurs and the rate at which viscosity changes around the glass transition temperature (T_g) varies between compounds.[50] The presence of compounds that form glasses at relatively low temperatures, such as water, will significantly affect the glass formation of a mixture.[51]

Aerosol particle morphology and the partitioning of components may also affect interactions between the gas and particle phases. Traditionally, atmospheric particles were assumed to be homogeneous and well–mixed. However, phase separation has been reported for aerosol particles, including liquid–liquid phase separation. The most likely morphologies are core–shell, in which one phase completely engulfs the other, and partially engulfed, where both phases are in contact with each other and the gas phase. Data consistent with phase separation has been reported for mixed particles containing inorganic and organic components as well as electrolyte–free organic particles.[52-55] The morphology of a particle is determined by the relative surface tensions of the phases in contact with each other, which are, in turn, heavily influenced by particle composition and water content.[20] The low surface tension organic phase is often observed forming the outer phase of core–shell particles. Consequently, gas uptake and bulk diffusion experiments have been reported with SOA coatings on cores ranging from water to inorganic salts.[56-58] The overall effect of morphology on gas–particle processes is not yet clear and may be heavily reliant on composition and water content of the particle.

The phase state and morphology of aerosol particles can have important and far–ranging effects. Slower diffusion in the particle phase will affect gas uptake and the rate of reactions in

the particle, affecting the composition, mass and growth of aerosol particles with important implications for their mass and size distributions. Decreased diffusion also can affect aging reactions (Figure 1.2), gas–particle equilibrium partitioning and the composition of the gas phase.[59, 60] In addition, organic components in particles that have higher viscosity or core–shell morphology may be shielded from atmospheric oxidants, extending their lifetimes and allowing them to undergo long–range transport.[61, 62] Finally, aerosol particle phase state and composition will affect physical properties that determine the role aerosols play in ice nucleation and liquid cloud droplet activation processes (Figure 1.2).[32]

Despite the substantial implications of SOA particle phase state, its variations and effects have not been considered explicitly in current air quality models. The Shiraiwa group has targeted development of a bottom–up modeling approach to predict the viscosity – and hence the phase state – of aerosol particles as a function of ambient temperature (T) and relative humidity (RH). Such a method could then be implemented in regional or global air quality models for simulating the distribution of SOA phase state in the atmosphere.

1.3: Parameterizations and modeling

Often, simplifying assumptions must be made when investigating a complex system of reactions or compounds. A common approach used is to introduce a parameterization—a mathematical equation or set of equations that can be used to generate approximate values for a quantity of interest in the system that is challenging or time–consuming to determine otherwise. The equation(s) may be derived from the extrapolation of basic physical principles for similar systems as in the case of cloud parameterizations used in global atmospheric models,[63] or generated through numerical fitting of a representative dataset as demonstrated in the

development of parameterizations to predict saturation mass concentration of organic compounds.[64] The independent variables in these equations are referred to as parameters and are fewer than the true number of variables in the real world system. Since the parameterization relies on fewer variables, its use decreases the complexity of the system, which is advantageous if the approximate values generated are reasonably accurate.

A closely related approach is the development of a model. Models are collections of mathematical equations that describe multiple variables of interest in a system. These equations may include parameterizations and/or known equations for basic physical processes. Additionally, the assumptions required to implement the model and boundaries of model application must be expressed mathematically. Thus, a model can be considered a detailed and educated 'guess' for the mechanism behind a physical process. As such, testing the accuracy of the guess by comparing model predictions to a wide range of experimentally–derived data and field measurements is essential to improving model accuracy. Models that have been demonstrated to provide acceptably accurate predictions for a dataset can be used to extrapolate to similar conditions by varying parameters, providing guidance for future experiments to further refine the model's accuracy.[65]

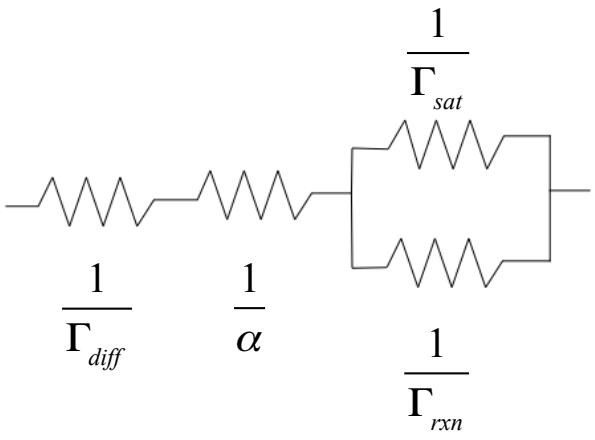

Figure 1.1. Schematic illustrating the resistor model for atmospheric processes. Here, processes considered include gas phase diffusion, surface accommodation, solvation in a liquid particle and bulk reaction. Adapted from Davidovits et al., (2006) Figure 2.[3]

1.4: Atmospheric Modeling

Elucidating the mechanism of heterogeneous atmospheric processes is challenging for multiple reasons. In addition to the large number of atmospheric species and physical processes that must be considered, the timescales associated with a particular species or process may span a wide range. On one end of this range are timescales less than a second, such as the desorption lifetime of the major atmospheric oxidant, OH, which is predicted to be approximately 10 nanoseconds ($\tau_d = 1\times10^{-8}$ s).[66] On the other end are timescales of days, months or years, such as the lifetime of peroxyacetylnitrate reservoir (PAN) due to thermal decomposition, which can vary between 1 hour (3.6×10^4 s) to months (60 days = 5.2×10^6 s) depending on ambient temperature.[67, 68]

Atmospheric processes can be represented as sets of differential equations, with physical quantities varying with time. For systems of related processes, the equations for some processes may contain more than one variable because other processes affect them. In such cases, the differential equation for those processes will contain variables that are dependent variables in other equations. Such systems of differential equations are described as 'coupled.' Coupled differential equations are usually too complex to solve directly and require a numerical approach with a computational solver program. However, given the wide range of timescales encountered in atmospheric processes, these systems are often 'stiff' meaning that the correct solution is very close numerically to incorrect solutions. In this situation, if the solver encounters an incorrect solution, it will be led away from the correct solution, greatly increasing the solving time and computational cost.[69] For this reason, small time steps must be used and computing a detailed simulation of a dynamic atmospheric process can be extremely challenging.

Another major challenge to the study of atmospheric processes is the need to consider reactions and processes between components in different phases. The study of heterogeneous reactions and processes has lagged significantly behind that of homogeneous liquid or gas systems. Much of the recent progress has been driven by the needs of atmospheric science and was aided by the application of the resistor model approach (Figure 1.3).[3]

The work of Danckwerts and Schwartz formed the basis of the resistor model.[70,3] Danckwerts derived a set of differential equations that could describe the diffusion of a gas into a liquid droplet. His approach assumed that a first–order rate equation could be used if the contact time between the two phases was short and the diffusivity of the droplet was uniform and constant. This approach gave researchers a starting point to calculate uptake of a gaseous species by a liquid droplet.

The formal resistor model was introduced by Schwartz and coworkers, who likened atmospheric systems to electrical circuits where individual processes acted as sources of 'resistance' to the uptake (γ) of a gaseous species.[3] The inverse of the uptake coefficient for a process provides a numerical value for the resistance. By assuming steady state conditions, a sequence of atmospheric processes could be decoupled and treated as resistive elements in series or in parallel. As illustrated in Figure 1.3, during the uptake of a gaseous species, molecules of the gas may diffuse through the gas phase to the particle where a portion of the molecules will collide with the surface of the particle and enter the liquid droplet. This sequence of events is described as gas phase diffusion, for which the resistance term is expressed as $\frac{1}{\Gamma_{diff}}$, and mass accommodation, for which the resistance term is expressed as $\frac{1}{\alpha}$. Once inside the particle, the gas molecules must dissolve in the liquid bulk to diffuse through the particle (solvation, $\frac{1}{\Gamma_{sat}}$) and over time an equilibrium will become established that will affect the previous processes in the

sequence. If the gas molecules react with the particle bulk, this reaction will affect the solvation equilibrium of the gas species, so a term for the bulk reaction ($\frac{1}{\Gamma_{rxn}}$) is added to the resistor model in parallel to the solvation term. Each resistance term affects the uptake of the gaseous species by the liquid droplet and the overall uptake can be described by solving the following equation:

$$\frac{1}{\gamma} = \frac{1}{\Gamma_{diff}} + \frac{1}{\alpha} + \frac{1}{\Gamma_{sat} + \Gamma_{rxn}}$$

Application of the resistor model has enabled researchers to calculate approximate solutions to the differential equations for many atmospheric processes,[58, 71, 72] some with errors of only a few percent compared to numerical solutions.[31]

A number of promising models have been developed using the resistor model to account for the atmospheric chemistry of SOA particles. However, the resistor model is limited by the assumption that atmospheric aerosol particles exist primarily in the liquid phase,[4] exhibit homogeneous mixing, and satisfy the criteria for steady–state or quasi–equilibrium conditions. Such requirements are met for the case of a gas phase reactant interacting with homogeneous, low viscosity, liquid aerosol droplets. In this case, thermodynamic considerations can be used to describe gas particle interactions. If, however, the particle phase state is more viscous or is not homogeneously mixed, as would be the case for semi–solid or solid particles, and for particles that exhibit phase separation,[3, 4, 73, 74] the assumptions required for the resistor model may no longer be valid.

In 2007, Pöschl, Rudich and Ammann introduced a kinetic framework for modeling of atmospheric heterogeneous systems.[75] The PRA framework laid the foundation for a complete kinetic treatment of gas–particle interactions for aerosol and cloud processes and demonstrated that their approach is compatible with the resistor model. Our group has developed kinetic

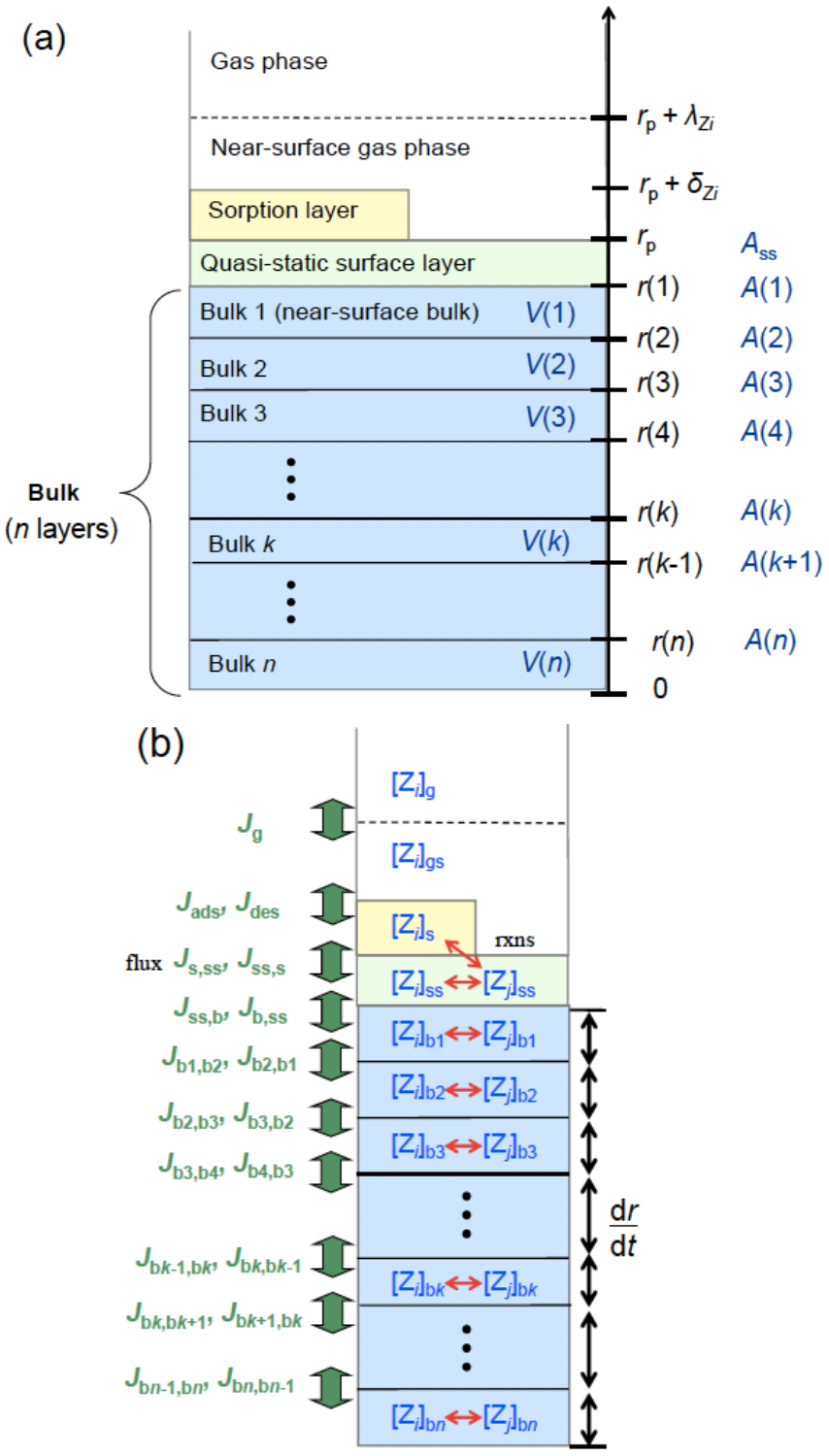

Figure 1.2. Kinetic multi-layer model of gas-phase interactions in aerosols and clouds (KM-GAP). (a) Model compartments and layers with corresponding distances from the particle center (r), surface areas (A), and volumes (V); (b) Transport fluxes (green arrows) and chemical reactions (red arrows). The black arrows indicate that each bulk layer can grow or shrink. (reproduced from Shiraiwa et al., 2012, Figure 1).

models based on the PRA framework, including the kinetic double–layer surface (K2–SURF) model that considers interactions between the gas phase and a surface[73], the kinetic multi–layer model of surface and bulk (KM-SUB) that explicitly considers mass transport and reactions at a particle surface and bulk[74], and the kinetic multi–layer model of gas–particle (KM–GAP) interaction[4].

KM-GAP is the most powerful version of the kinetic models developed by the Shiraiwa group based on the PRA framework. It considers surface and bulk reactions and explicitly treats all mass transport processes from the gas phase to the particle bulk (Figure 1.4). These processes may include: gas–phase diffusion, adsorption and desorption from the surface of the particle, bulk diffusion, condensation, evaporation and heat transfer.[4] The model treats the gas phase with two layers: a quasi–continuous gas phase and a near–surface gas phase layer. Multiple layers represent the condensed phase: sorption layer, quasi–surface layer, and a variable number of bulk layers.

While KM-GAP can be used to simulate the same types of systems as the resistor model, it does not require steady–state conditions and is well–suited for application to simulations of particles that are not homogenous and well–mixed. For every one of the layers, the number of each species is calculated as a function of time and an unlimited number of chemical species can be included in the model. Another key feature of KM-GAP is the ability for the layers to increase and decrease in size to reflect changes in molecular composition as mass transport and chemical reaction(s) occur.[4] As a result, KM-GAP also can be used to simulate changes in particle size over time.

Another advantage of KM-GAP over traditional resistor models is that the particle bulk can be treated with a variable number of layers, enabling users to optimize computational cost

without sacrificing resolution in the particle bulk. Individual terms for mass transport between bulk layers are used to explicitly simulate the change in number of species over time. Bulk diffusion in KM-GAP is treated according to Fick's first law of diffusion in the following form:

$$k_{\mathrm{b,b},Z_i}(k) = \frac{2D_{b,Z_i}}{(\delta(k)+\delta(k+1))}$$

where $k_{b,b,Z_i}(k)$ is the first–order transport rate coefficient for mass transport between bulk layers (molecules cm^{-1} s^{-1}), D_{b,Z_i} is the bulk diffusion coefficient (molecules cm^{-2} s^{-1}) for species Z_i, and $\frac{2}{(\delta(k)+\delta(k+1))}$ is the average distance (cm) travelled by a molecule between bulk layers k and k+1.[4] Mass transport flux (J, molecules cm^{-2} s^{-1}) can then be calculated with $J_{\mathrm{b,b},Z_i} = k_{\mathrm{b,b},Z_i}(k)[Z_i]_{bk}$. Thus, detailed simulations of the processes inside a particle over time can be conducted with KM-GAP.

A differential equation is constructed for each layer to account for mass transport and gain or loss from chemical reactions. For example, the change in the absolute number of molecules of species Z_i in bulk layer k over time ($\frac{dN_{Z_i,bk}}{dt}$) is:

$$\frac{dN_{Z_i,\mathrm{b}k}}{dt} = \left(J_{\mathrm{b}k-1,\mathrm{b}k,Z_i} - J_{\mathrm{b}k,\mathrm{b}k-1,Z_i}\right)A(k) + \left(J_{\mathrm{b}k+1,\mathrm{b}k,Z_i} - J_{\mathrm{b}k,\mathrm{b}k+1,Z_i}\right)A(k+1)$$

$$+ \left(P_{\mathrm{b}k,Z_i} - L_{\mathrm{b}k,Z_i}\right)V(k) \;\; (k = 2, \ldots., n-1)$$

This equation includes multiple terms to represent mass transport flux between bulk layer k and the layers before and after it (k-1, k+1 respectively). ($J_{\mathrm{b}k-1,\mathrm{b}k,Z_i}$) is the mass transport flux for species Z_i from bulk layer k-1 to bulk layer k and $J_{\mathrm{b}k,\mathrm{b}k-1,Z_i}$ is the mass transport flux for species Z_i from bulk layer k to bulk layer k-1. The difference between these terms is the net flux between the two layers which is multiplied by the area $A(k)$ (cm^2) of bulk layer k to determine the number of molecules of Z_i that is gained or lost from layer k at each time step. A similar expression is

used for mass transport between layers k and k+1. Also included in the differential equation for the layer is a term for the production ($P_{\mathrm{b}k,Z_i}$, molecules cm^{-3}) and loss ($L_{\mathrm{b}k,Z_i}$, molecules cm^{-3}) from a chemical reaction. An analogous differential equation is included for each chemical species in every layer. Since the kinetic framework on which KM-GAP is based is compatible with the resistor model, predictions from the kinetic model can be used with already existing information from previous models to consider kinetic limitations in a system.

Due to the substantial global presence of atmospheric aerosol particles, it is crucial that the processes related to their formation, reactivity and aging be characterized well to accurately consider their effect on public health and the climate. Consequently, the need to consider kinetic limitations on partitioning and other processes within or on the surface of SOA particles is of paramount importance.

1.5: Importance of amines and mixtures to atmospheric aerosol particles

Application of KM-GAP to key atmospheric systems will aid in the elucidation of mechanisms for processes that may experience kinetic limitations, such as new particle formation (NPF) and nanoparticle growth, which are essential to our understanding of cloud condensation nuclei.[55, 76, 77] It is already commonly accepted that sulfuric acid, which is formed when sulfur dioxide is oxidized in the air, plays a major role in NPF and growth.[19, 78, 76] Thermodynamic modeling predicts that sulfuric acid in the presence of water and base will preferentially form low volatility sulfate salts.[79] Since ammonia is the most abundant basic compound in the atmosphere – present at up to ppb levels depending on proximity to source – its protonated form ammonium is the expected counter ion. During recent field campaigns though, signals attributed to aminium salts were detected during the analysis of nanoparticles.[76, 80]

In aminium salts, the cations are protonated amines such as methylamine or dimethylamine. Amines are derivatives of ammonia, where one or more hydrogen has been substituted with an alkyl or aryl group. While there are many different amines present in the atmosphere, the most prevalent are low molecular weight small chain amines, such as methylamine, dimethylamine and trimethylamine.[79] Small–chain alkyl amines were not thought to be involved in particle formation as they are highly volatile and present at much lower ppt levels.[81] However, Smith et al.[76] concluded that depending on location, aminium salts could account for almost half of positive ions from particles collected in the field. Additionally, Zordan et al., observed that ammonia alone could not account for the nitrogen present in atmospheric aerosol particles.[82] Hence, the role of atmospheric amines in aerosol particle formation and growth has become an area of great interest.

Due to their high vapor pressure, amines most likely to partition into the particle phase by dissolving in the aqueous phase through reaction, undergoing oxidation to form SOA or through reactive uptake reactions such as acid–base reactions to form aminium salts.[12, 79] The displacement of ammonium by aminium ions from ammonium bisulfate and ammonium nitrate has been demonstrated to be favored for 1-2 nm molecular clusters. However, this result is not projected to extend to larger cluster sizes.[83] In the past decade, multiple studies of reactive uptake of amines by ammonium sulfate and ammonium nitrate particles have been reported.[12, 81, 84] It has been reported that the phase state of the particle is an important factor. Thus, a kinetic model for this system could provide important information about the effect of phase state on the reactive uptake of amines by ammonium salts.

Systems with aerosol particles containing both inorganic and organic compounds should be investigated. As discussed in Section 1.1, aerosol particles typically contain a mixture of

organic and inorganic components, with many of the organic compounds comprising SOA generated from reactions of volatile organic compounds in the gas phase or particle phase. SOA can be formed from a variety of volatile organic compounds emitted from anthropogenic or biogenic sources. The most common precursors are biogenic compounds emitted by vegetation, such as α–pinene and isoprene.[31] However, anthropogenic VOCs, such as toluene and naphthalene, have also been shown to form SOA and can interact with biogenic aerosol particles.[2, 9, 31] Charnawskas et al. reported that anthropogenic SOA affects cloud formation to a greater degree than biogenic SOA.[31] The interplay between inorganic and organic compounds, and anthropogenic and biogenic sources adds an additional level of complexity to our atmosphere that global models must be able to simulate.

The organic portion of atmospheric aerosol can consist of hundreds or thousands of compounds. For this reason, investigation of SOA mixtures from different organic precursors is strongly encouraged. For example, aerosol from vegetation that is burned for campfires and other domestic uses – known as biomass burning aerosol – is considered one of the primary sources of brown carbon.[28] The composition and physical properties of brown carbon is highly dependent on source and the location at which it is generated. Another important source of information about such mixtures is diesel-derived SOA. Diesel fuel vehicle emissions are a significant source of anthropogenic VOCs. Since diesel emissions contain both combustion products and residual fuel, they lead to the release of a wide range of hydrocarbons and aromatic compounds.[85] Diesel exhaust is also the source of particulate matter that is implicated in air pollution and disease as their inhalation can bring allergens into the body or exacerbate existing conditions.[23, 24] Thus, the viscosity and phase state of atmospheric particles and their kinetic implications on atmospheric processes is a rich area of study that warrants continued attention

CHAPTER 2

PREDICTING THE GLASS TRANSITION TEMPERATURE AND VISCOSITY OF SECONDARY ORGANIC MATERIAL USING MOLECULAR COMPOSITION

Portions of this chapter are reproduced with permission from: DeRieux, W. S. W.; Li, Y.; Lin, P.; Laskin, J.; Laskin, A.; Bertram, A. K.; Nizkorodov, S. A.; Shiraiwa, M., Predicting the glass transition temperature and viscosity of secondary organic material using molecular composition. *Atmospheric Chemistry and Physics* **2018**, *18*, 6331-6351.

2.1: Introduction

Secondary organic aerosol (SOA) accounts for a large fraction of submicron particles in the atmosphere and they play an important role in climate, air quality and public health.[35, 86] Traditionally, SOA particles were assumed to be liquid with dynamic viscosity η below 10^2 Pa s, but a number of recent studies have shown that they can also adopt amorphous semi-solid ($10^2 \leq \eta \leq 10^{12}$ Pa s), or glassy solid ($\eta > 10^{12}$ Pa s) states, depending on chemical composition and temperature.[5, 36, 37, 87] The phase state is also strongly affected by relative humidity, as water can act as a plasticizer to lower viscosity.[14] Ambient and laboratory-generated SOA particles have been observed to bounce off the smooth hard surface of an inertial impactor at low RH, implying a non-liquid state,[10, 88-90] whereas predominantly biogenic SOA particles in the Amazon basin did not bounce off the impactor surface at high RH, implying they are primarily liquid.[91] Upon dilution or heating, SOA particles were observed to evaporate unexpectedly slowly,[92, 93] and recent modeling studies have evaluated the contributions of low diffusivity and volatility to slow evaporation rates.[94, 95] Measurements of the viscosity of SOA bulk material derived from the oxidation of α-pinene,[38, 40, 96] limonene,[97] isoprene,[39] and toluene[9] have confirmed that SOA particles adopt a wide range of viscosities.

Viscosity can be directly converted to bulk diffusivity in organic molecules using the Stokes–Einstein equation.[98-101] This equation has been shown to work well for organic molecules diffusing through materials with η below ~10^3 Pa s.[102, 103] Note that this relation is not accurate for predicting the bulk diffusivity of water and small molecules and it may also underestimate the diffusivity of organic molecules in a highly viscous matrix by a few orders of magnitudes.[1, 36, 98-107] The particle phase state, viscosity, and bulk diffusivity have been shown to affect the gas uptake and chemical transformation of organic compounds due to the kinetic limitations of bulk

diffusion,[1, 58, 66, 104, 108-116] which may facilitate the long-range transport of organic compounds embedded in viscous or glassy particles.[62, 117] Molecular motion can be hindered in a highly viscous matrix, slowing down photochemical reactions in particles.[97, 118] Water diffusion can still be fast even in an amorphous solid matrix under room temperature, but it can be hindered significantly under low temperatures,[14, 32, 119-121] affecting homogeneous vs. heterogeneous ice nucleation pathways.[32, 122-129] Despite the substantial implications of the SOA particle phase state, its effects on gas-particle interactions have not yet been considered explicitly in current climate and air quality models.[62]

The partitioning of semi-volatile compounds into viscous particles may result in kinetically limited growth in contrast to quasi-equilibrium growth,[130-132] which also affects the evolution of particle size distribution upon SOA growth.[60, 133] Note that the equilibration timescale of SOA partitioning is determined by bulk diffusivity or viscosity, but is also affected by other factors such as volatility, accommodation coefficient, particle size and mass loadings.[42, 134, 135] Chamber experiments probing the mixing timescales of SOA particles derived by oxidation of various precursors such as isoprene, terpene, and toluene have observed strong kinetic limitations at low RH, but not at moderate and high RH.[136-138] Several studies have observed the kinetic limitations of the bulk diffusion of organic molecules including polycyclic aromatic hydrocarbons[112, 139] and isoprene-derived epoxydiols[58] in SOA, while Gorkowski et al.[56] did not observe significant diffusion limitations for glycerol and squalene in α-pinene SOA. Quasi-equilibrium versus kinetically-limited or non-equilibrium SOA growth remains an open issue and warrants further investigations.

Group contribution methods have been used to predict the viscosities of pure compounds when the functionality and molecular structure are known.[7, 140] Song et al.[141] showed that

estimations from group contribution approaches combined with either non-ideal or ideal mixing reproduced the RH-dependent trends particularly well for the alcohol, di-, and tricarboxylic acid systems with viscosity of up to 10^4 Pa s. In contrast, model calculations overestimated the viscosity of more viscous compounds including monosaccharides, disaccharides, and trisaccharides by many orders of magnitude.[141] A recent study compiled the viscosity of organic compounds with atmospherically relevant functional groups, investigating the influence of the number and location of functional groups on viscosity.[7] These studies provide important insights in estimating the viscosity of individual organic compounds.

Particle phase state can be characterized by a glass transition temperature (T_g), which is a characteristic temperature representing a non-equilibrium phase transition from a glassy solid state to a semi-solid state as the temperature increases.[5] Recently, a method has been developed to estimate T_g of pure organic compounds comprised of carbon, hydrogen, and oxygen (CHO compounds) with molar mass less than 450 g mol^{-1} based on their molar mass and atomic O:C ratio.[34] It has been applied successfully in a global chemistry climate model to predict T_g and the phase state of atmospheric SOA, which indicated that SOA particles are mostly liquid or semi-solid in the planetary boundary layer, while they should be glassy in the middle and upper troposphere.[34] A recent study provided a consistent result, suggesting that mixing timescales of organic molecules within SOA are often < 1 h in a global planetary boundary layer.[142]

It has been shown that SOA particles contain oligomeric compounds with molar masses higher than 450 g mol^{-1},[143-146] which makes the previously developed parameterization incomplete. In this study, we extend the parameterization of T_g to higher–molar–mass compounds, and apply it to high–resolution mass spectrometry data for toluene SOA and biomass burning particles. The Arrhenius approach and the Gordon–Taylor mixing rules were

applied to estimate the viscosity of SOA bulk materials to compare with the literature–reported viscosity measurements. This method will be useful for estimations of viscosity of organic particles, for which high–resolution mass spectra are available. It can also be applied in global or regional models to evaluate the impacts of the particle phase state on the role of SOA in climate and air quality.

2.2: Parameterization development

2.2.1: Glass transition temperature

Figure 2.1a shows the dependence of T_g on the molar mass (M) of organic compounds. Solid markers represent measured T_g of 258 CHO compounds,[5-7] while open markers represent 654 CHO compounds in SOA.[8] Markers are color-coded by atomic O:C ratio. Their melting points (T_m) were estimated by the Estimation Programs Interface (EPI) Suite software version 4.1[147] and their T_g values were estimated using the Boyer–Kauzmann rule: $T_g = g \cdot T_m$ with $g = 0.7$.[5, 34] This rule can provide good estimates of T_g, as has been validated in previous work[5] and also shown in Fig. 2.2(a). A subset of data shown in Figure 2.1 was originally published in Shiraiwa et al.[34] for compounds with $M < 450$ g mol^{-1}. This version of the figure has been updated to include a number of experimentally measured T_g values of larger compounds with M up to 1153 g mol^{-1}, including aliphatic compounds containing OH and/or COOH groups. Specifically, data for 76 aliphatic alcohols, 39 carbohydrates and their derivatives, 4 carboxylic acids, and 4 hydroxy acids, as compiled by Rothfuss and Petters,[7] have been added to Figure 2.1. Eight of these compounds are carbohydrates with $M > 450$ g mol^{-1}. These updates are critical for reliable parameterization of T_g based on M. When M increases above ~500 g mol^{-1}, the slope of T_g decreases, making it challenging to extrapolate the low-M data from the original Shiraiwa et

al.[34] study to higher M values. When M increases to ~1000 g mol^{-1}, the corresponding T_g appears to level off at around 420 K.

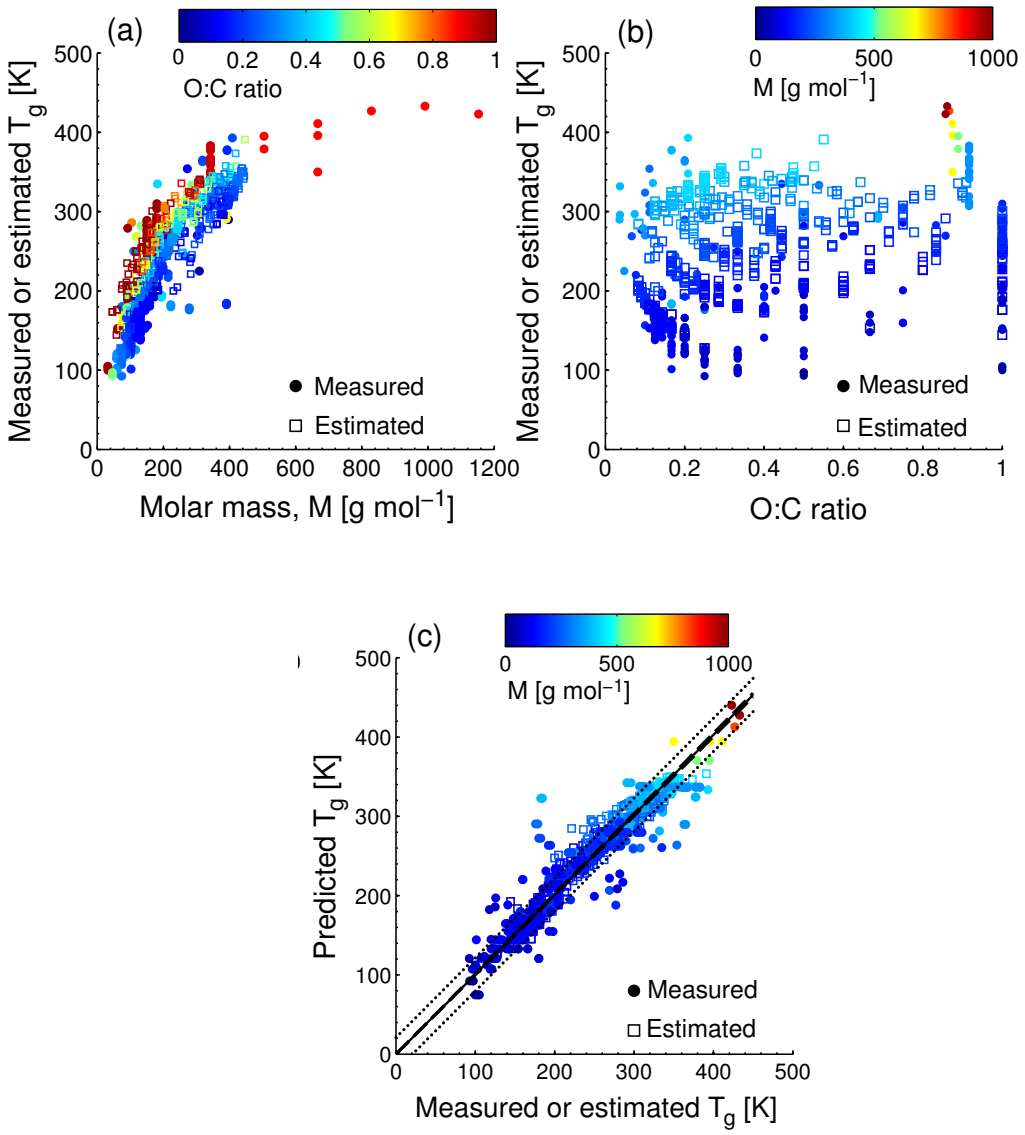

Figure 2.1. Characteristic relationships between molecular properties and the glass transition temperature (T_g) of organic compounds. (a) T_g of organic compounds as measured (circles) and estimated with the Boyer-Kauzmann rule (squares) plotted against molar mass. The markers are color-coded by atomic O:C ratio. (b) Measured (circles) and estimated (squares) T_g of organic compounds plotted against O:C ratio. The markers are color-coded by molar mass. (c) Predicted T_g for CHO compounds using a parameterization (Eq. 2) developed in this study compared to measured (circles) and estimated T_g by the Boyer-Kauzmann rule (squares). The solid line shows 1:1 line and the dashed and dotted lines show 68% confidence and prediction bands, respectively.

Such dependence on M has been described for polymers with the Fox-Flory equation:[148] $T_g(M) = T_{g,\infty} - \frac{K_m}{M}$, where K_m is a constant and $T_{g,\infty}$ is the asymptotic value of T_g specific to the polymer. We conducted a literature search and found that most of the reported $T_{g,\infty}$ values fell

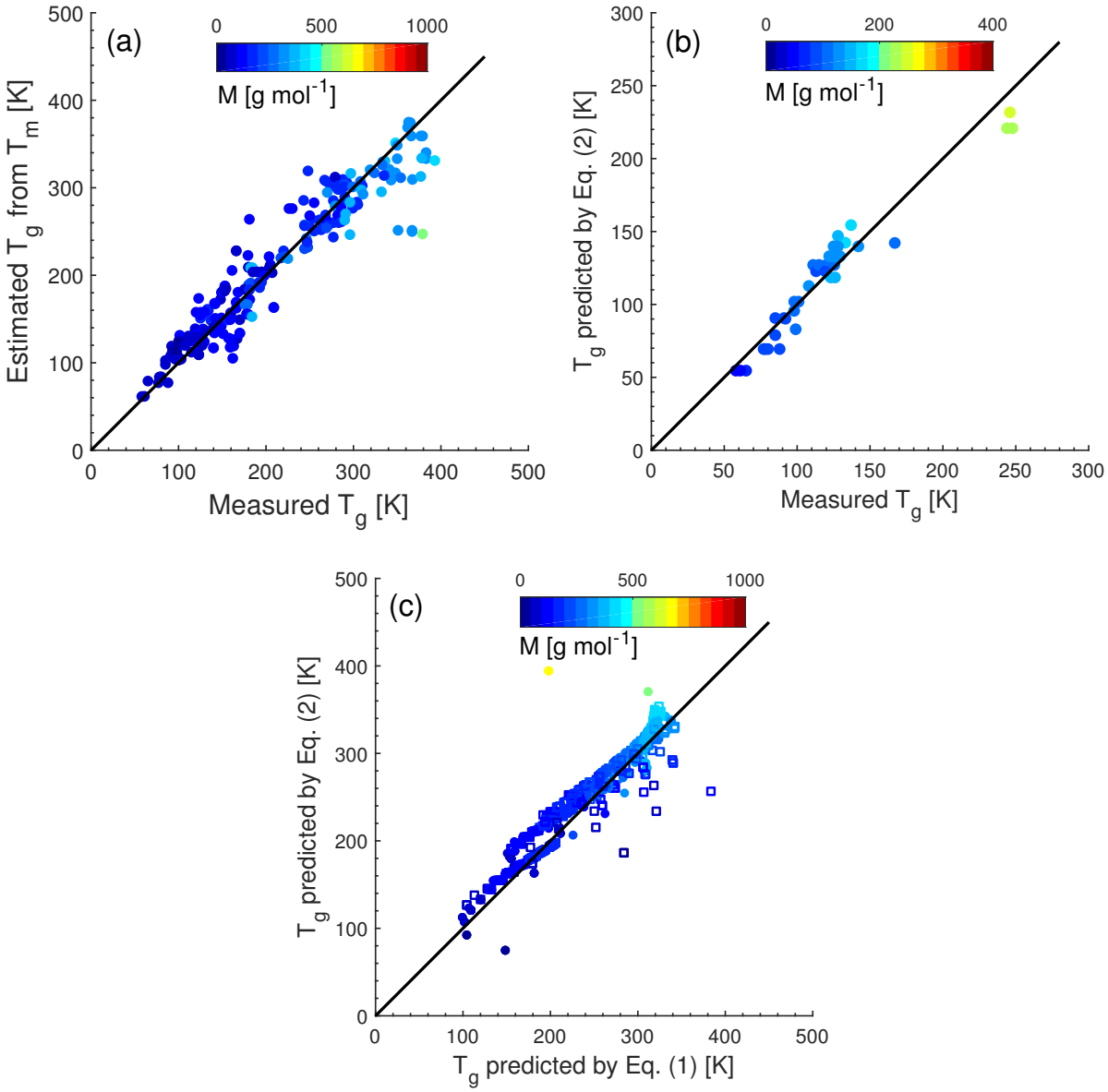

Figure 2.2. (a) Comparison of measured and estimated T_g by the Boyer-Kauzmann rule for 251 organic compounds (Koop et al.;[5] Dette et al.;[6] Rothfuss and Petters[7]) with their measured T_m available. The markers are color-coded by molar mass. (b, c) Predicted T_g using Eq. (2) compared with (b) measured T_g for CH compounds and (c) predicted T_g using Eq. (1) for CHO compounds. The solid line shows 1:1 line. Solid circle markers represent organic compounds as compiled in Koop et al.[153] and open square marker represent SOA oxidation products in Shiraiwa et al.[8] in panel (c).

below ~500 K.[148-152] The Fox-Flory equation works very well for high molar mass compounds and is also generally applicable to smaller compounds,[5] as supported by an approximately linear dependence of T_g on the inverse molar mass in Fig. 2.3(a). Figure 2.1b plots the values of T_g as a function of the atomic O:C ratio of

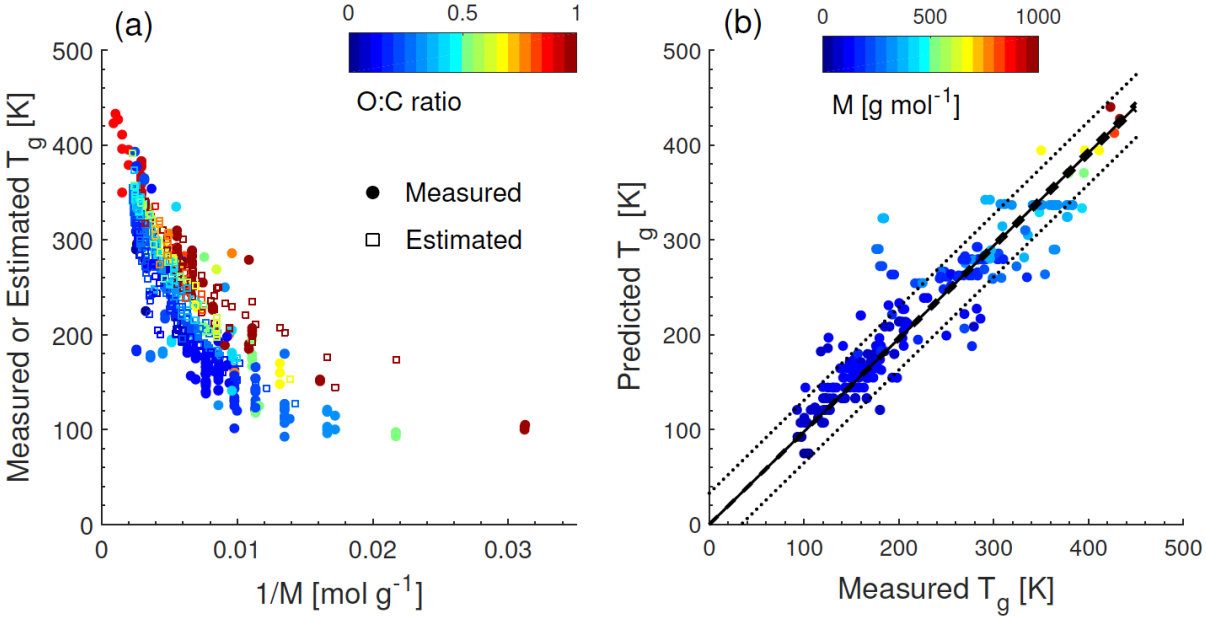

Figure 2.3. (a) T_g of organic compounds as measured (circles) and estimated with the Boyer-Kauzmann rule (squares) plotted against the inverse molar mass. The markers are color-coded by atomic O:C ratio. (b) Predicted T_g for CHO compounds using a parameterization (Eq. 2) developed in this study compared to measured T_g (circles). The solid line shows 1:1 line and the dashed and dotted lines show 68% confidence and prediction bands, respectively.

organic molecules. Figures 2.1a and 2.1b clearly demonstrate that T_g depends primarily on the molar mass with a weak dependence on the atomic O:C ratio.

A parameterization for T_g calculation based on the molar mass and atomic O:C ratio was developed in Shiraiwa et al.,[26] which is applicable to CH and CHO compounds with $M < 450$ g mol^{-1}:[34]

$$T_g = A + BM + CM^2 + D\,(O{:}C) + E\,M\,(O{:}C), \quad (1)$$

where A = –21.57 (±13.47) [K], B = 1.51 (±0.14) [K mol g^{-1}], C = -1.7×10^{-3} ($\pm3.0\times10^{-4}$) [K mol^2 g^{-2}], D = 131.4 (±16.01) [K] and E = –0.25 (±0.085) [K mol g^{-1}]. These values were obtained by fitting the measured T_g of 179 CH and CHO compounds with $M < 450$ g mol^{-1} with multi-linear least squares analysis. Note that application of Eq. (1) may provide unreasonable T_g values for compounds with $M > 500$ g mol^{-1} because it does not account for the strong curvature in the T_g vs. M dependence shown in Figure 2.1a.

Table 2.1. Composition classes and the n_C^0 and b values (K) for glass transition temperature parameterizations obtained by least-squares optimization using the measurements compiled in Koop et al.,[5] Dette et al.,[6] and Rothfuss and Petters.[156]

Classes	n_C^0	b_C	b_H	b_{CH}	b_O	b_{CO}
CH	1.96 (±1.81)	61.99 (±53.65)	–113.33 (±44.47)	28.74 (±20.86)		
CHO	12.13 (±2.66)	10.95 (±13.60)	–41.82 (±14.78)	21.61 (±5.30)	118.96 (±9.72)	–24.38 (±4.21)

In this study we have developed an improved parameterization to predict T_g of CH and CHO compounds using the number of carbon (n_C), hydrogen (n_H), and oxygen (n_O) that can also be applied to higher–molar–mass compounds. Motivated by a good correlation between T_g and volatility (Fig. 1a in Shiraiwa et al.[26]), we use an equation with a similar formulation to the equation used to predict the saturation mass concentration or volatility:[64, 153]

$$T_g = (n_C^0 + ln(n_C))\,b_C + ln(n_H)\,b_H + ln(n_C)\,ln(n_H)\,b_{CH} + ln(n_O)\,b_O + ln(n_C)\,ln(n_O)\,b_{CO} \quad (2)$$

where n_C^0 is the reference carbon number, b_C, b_H and b_O denote the contribution of each atom to T_g, and b_{CH} and b_{CO} are coefficients that reflect contributions from carbon-hydrogen and carbon-oxygen bonds, respectively. These values were obtained by fitting the measured T_g of 42 CH

compounds and 258 CHO compounds with multi-linear least squares analysis with 68% prediction and confidence intervals. The best-fit parameters are summarized in Table 2.1. Note that the evaluation dataset used to derive Eq. (2) contains CH compounds with $M < 260$ g mol^{-1} (see Fig. 2.2b for comparison of measured and predicted T_g). Thus, the application of Eq. (2) to higher–molar–mass compounds may require further refinement of the method when measured T_g for higher–molar–mass CH compounds becomes available. 2.1c shows that the T_g values predicted using Eq. (2) are in good agreement with the T_g values measured in experiments (see also Fig. 2.3(b)) or estimated by the Boyer-Kauzmann rule as indicated by the high correlation coefficient of 0.95. T_g of individual compounds can be predicted within ±21 K as indicated by the prediction band (dotted lines in Fig. 2.1c); however, this uncertainty may be much smaller for multicomponent SOA mixtures under ideal mixing conditions as indicated in the confidence band (dashed lines, almost overlapping with the 1:1 line).

These results are noteworthy given that the parameterization (Eq. 2) does not consider either explicit molecular structures or functional groups. Previous studies have shown that T_g can be especially sensitive to the number of OH groups, which interact strongly through hydrogen bonding. For example, Nakanishi and Nozaki[154] found a direct relationship between T_g and the number of hydroxyl groups in a molecule for sugar alcohols; T_g increases as the number of OH groups increases. They reported that the correlation between T_g and the number of OH groups was much stronger than the correlation between T_g and the number of carbons in a molecule. Such a trend is implicitly included in Eqs. (1) and (2), which contain the O:C ratio and number of oxygen atoms as parameters, respectively. Recently, Rothfuss and Petters[156] showed an approximately linear relationship between the number of OH groups and T_g for compounds with up to eight OH groups. Grayson et al.[155] showed that addition of hydroxyl functional groups

increases viscosity, a conclusion supported by both the experimental data and quantitative structure-property relationship model. The correlation between T_g and the number of carbon atoms is consistent with the free volume theory, in which molecular motion is restricted by the difference between the space required for a molecule to vibrate versus the space in which the molecule resides (i.e., the free volume).[156] The correlation between T_g and the number of OH groups is more consistent with the topological constraint theory, in which the primary influence is the three–dimensional structure of the molecule as determined by molecular bonds and hydrogen-bonding networks.[154, 157] Future experiments targeting more comprehensive T_g data, especially for higher–molar–mass compounds, would lead to further refinements of our T_g parameterizations.

Comparing Eqs. (1) and (2), the two parameterizations give a similar performance for compounds with $M < 450$ g mol^{-1} as shown in Fig. 2.2c. The statistical measures of correlation coefficient (R), mean bias (MB), and root mean square error (RMSE) are 0.93, –6.45 K, and 25.64 K, respectively, for the performance of Eq. (1), while for Eq. (2), they are 0.95, 3.15 K, and 21.11 K, respectively. It should be noted again that Eq. (1) cannot be used to predict T_g for compounds with $M > 450$ g mol^{-1}. For example, T_g of stachyose ($M = 667$ g mol^{-1}) predicted by Eq. (1) is 198 K, while that by Eq. (2) is 394 K, which agrees much better with the measured mean T_g of 396 K.[7] Eq. (2) is more flexible than Eq. (1) and can be potentially expanded to include compounds containing heteroatoms (e.g., nitrogen or sulfur), once substantial sets of experimental values of T_g for such compounds become available. Regarding the applications in air quality and climate models, Eq. (1) can be applied in the volatility basis set (VBS)[43, 153] and the molecular corridor approach[8, 64] to predict the T_g of SOA particles,[26] while the new

parameterization may be suitable for coupling with the statistical oxidation model, which characterizes the SOA evolution as a function of n_C and n_O.[158, 159]

These parameterizations (Eqs. 1, 2) calculate T_g based on the elemental composition of organic compounds. SOA particles contain a number of organic compounds as well as a variable amount of liquid water, which has low T_g (136 K) and can act as a plasticizer.[5, 14] Under humid conditions, SOA particles take up water by hygroscopic growth in response to RH, lowering T_g and the viscosity of SOA particles. Estimations of T_g for SOA-water mixtures were discussed by Shiraiwa et al.[26], who applied the Gordon–Taylor equation validated for a wide range of mixtures of organics, polymer, and water.[6, 37, 46, 160, 161] Briefly, T_g of mixtures of SOA compounds under dry conditions ($T_{g,org}$) were calculated assuming the Gordon–Taylor constant (k_{GT}) of 1: $T_{g,org} = \sum_i w_i T_{g,i}$, where w_i is the mass fraction of organic compound i, which can be derived using mass concentrations of SOA products. The Gordon–Taylor equation can also be applied to calculate T_g of organic–water mixtures considering the mass fraction of organics (w_{org}) in SOA particles:[5]

$$T_g(w_{org}) = \frac{(1-w_{org})T_{g,w} + \frac{1}{k_{GT}} w_{org} T_{g,org}}{(1-w_{org}) + \frac{1}{k_{GT}} w_{org}} \quad (3)$$

w_{org} can be calculated using the mass concentrations of water (m_{H_2O}) and SOA (m_{SOA}) as $w_{org} = m_{SOA} / (m_{SOA} + m_{H_2O})$. m_{H_2O} can be estimated using the effective hygroscopicity parameter (κ):[162]

$$m_{H2O} = \frac{\kappa \rho_w m_{SOA}}{\rho_{SOA}\left(\frac{1}{a_w} - 1\right)} \quad (4)$$

The density of water (ρ_w) is 1 g cm^{-3}, the density of SOA particles (ρ_{SOA}) is assumed to be 1.2 g cm^{-3},[163] m_{SOA} is the total mass concentrations of SOA, and a_w is the water activity calculated as a_w = RH/100. Pajunoja et al.[164] found that water uptake in subsaturated conditions is inhibited

until RH is high enough for the dissolution of water in SOA particles with relatively low O:C ratios. As the oxidation of SOA increases, the solubility of water increases and dissolution occurs at lower RH values. In both cases, the use of subsaturated hygroscopicity measurements was supported.

2.2.2: Viscosity

The temperature dependence of viscosity (η) can be predicted using the modified Vogel-Tammann-Fulcher (VTF) equation:[48]

$$\eta = \eta_\infty e^{\frac{T_0 D}{T - T_0}} \quad (5)$$

where η_∞ is viscosity at infinite temperature; T_0 is the Vogel temperature; T is the ambient temperature. The fragility parameter, D, characterizes how rapidly the dynamics of a material slow down as T approaches T_g, reflecting to what degree the temperature dependence of the viscosity deviates from Arrhenius behavior. When T is close to T_g ($T_g/T \approx 1$), smaller D values indicate that viscosity is sensitive to temperature change (fragile behavior); while larger D values indicate that viscosity is less sensitive to temperature change (strong or Arrhenius behavior).

Assuming η_∞=10^{-5} Pa s:[48]

$$\log \eta = -5 + 0.434 \frac{T_0 D}{T - T_0} \quad (6)$$

When $T = T_g$, $\eta = 10^{12}$ Pa s, which leads to:[48, 165]

$$T_0 = \frac{39.17\, T_g}{D + 39.17} \quad (7)$$

As can be seen in Eq. (7), both T_g and D are required to calculate η from Eq. (6) at a given temperature. Figure 2.4 shows the T_g-scaled Arrhenius plot of fragility (viscosity versus T_g/T)

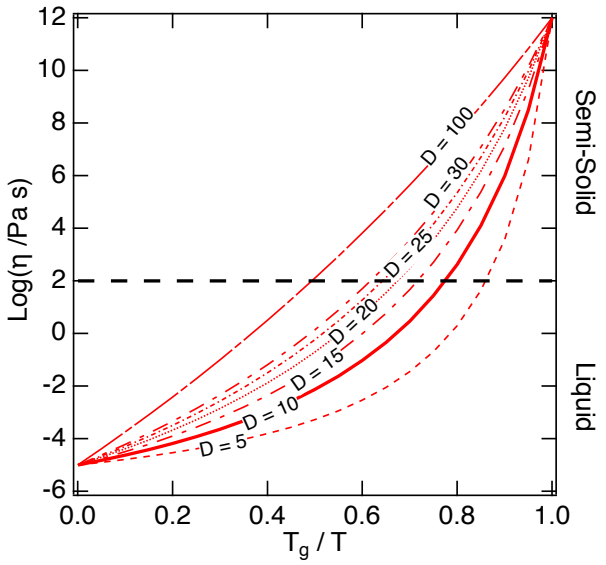

Figure 2.4. The Angell plot of viscosity (η) vs. T_g/T. The lines represent different fragility parameter (D) values in the range of 5 - 100, with D = 10 (the solid line) used as a base case for this study. A large fragility parameter value is associated with a strong glass former, while fragile materials are associated with lower values. The black dashed line at viscosity of 10^2 Pa s indicates the approximate threshold between liquid and semi-solid states.

referred to as an Angell plot.[47] D values of organic compounds are typically in the range of ~5–30.[50] To estimate D values that could be applied to SOA compounds, we compiled measured fragility values. Fragility was often measured in the form of the fragility steepness index (m), which represents the slope of the Arrhenius plot at the point where $T = T_g$.[49] Compounds with lower m exhibit higher D values, indicating stronger glass formers. The measured m values of 95 organic compounds are included in the Table. m can be converted to D using equation (8):

$$D = \frac{665.89}{m-17} \qquad (8)$$

The fragility steepness index (m) is defined as:

$$m = \lim_{T \to Tg} \frac{d\, log\eta}{d(T_g/T)} \qquad (9)$$

Combining Eq. (9) with Eq. (6) gives:

$$m = \lim_{T \to Tg} \frac{d}{d(T_g/T)} \left(-5 + 0.434 \frac{T_0 D}{T - T_0}\right) \qquad (10)$$

Considering that $\eta = 10^{12}$ Pa s at $T = T_g$,[48] and by defining $\Delta x = 1 - T_g/T$, a combination with Eq. (7) leads to:

$$m = \lim_{\Delta x \to 0} \frac{1}{\Delta x} \left(12 - \left(-5 + 0.434 \frac{\frac{39.17\, T_g}{D + 39.17} D}{\frac{T_g}{1 - \Delta x} - \frac{39.17\, T_g}{D + 39.17}} \right) \right)$$

$$= \lim_{\Delta x \to 0} \frac{1}{\Delta x} \left(17 - 0.434 \frac{39.17 T_g D (1 - \Delta x)}{D T_g + 39.17 T_g \Delta x} \right)$$

$$= \lim_{\Delta x \to 0} \frac{(665.89 + 17D)}{(D + 39.17\Delta x)}$$

$$= \frac{665.89 + 17D}{D} \quad (11)$$

Note that Eq. (11) is derived assuming that the high temperature limit of viscosity η_∞ is equal to 10^{-5} Pa s[48] in the VTF equation (Eq. 5). Similar equations for the relation between m and D were given by previous studies using different η_∞ and units[51, 119, 165] and applying those gave very similar results in our study.

Figure 2.5 shows the measured D as a function of (a) molar mass and (b) the atomic O:C ratio of organic molecules. The molar mass exerts a stronger effect on fragility, while there is little dependence of D on the O:C ratio. As molar mass increases, D approaches a lower limit of 10.3 (± 1.7), consistent with the value of 10 used in our recent study.[34] To evaluate the impact of the variations of D on viscosity prediction, sensitivity calculations were conducted as described in Sect. 2.3.

Besides the VTF equation, another commonly used equation for describing the temperature dependence of viscosity is the Williams–Landel–Ferry (WLF) equation: $\log \frac{\eta(T)}{\eta(T_g)} = \frac{-C_1(T - T_g)}{C_2 + (T - T_g)}$, where empirical parameters C_1 and C_2 are adopted as 17.44 and 51.6 K, respectively.[114, 128, 166]

The two equations are mathematically equivalent, both defined with respect to a reference temperature, and their parameters are related through $C_1 = \frac{DT_0}{2.303(T_g - T_0)}$ and $C_2 = T_g - T_0$. For the WLF equation, T_g is the reference temperature and there is a linear dependence assumed between temperature and

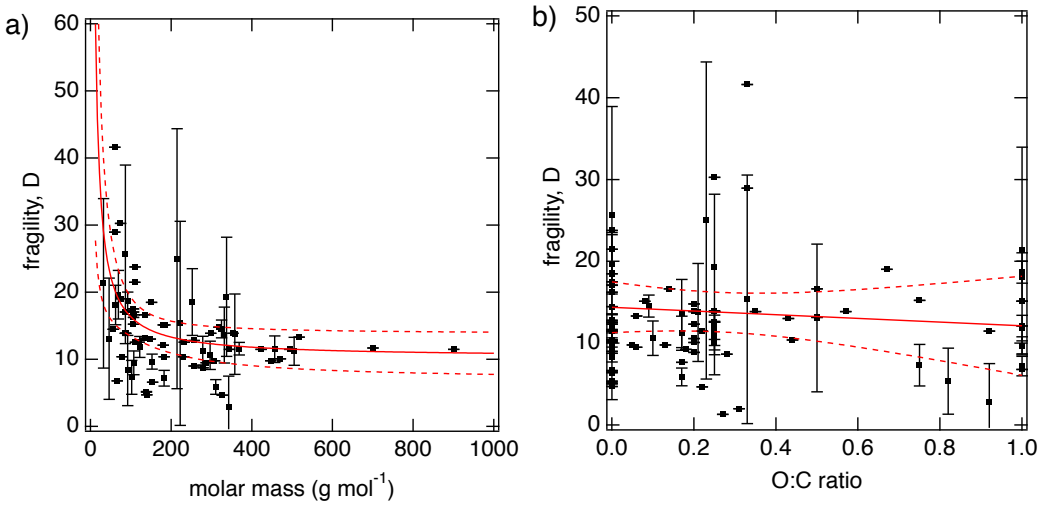

Figure 2.5. Fragility parameter of organic compounds (D) plotted against (a) molar mass and (b) atomic O:C ratio. Error bars are standard deviations. The solid red lines represent the fitted curves with fitted equations for (a) $D = 602.6/M + 10.3$ and (b) $D = 14.4 - 2.3$(O:C) respectively. Dashed red lines indicate the 95% confidence band.

free volume.[167-169] For the VTF equation, the reference is the Vogel temperature (T_0), a hypothetical temperature at which all non-vibrational motion ceases and viscosity becomes infinite and the theoretical foundation of the VTF equation includes both thermodynamic and kinetic considerations.[167-169] Recently, Rothfuss and Petters[170] applied a similar approach to model viscosity for sucrose particles by applying the VTF and Gordon–Taylor approaches. The calculations of the viscosity of multi-component SOA mixtures in this study are based mainly on the VTF equation, and the difference between calculated results from the two equations will be briefly discussed in the following section.

Table 2.2. Fragility values from literature. Shaded rows indicate multiple values have been reported for a compound.

Compound Name	m	D
0/100 polyurethane/polyaminourethane[171]		1.3
1,1'-Di(4-methoxy-5-methylphenyl)cyclohexane[172]	66	13.59
1,1'-Di(4-methoxy-5-methylphenyl)cyclohexane[173]	60	15.49
1,1'-Di(p-methoxyphenyl)cyclohexane[173]	90	9.12
1,1'-Di(p-methyloxyphenyl)cyclohexane[172]	72	12.11
1,2-propanediol[174]	52	19.03
1,2,4-butanetriol[154]	60.7	15.24
1,2,6-hexanetriol[154]	67.6	13.16
1,2,7-heptanetriol[154]	68.2	13.01
1,3-bis(1-naphthyl)-5-(2-naphthyl)benzene[167]	66	13.59
1,3-bis(1-naphthyl)-5-(2-naphthyl)benzene[175]	86	9.65
1,3-bis(1-naphthyl)-5-(2-naphthyl)benzene[176]	76	11.29
1,3-bis(3-phenoxyphenoxy)benzene[167]	85	9.79
1,3-diphenyl-1,1,3,3-tetramethyldisiloxane[176]	87	9.51
100/0 polyurethane/polyaminourethane[171]		2.00
2-benzylphenol[176]	61	15.13
2-methyl-1-propanol[176]	39	30.27
2-methylpentane[174]	36	35.05
2-methylpentane[176]	58	16.24
2-methyltetrahydrofuran[176]	65	13.87
3-bromopentane[176]	53	18.50
3-methyl-1,3,5-pentanetriol[154]	57	16.65
3-methylaniline[174]	79	10.74
3-methylaniline[176]	98	8.22
3-methylpentane[176]	56	17.07
3-methylphenol[176]	57	16.65
9-bromophenanthrene[176]	69	12.81
Benzene[177]	81	10.40
Beta-D-fructofuranose[176]	61	15.13
Butyronitrile[174]	47	22.20
Butyronitrile[176]	56	17.07
Cimetidine[178]	65	13.87
Cimetidine[178]	54	18.00
Cimetidine[178]	45	23.78
Cinnarizine[179]	70.75	12.39
Cinnarizine[179]	70.67	12.41
cis/trans-decahydro-naphthalene[180]	147	5.12
cis/trans-decahydro-naphthalene[176]	145	5.20

Compound Name	m	D
Cyanoadamantane[181, 182]	23	110.98
Cyanocyclohexane[181, 183]	48	21.48
D-glucose[176]	72	12.11
Decahydroisoquinoline[175]	158	4.72
Deuterated 1,3-bis(1-naphthyl)-5-(2-naphthyl)benzene[175]	83	10.09
Dibutyl phthalate[50]	69	12.81
Dibutyl phthalate[184]	85	9.79
Diethyl phthalate[185]		2.20
Diethyl phthalate[185]		32.00
Diethyl phthalate[176]	73	11.89
Dipyridamole[179]	81.94	10.25
Dipyridamole[179]	65.51	13.73
Ethanol[50]		2.70
Ethanol[181, 186]	52	19.03
Ethanol[176]	55	17.52
Ethylbenzene[176]	58	16.24
Ethylene glycol[50]		16.00
Ethylene glycol[176]	50	20.18
Famotidine[178]	68	13.06
Famotidine[178]	43	25.61
Flopropione[176]	81	10.40
Glibenclamide[176]	75	11.48
Griseofulvin[176]	65	13.87
Hydrochloro-thiazide[176]	65	13.87
Hyperbranched polyamine ester[187]		2.50
Hyperbranched polyamine ester[187]		8.20
Indomethacin[188]	89	9.25
Indomethacin[176]	75	11.48
Isooctylcyanobiphenyl[181, 185]	85	9.79
Isopropylbenzene[176]	70	12.56
Li-acetate[176]	115	6.79
m-fluoroaniline[167]	70	12.56
m-fluorotoluene[176]	45	23.78
m-xylene[176]	56	17.07
Maltitol[176]	75	11.48
Methanol[50]		12.40
Methanol[176]	39	30.27
n-Butene[176]	63	14.48
N-Ethylacetamide[176]	65	13.87
n-Propanol[176]	40	28.95

Compound Name	m	D
Nizatidine[178]	91	9.00
Nizatidine[178]	62	14.80
Nizatidine[178]	56	17.07
o-Terphenyl[189]	81	10.40
o-Xylene[167]	55	17.52
Phenobarbital[176]	70	12.56
Phenolphthalein[176]	62	14.80
Phenyl salicylate[50]		38.70
Phenyl salicylate[176]	76	11.29
Poly(4-methylstyrene)[190]	121	6.40
Poly(4-methylstyrene)[190]	75	11.48
Poly(alpha-methylstyrene)[190]	149	5.04
Poly(alpha-methylstyrene)[190]	74	11.68
Poly(benzylmethacrylate)[190]	89	9.25
Poly(cyclohexylethylene)[190]	117	6.66
Poly(cyclohexylethylene)[190]	82	10.24
Poly(cyclohexylmethacrylate)[190]	83	10.09
Poly(cyclohexylmethacrylate)[190]	80	10.57
Poly(cyclohexylmethacrylate)[190]	71	12.33
Poly(diphenoxyphosphazene)[190]	104	7.65
Poly(phenylmethacrylate)[190]	92	8.88
Poly(t-butylstyrene)[190]	141	5.37
Poly(t-butylstyrene)[190]	71	12.33
Polytetrahydrofuran[191]	109.6	7.19
Polytetrahydrofuran[191]	63.8	14.23
Polytetrahydrofuran[191]	86.1	9.64
Polytetrahydrofuran[191]	67.9	13.08
Polytetrahydrofuran[191]	77.9	10.93
Polytetrahydrofuran[191]	63.1	14.44
Probucol[176]	67	13.32
Propane-1,2,3-triol[192]	57	16.65
Propane-1,2,3-triol[193]	53	18.50
Propane-1,2,3-triol[154]	50	20.18
Propane-1,2,3-triol[176]	51	19.59
Propane-1,2,3-triol[176]	53	18.50
Propanol[50]	33	41.62
Propylene carbonate[50]	104	7.65
Propylene carbonate[181]	90	9.12
Propylene carbonate[175]	93	8.76
Propylene carbonate[176]	99	8.12

Compound Name	m	D
Sorbitol[192]	128	6.00
Sorbitol[193]	127	6.05
Sorbitol[154]	102.3	7.81
Sorbitol[174]	93	8.76
Sorbitol[176]	107	7.40
Squalane[175]	75	11.48
Sucrose[50]		0.15
Sucrose[176]	98	8.22
Sucrose benzoate[194]	94	8.65
Tetrachloromethane[195]	118	6.59
Threitol[192]	79	10.74
Threitol[154]	68.4	12.96
Toluene[188]	131	5.84
Compound Name	m	D
Toluene[174]	59	15.85
Toluene[176]	103	7.74
Triphenyl phosphite[50]	160	4.66
Triphenyl phosphite[196]	125	6.17
Triphenyl phosphite[176]	115	6.79
Triphenylchloromethane[167]	93	8.76
Triphenylethene[176]	91	9.00
Triphenylphosphate[174]	160	4.66
Xylitol[192]	94	8.65
Xylitol[154]	78.3	10.86
Xylitol[176]	87	9.51

2.3: Comparison of predicted viscosity with measurements

2.3.1: SOA formed from α–pinene and isoprene

The purpose of this section is to demonstrate that the viscosity of SOA material can be predicted over a broad range of RH values from four parameters: T_g of dry SOA ($T_{g,org}$), fragility (D), hygroscopicity (κ), and the Gordon–Taylor constant for mixing SOA and water (k_{GT}). The viscosity of α-pinene SOA has been measured or estimated as a function of RH by several groups using multiple experimental techniques as shown in Fig. 2.6(a).[10, 38, 40, 41, 139, 197, 198] The

wide range of experimentally measured viscosities reported for α-pinene SOA, particularly from 30-60% RH is most likely a consequence of the different experimental approaches, mass loadings and O:C ratios for each experiment. For instance, Grayson et al.[41] used mass loadings of 121 to 14000 μg m^{-3} and observed that viscosity decreased as mass loading increased. Higher mass loadings would lead to greater partitioning of semi-volatile and lower–molar–mass compounds into the particle phase, which would lead to the decrease in T_g and the viscosity of the resulting SOA mixture, as very recently demonstrated experimentally by Jain et al.[199] Grayson et al.[34] concluded that their results should be considered a lower limit for the viscosity of α-pinene SOA in the atmosphere. It should also be noted that the viscosity measurements from Renbaum–Wolff et al.[38] were for the water-soluble portion of the SOA. These datasets suggest that the viscosity of α-pinene SOA approaches very high values (~>10^8 Pa s) below 20-30% RH and decreases with an increase in RH reaching a value of ~10 Pa s at 80% RH. As can be seen in Fig. 2.6(b), PAM–generated isoprene SOA is less viscous with $\eta < 10^6$ Pa s even under dry conditions, undergoing a phase transition from a semi-solid phase to a liquid phase at ~55% RH.[10, 39]

The solid lines with the shaded areas in Fig. 2.6 are viscosity values predicted using $T_{g,org}$, D, κ, k_{GT}. $T_{g,org}$ values were adopted by Berkemeier et al.,[32] who estimated $T_{g,org}$ with the Boyer-Kauzmann rule using the melting point of representative SOA oxidation products. Note that Eqs. (1) and (2) were not used to estimate $T_{g,org}$, which should be done in future studies by obtaining their elemental composition using high–resolution mass spectrometry. For α-pinene, $T_{g,org}$ was assumed to be 278 K corresponding to an O:C ratio of 0.5,[32] which is a typical O:C ratio of α-pinene SOA.[200-202]

The $T_{g,org}$ selected for isoprene SOA was 255 K, corresponding to the O:C ratio of 0.6. Although no measurements of the O:C ratio for the experimental isoprene SOA data were reported, Song et al.[39] estimated O:C of 0.64-1.1 based on literature values. As O:C ratios are useful in estimating $T_{g,org}$, we encourage the measurement of the O:C ratio of SOA when conducting viscosity measurements. In contrast to α-pinene SOA, there are limited viscosity measurements for isoprene SOA. While the predicted viscosity is consistent with the experimental data, comparison of our model predictions to additional measurements is strongly recommended. Song et al.[39] prepared isoprene SOA in a potential aerosol mass (PAM) reactor while the data by Bateman et al.[10] were for isoprene SOA generated in a smog chamber. It has been suggested that under ambient conditions, the majority of isoprene-derived SOA can be

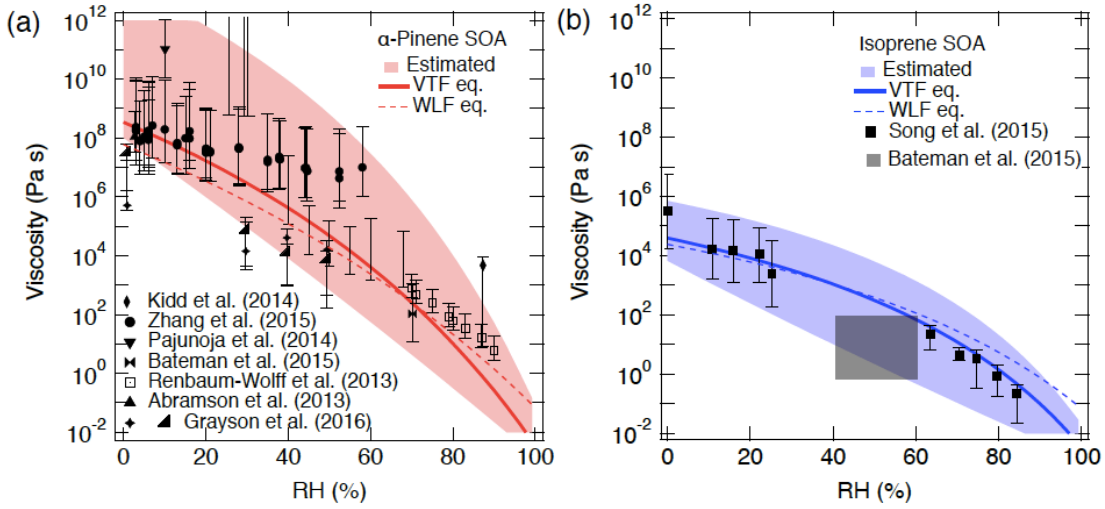

Figure 2.6. Comparison of measured and predicted viscosity of (a) α-pinene SOA and (b) isoprene SOA at 295 K as a function of RH. The solid lines represent base simulations applying glass transition temperature of dry SOA ($T_{g,org}$), fragility (D), hygroscopicity (κ) and Gordon-Taylor constant (k_{GT}) of 278.5 K, 10, 0.1 and 2.5 respectively for (a) α-pinene SOA and 255 K, 10, 0.1 and 3.0 respectively for (b) isoprene SOA. The shaded regions were calculated with varying those parameters: $T_{g,org}$ = 300 K (278.5 K), κ = 0.1 (0.1), D = 20 (10), k_{GT} = 2.5 (2.0) for the upper (lower) limit in (a); $T_{g,org}$ = 255 K (255 K), κ = 0.15 (0.15), D = 15 (8), k_{GT} = 3.0 (2.5) for the upper (lower) limit in (b).

derived through heterogeneous interactions with acidic sulfate particles forming oligomers,[203-205] which may increase viscosity compared to the model SOA generated in PAM or a chamber. Further studies are warranted to compare laboratory-generated and ambient isoprene SOA and to investigate the effect of the acidic seed on the viscosity.

For both α-pinene and isoprene SOA, D was set to 10 based on the analysis presented in Fig. 2.5(a). κ was set to 0.1 based on field and laboratory measurements[198, 206-208] and k_{GT} was assumed to be 2.5.[5, 37] Using these parameters, the predicted viscosities match the magnitude and the RH-dependence of the measured viscosity of α-pinene and isoprene SOA. Figure 2.6 also shows predicted viscosities (dotted lines) using the WLF equation, which shows similar values as the VTF equation, but slightly underestimates the viscosity of α-pinene SOA at low RH and overestimates the viscosity of isoprene SOA at high RH.

Sensitivity studies were conducted to examine the effects of $T_{g,org}$, D, κ and k_{GT}, on the calculated viscosity. In these studies, $T_{g,org}$ of α-pinene and isoprene SOA were varied within 229-328 K and 255-316 K, respectively, representing $T_{g,org}$ of different oxidation states.[32] D was varied between 5 and 30, which is the range characteristic for organic compounds (see Fig. 2.5a). κ values of 0.05-0.15 were used for α-pinene and isoprene SOA.[164, 207] For the Gordon–Taylor constant, values of 2.5±1.5 were considered.[5, 6, 37, 46]

The effect of varying each parameter on the calculated viscosity of α-pinene SOA is illustrated in Fig. 2.7. Variations of ±50 K in $T_{g,org}$ result in 3-6 order of magnitude differences in calculated values at dry conditions, indicating that $T_{g,org}$ is a critical parameter for viscosity estimations. Decreasing D from 10 to 5 led to a decrease in calculated values by more than 1 order of magnitude. The calculated results were within the upper limit of measurements when increasing D from 10 to 20, and the predicted values were only slightly enhanced when further

increasing D from 20 to 30. Calculated values with variations in κ from 0.05 to 0.15 and k_{GT} from 1.0 to 4.0 were all within the measured ranges. For isoprene SOA, an increase of $T_{g,org}$ to 287 K, which represents a higher oxidation state,[32] led to calculated values to be several orders of magnitude higher than the upper limit of measurements (Fig. 2.8a). When $T_{g,org}$ reaches 316 K, isoprene SOA can occur as a solid for RH lower than ~40%. Compared to α-pinene SOA, a variation in D has a larger effect on the calculated viscosity (Fig. 2.8b). For a range of 5–30 for D, calculations with the D value of 10 agreed well with the measurements, while other D values

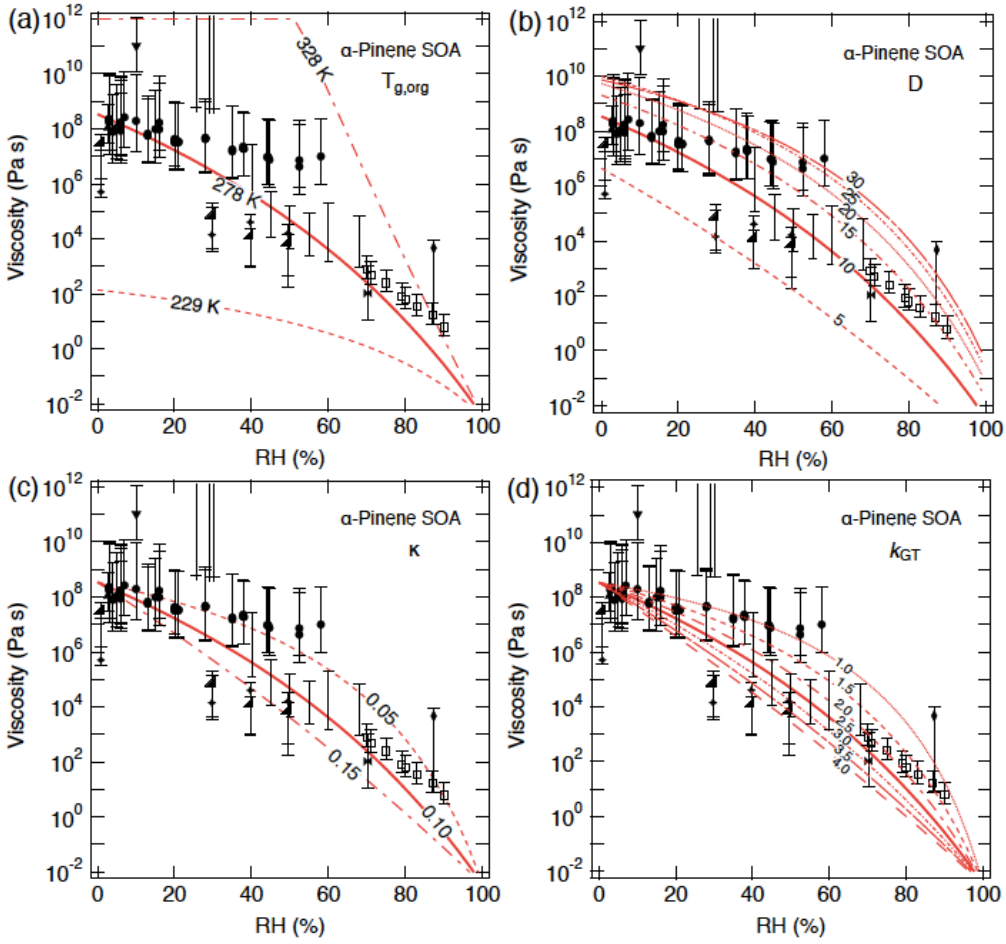

Figure 2.7. Sensitivity calculations for viscosity of α-pinene SOA at ambient temperature of 295 K as a function of RH at varying: a) glass transition temperature of dry SOA ($T_{g,org}$), b) fragility (D), c) hygroscopicity (κ), and d) Gordon-Taylor constant (k_{GT}).

resulted in calculated viscosity outside of the measured ranges. Figures 2.8c and 2.8d show that decreasing κ and k_{GT} below the reference values, the predictions overestimate the measured η by 1 or 2 orders of magnitude. The latter is most evident at RH > 60%, at which the calculated values were higher than the upper limit of measurements. Modeling results with κ and k_{GT} increasing to 0.15 and 4.0, respectively, were within the lower limit of measurements.

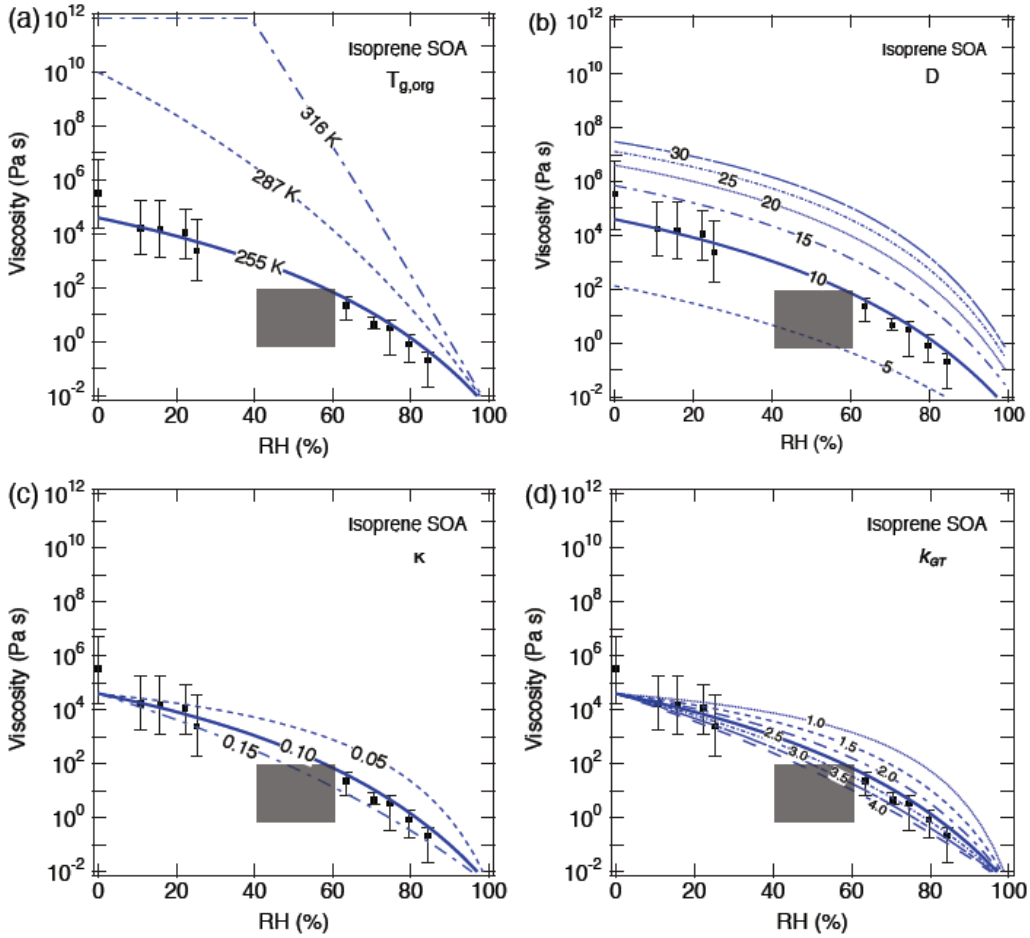

Figure 2.8. Sensitivity calculations for viscosity of isoprene SOA at ambient temperature of 295 K as a function of RH at varying: a) glass transition temperature of dry SOA ($T_{g,org}$), b) fragility (D), c) hygroscopicity (κ), and d) Gordon-Taylor constant (k_{GT}).

The above comparison between the measured and predicted viscosity demonstrates that the method described in this study can reproduce reasonably well the measured RH-dependent viscosity of SOA formed from α-pinene and isoprene. The sensitivity calculations showed that

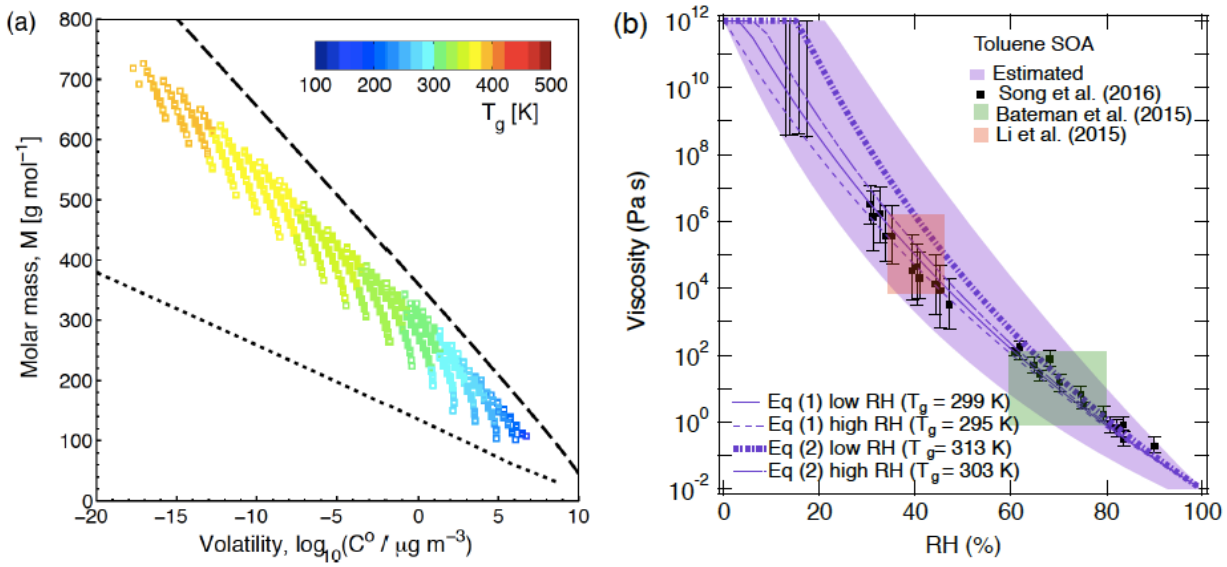

Figure 2.9. (a) Molecular corridor of molar mass plotted against volatility of toluene SOA formed under dry conditions[2] color-coded by glass transition temperature (T_g) estimated using Eq. (2). The upper dashed line indicates the low O:C bound of the molecular corridor (linear alkanes C_nH_{2n+2} with O:C = 0), and the lower dotted line indicates the high O:C bound (sugar alcohols $C_nH_{2n+2}O_n$ with O:C = 1). (b) Comparison of measured (markers) and modeled (lines) viscosity of toluene SOA at 295 K as a function of RH. Viscosities were calculated using fragility (D) of 13, the hygroscopicity (κ) of 0.25 and the Gordon-Taylor constant (k_{GT}) of 3.0 with different glass transition temperatures of dry SOA ($T_{g,org}$) as estimated using Eq. (1) or (2) under low and high RH conditions. The shaded regions were calculated by varying those parameters: $T_{g,org}$ = 313 K (295 K), κ = 0.20 (0.25), D = 13 (10), k_{GT} = 2.5 (3.5) for the upper (lower) limit. Mass loadings were 23 μg m^{-3} for LRH and 8 μg m^{-3} for HRH.[2]

$T_{g,org}$ contributed the most to the uncertainty in the viscosity estimates. Previous studies have shown that the experimental conditions such as particle mass concentrations[41] and RH upon SOA formation[2, 197] can impact chemical composition of SOA and hence the phase state and viscosity. Further efforts to constrain the uncertainties are needed both in experiments and parameterizations.

2.3.2: SOA formed from toluene

In this and the following sections, we examine the feasibility of calculating the value of $T_{g,org}$ from mass spectrometry data on SOA.[2] measured the elemental composition of toluene SOA using nanospray desorption electrospray ionization high-resolution mass spectrometry (nano-DESI-HRMS).[209, 210] Toluene SOA were formed by OH photooxidation in an aerosol smog chamber at <2% RH (mass loading = 23 μg m^{-3}) and 75% RH (mass loading = 8 μg m^{-3}) to investigate the effect of RH on the chemical composition of toluene SOA formed under low-NO_x conditions. Measurements revealed a significant reduction in the fraction of oligomers present in toluene SOA generated under high RH conditions compared to SOA generated under low RH conditions.[2] The detected molar mass of individual oxidation products spanned a range of 102–570 g mol^{-1} at high RH, which increased up to 726 g mol^{-1} at low RH.

Figure 2.9a shows the interdependence of glass transition temperature, volatility, and molar mass of the detected toluene SOA compounds. Glass transition temperatures were calculated using Eq. (2). The saturation mass concentrations or volatilities of detected compounds were estimated from the elemental composition by using the parameterization of Li et al.[64] The analysis is based on the molecular corridor approach—a two-dimensional framework of volatility and molar mass of SOA components constrained by boundary lines of low and high atomic O:C ratios, corresponding to *n*-alkanes (C_nH_{2n+2}, O:C = 0) and sugar alcohols ($C_nH_{2n+2}O_n$, O:C = 1), respectively,[8, 64] The toluene SOA constituents are well constrained by the molecular corridor and T_g values are higher for compounds with a higher molar mass and lower volatility.

Equation (1) was used to calculate T_g for individual compounds with M < 450 g mol^{-1}, while excluding compounds with molar mass higher than 450 g mol^{-1}. This approach was deemed reasonable as such high–molar–mass compounds account for < 10% of all toluene SOA

products formed at low RH, and for < 2% formed at high RH. Equation (2) was used to calculate T_g for all the detected compounds. T_g of dry toluene SOA ($T_{g,org}$) was then computed using the Gordon–Taylor approach with k_{GT} = 1 (Sect. 2.2.1). The relative mass concentrations of individual components were assumed to be proportional to their relative abundance in the nano-DESI-HRMS spectrum. This assumption has a number of caveats,[211, 212] and as we will see below, it results in deviations between the predicted and measured viscosity. Table 2.2 summarizes the results of such calculations, showing that the $T_{g,org}$ by Eq. (1) – excluding

Table 2.3. Glass transition temperatures calculated using Eq. (1) and (2) for toluene SOA mixtures at low relative humidity (low RH < 2%) and high relative humidity (high RH = 75%) conditions.

$T_{g,org}$ (K)	low RH	high RH
Equation (1)*	299	295
Equation (2)	313	303

Compounds with M > 450 g mol^{-1} were excluded from the analysis.

high–molar–mass compounds – is about 10 K lower as compared to $T_{g,org}$ by Eq. (2). $T_{g,org}$ at low RH is predicted to be higher than $T_{g,org}$ at high RH, which results from a lower abundance of high–molar–mass compounds observed at high RH. This trend is consistent with,[197] who showed that SOA material formed under dry conditions is more viscous than that formed under wet conditions.

Figure 2.9b shows the predicted viscosity of toluene SOA as a function of RH compared to the measured viscosity of toluene SOA formed in an oxidation flow reactor at 13% RH.[9] Indirect viscosity measurements are also included in shaded boxes for toluene-derived SOA.[10, 11] Lines with shaded areas are calculated viscosities using $T_{g,org}$ as described above. κ was assumed to be 0.25 based on laboratory measurements.[207, 213] To achieve good fit, D was set to 13 and k_{GT} was assumed to be 3.0.[6] Estimations with Eq. (1) match the measured viscosity values very well

over the entire RH range. Predictions with Eq. (2) overestimated the measurements by 1 or 2 orders of magnitude at moderate RH between 30% and 50%, while they agreed with the measurements derived at RH ≥ 60% and at the dry conditions.

There are several possible reasons for the difference between the measurements and predictions. First, the relative abundance of high–molar–mass compounds observed in HRMS measurements may be overestimated, as high–molar–mass compounds tend to have higher (yet generally unknown) ionization efficiencies compared to lower–molar–mass compounds. Second,

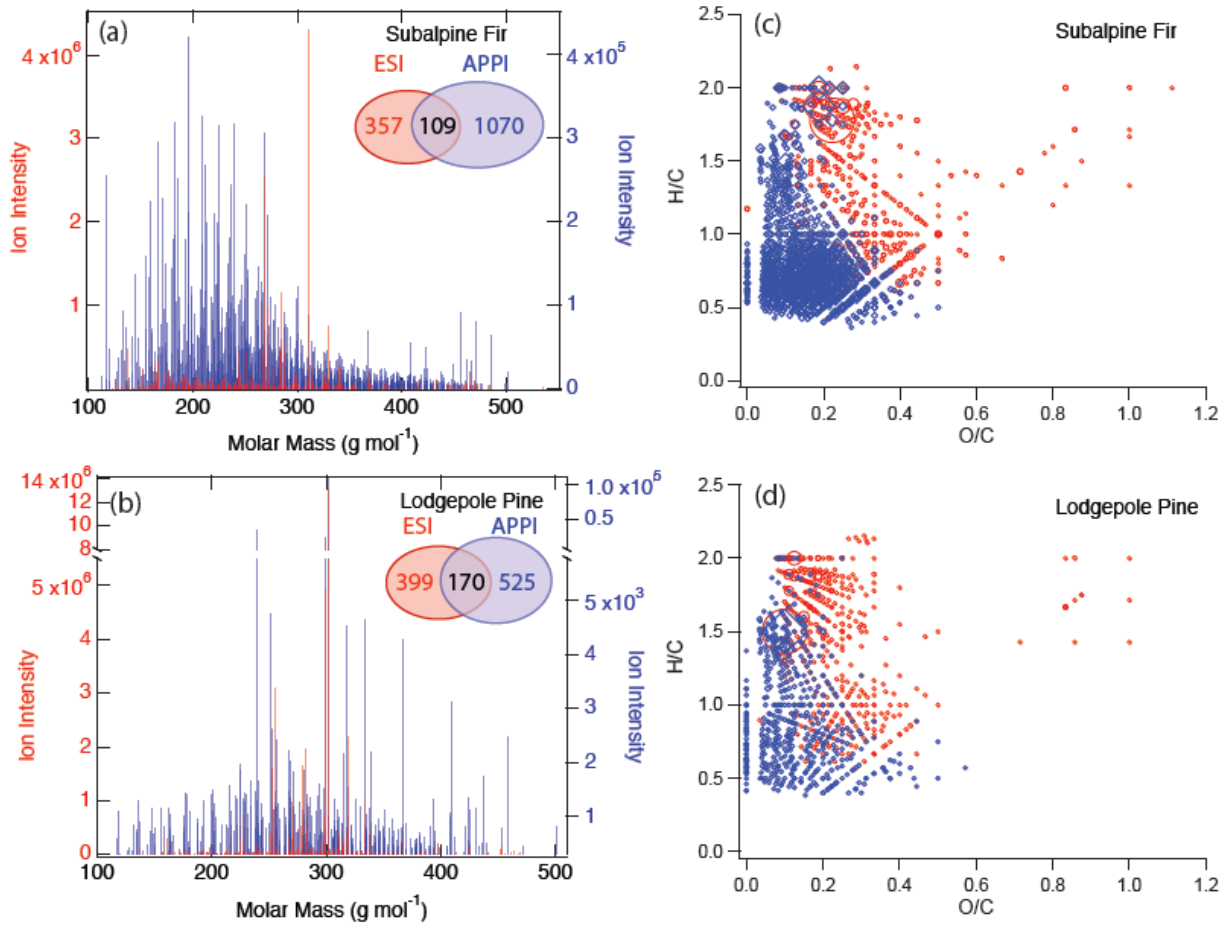

Figure 2.10. Mass spectra of biomass burning organic particles collected from test burns of (a) subalpine fir and (b) lodgepole pine as measured by high resolution mass spectrometry with two ionization techniques: electron spray ionization (ESI, red) and atmospheric pressure photoionization (APPI; blue). Numbers of elemental formulas identified by ESI (red), APPI (blue) and both modes (black) are also specified. Van Krevelen plots of the compounds identified by ESI (red) and APPI (blue) mode in BBOA from burning of (c) subalpine fir and (d) lodgepole pine.

the nano-DESI-HRMS analysis of toluene SOA was limited to m/z range of 100–1000.[2] It is possible that some SOA products with lower molar mass were present in particles but not detected, which would lead to an overestimation of T_g. Third, the chemical composition of toluene SOA is likely different between Hinks et al.[201] and Song et al.[9] because of the differences in the experimental conditions. Specifically, toluene SOA was formed in a Teflon chamber in Hinks et al., while Song et al. used an oxidation flow reactor to generate toluene SOA. The O:C ratios are 0.71 at low RH and 0.63 at high RH based on nano-DESI-HRMS measurements in Hinks et al.,[201] while the O:C ratio was 1.06 in Song et al.[5] based on the aerosol mass spectrometry (AMS) measurements.

In addition, different mass loadings may have affected viscosity. Song et al.[5] measured viscosity at two different mass loadings (60-100 and 600-1000 μg m^{-3}) and compared their results to the toluene SOA data in Bateman et al. (2015; 30–50 μg m^{-3}) and Li et al. (2015; 44–125 μg m^{-3}), observing little impact of mass loadings on viscosity. We carried out a sensitivity study of mass loadings on viscosity using a set of compounds detected by HRMS. The saturation mass concentration was predicted for each component using the molecular corridor approach.[64] Assuming that the mass signal intensity is proportional to the total mass concentration of the compound in the mixture and applying the absorptive partitioning theory,[214] particle–phase concentrations of each compound were predicted to estimate T_g at different organic aerosol mass

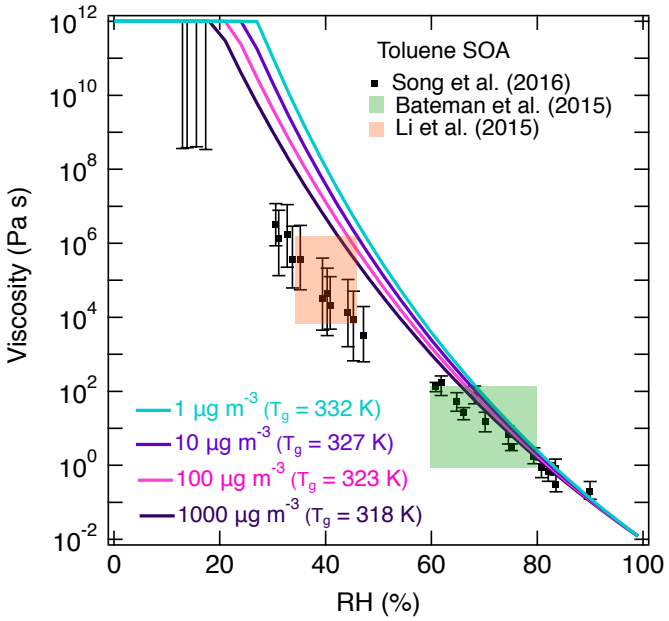

Figure 2.11. Effect of mass loading on predicted viscosity for toluene SOA. Solid lines represent the predicted viscosity with Eq. (2) using chemical composition of toluene SOA formed at low RH. Viscosity was predicted with different mass loadings ranging from 1-1000 μg m^{-3}. Markers and shaded boxes represent experimentally measured viscosity values. Song et al.[9] mass loadings were 60-100 and 600-1000 μg m^{-3}. Bateman et al.,[10] and Li et al.,[11] mass loadings were 30-50 μg m^{-3} and 44-125 μg m^{-3}, respectively.

loading values (1–1000 μg m^{-3}). The glass transition temperature of the SOA mixture decreases as mass loading increases. Viscosity decreases up to 2 orders of magnitude at low RH, while at high RH there is little difference as shown in Fig. 2.11. Simultaneous measurements of viscosity and chemical composition with different mass loadings should be performed in future studies.

2.3.3: Biomass Burning Particles

To further explore the applicability of our viscosity prediction method using elemental composition as measured by HRMS, we performed similar calculations for biomass burning organic particles emitted from test facility burns of subalpine fir and lodgepole pine trees, which were conducted as a part of the FIREX 2016 campaign.[215] These samples were analyzed by HRMS using two different ionization sources: electrospray ionization (ESI) and atmospheric

pressure photoionization (APPI). The mass spectra shown in Fig. 2.10a and b indicate that a substantial number of compounds were detected by both methods (109 and 170 compounds for subalpine fur and lodgepole pine, respectively). However, pronounced differences are also observed between the ESI and APPI spectra both in terms of the identity and signal intensities of the detected compounds.

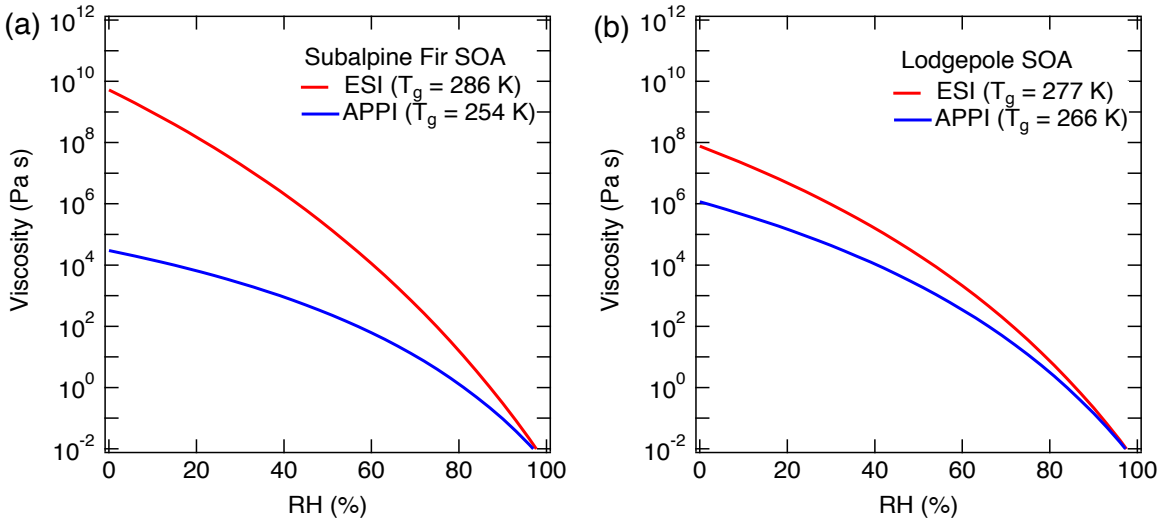

Figure 2.12. Predicted viscosity for biomass burning particles of (a) subalpine fir and (b) lodgepole pine trees as measured by high resolution mass spectrometry with two ionization techniques: electrospray ionization (ESI, red) and atmospheric pressure photoionization (APPI; blue). $T_{g,org}$ are specified in the figure legend and other used parameters are fixed to $\kappa = 0.1$, $D = 10$, $k_{GT} = 2.5$.

Glass transition temperatures for the assigned CH and CHO compounds were computed using Eq. (2). Nitrogen– and sulfur–containing compounds (CHON and CHOS) are not yet covered by Eq. (2) and were therefore excluded from the analysis. CHON and CHOS compounds comprised less than 10% of the detected ion intensity and <15% of the assigned compounds. Note that we do not intend to provide accurate estimates of the viscosity of ambient biomass burning particles (as inorganic components are also not included in this analysis), but we investigate how the use of different ionization methods would lead to variations in our viscosity predictions. T_g values of organic mixtures ($T_{g,org}$) were then calculated using the Gordon–Taylor approach with k_{GT} = 1,

assuming that the relative concentration of each compound is proportional to its MS signal intensity. The calculated $T_{g,org}$ values for the mixtures are specified in the legend of Fig. 2.12. For both types of mixtures, the calculated $T_{g,org}$ for the APPI MS data is lower than the value calculated based on the ESI MS data with a difference of 32 K for subalpine fir and 11 K for the lodgepole pine. Figure 2.12 shows the predicted viscosity as a function of RH, assuming $D = 10$, $\kappa = 0.10$ and $k_{GT} = 2.5$. The difference in $T_{g,org}$ derived from ESI and APPI results in a variation of predicted viscosity at low RH by up to 5 and 2 orders of magnitude for subalpine fir and lodgepole pine, respectively.

The difference in the calculated $T_{g,org}$ values is attributed to the chemical profile of the species detected using different ionization techniques as shown in the mass spectra in Fig. 2.10a and b. The van Krevelen diagrams in Fig. 2.10c and d illustrate these compositional differences between chemical species detected by ESI and APPI. ESI is more efficient at detection of polar compounds,[216] which typically have higher O:C ratios and therefore would result in higher predicted values of glass transition temperature.[5, 89] APPI enables the detection of nonpolar compounds with lower O:C ratios, in particular polycyclic aromatic hydrocarbons (PAHs), that have low ionization efficiencies when analyzed by ESI MS.[217, 218] Due to the complementary nature of these ionization methods, it is most likely that the actual glass transition temperature and viscosity of each type of organic components in biomass burning aerosols are somewhere in between the values inferred from ESI and APPI data sets: ESI MS may be viewed as providing the upper limit of viscosity, while APPI MS gives the lower limit. Our results indicate that the use of complementary ionization techniques may help evaluate the associated uncertainty for the prediction of viscosity values based on elemental composition as measured by HRMS.

2.4: Conclusions

We have developed a parameterization for the calculation of the glass transition temperature of individual SOA compounds with molar mass up to ~1100 g mol^{-1} using the number of carbon, oxygen, and hydrogen atoms. The viscosity of SOA was estimated using the T_g-scaled Arrhenius plot of viscosity versus T_g/T and the Gordon–Taylor approach to account for mixtures of SOA and water. The fragility parameter D was compiled for organic compounds and we found that D approaches a lower limit of ~10 (±1.7) as the molar mass increases. The resulting viscosity estimations agree well with the measured viscosity of α-pinene and isoprene SOA, validating our method. Using HRMS data, the glass transition temperatures of individual components and the viscosity of toluene SOA were predicted, also resulting in a good agreement with measurements. However, we note that the predicted viscosities were higher than the measured values suggesting that additional considerations may need to be taken into account. For example, the ionization efficiency of both low– and high–molar–mass compounds may have a pronounced effect on the relative abundance of different classes of compounds in HRMS data. The viscosity prediction method was also applied to biomass burning particles, whose elemental composition was measured using HRMS with two different ionization techniques. Substantial differences in viscosity estimations were

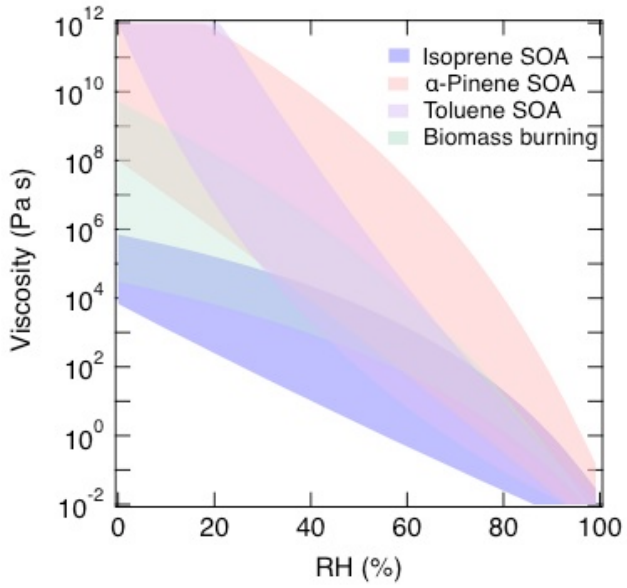

Figure 2.13. Summary of predicted range of viscosity of α-pinene SOA (red), isoprene SOA (blue), toluene SOA (purple), and biomass burning particles (green).

obtained using ESI and APPI mass spectra because these two ionization methods probe different subsets of compounds.

Figure 2.13 summarizes the predicted range of viscosity of α-pinene SOA, isoprene SOA (generated by PAM), toluene SOA, and biomass burning particles. Isoprene SOA has lower viscosity, reflecting lower glass transition temperature due to the relatively low molar mass of isoprene oxidation products. α-Pinene and toluene SOA have much higher viscosity with a different shape of the RH dependence due to differences in glass transition temperatures and hygroscopicity. Biomass burning particles have moderate viscosity between the two extreme cases. Currently, both predictions and measurements are subject to large uncertainties and variations. Complementary measurements of viscosity and chemical composition employing different ionization techniques are desired to further constrain RH-dependent viscosity in future studies. Current T_g parameterizations do not consider functionality or molecular structure explicitly and further measurements of T_g and viscosity of SOA would allow us to refine the method presented in this study. Nevertheless, current results offer a promising starting point and such simple parameterizations are practical for predicting viscosity of particles as measured by HRMS. The developed viscosity prediction method should also be useful in recent efforts to simulate the distribution of SOA phase state and related properties in regional or global air quality models e.g., [34, 142]

CHAPTER 3

EFFECTS OF PHASE STATE AND PHASE SEPARATION ON DIMETHYLAMINE UPTAKE OF AMMONIUM SULFATE AND AMMONIUM SULFATE–SUCROSE MIXED PARTICLES

3.1: Introduction

Atmospheric submicron aerosol particles play an important role in air quality, climate and public health.[45, 219, 220] The role of alkyl amines in atmospheric aerosol chemistry is of interest due to the unexpectedly high amounts of aminium salts detected in ambient aerosol particles.[76, 221-223] These amounts are out of proportion to the relative amounts of amine and ammonia detected in the atmosphere, since small chain alkyl amines are typically present at concentrations several orders of magnitude lower than ammonia in the gas phase.[79] Ammonia is known to form or contribute substantially to inorganic aerosols by neutralizing atmospheric acids, while amines are receiving growing attention for their potential role in new particle formation.

One pathway through which amines partition from the gas phase into particles is reactive uptake by ammonium sulfate aerosols. Various studies have reported the displacement of ammonium by an alkyl aminium ion. Earlier reports investigated the reaction at low pressure under conditions with limited water.[84, 224] Qiu et al.[224] studied the heterogeneous uptake of methylamine, dimethylamine and trimethylamine vapor by ammonium sulfate and ammonium bisulfate coatings on glass tubes at low pressure and low RH, reporting initial uptake coefficients of $(2.6 - 3.4)\times10^{-2}$ and steady-state uptake coefficients of $(2.3 - 60)\times10^{-4}$. Liu et al.[84] studied the displacement of ammonium from various powdered ammonium salts by aqueous methylamine vapor at very low pressure to report uptake coefficients of $2.3\times10^{-3} – 1.8\times10^{-2}$.

Several studies have reported investigations of amine uptake reactions by ammonium sulfate and other particles.[81, 225, 226] Chu and Chan[12] reported measurements of the reactive uptake of dimethylamine by crystalline or aqueous ammonium sulfate (AS) and AS-sucrose mixed particles. The net reaction is:

$$(CH_3)_2NH\,(g) + NH_4^+\,(aq) \longrightarrow (CH_3)_2NH_2^+\,(aq) + NH_3\,(g) \quad \textbf{(1)}$$

They performed their experiments under conditions of controlled relative humidity (RH) and observed that the amine/ammonium exchange reaction appeared to be water and bulk–diffusion limited. Chu and Chan[12] also reported visual observations and Raman spectroscopic data consistent with the presence of liquid–liquid phase separation in their mixed ammonium sulfate–sucrose micron–sized particles. Sucrose is a widely used surrogate for the hydrophilic organic component of secondary organic aerosol (SOA) particles.

SOA can adopt liquid, semi–solid or glassy phase states depending on chemical composition, temperature and RH.[5, 36, 38, 61, 88] Phase state and associated particle viscosity may affect crucial atmospheric aerosol processes such as ice nucleation,[129] gas uptake and particle growth both in terms of magnitude and characteristic timescales.[227] The presence of a viscous semisolid or glassy phase state can limit reactive uptake by reducing mass transfer and bulk diffusion in aerosol particles.[1, 66, 104, 108, 113, 228, 229] Particle morphology is another important factor affecting uptake processes. It has traditionally been assumed that aerosol particles are homogeneously well-mixed. However, phase separation into two or more liquid or viscous amorphous phases has been observed both in aerosol particles containing organic and inorganic components mixed with water, as well as electrolyte–free aqueous organic particles.[20, 230-233] Phase–separated particles can adopt either a core–shell morphology, in which one phase completely engulfs a second phase, or a partial–engulfing structure, in which both phases

maintain direct contact with the gas phase over some surface area.[77] Several studies have demonstrated that the presence of an SOA coating on particles in a core–shell morphology will lead to a substantial decrease in the uptake of gaseous species.[56, 58, 234]

In this study we investigate the amine/ammonium displacement reaction in particles containing different morphologies and phases using kinetic and thermodynamic modeling to further constrain the reaction mechanism and develop an understanding of limiting processes. A kinetic multi–layer model facilitates the systematic investigation of the reaction over a range of particle sizes, compositions and environmental conditions. Such information can be useful in setting up future experiments and helps in determining priorities for field measurements.

3.2: Methods

3.2.1: Summary of previous experimental work

Our model was applied to previously reported experimental data from Chu and Chan, briefly described in the following.[12] Single particles were generated from aqueous solutions of ammonium sulfate (AS) and sucrose with the following sucrose molar fractions on a dry basis: F_{Su} = 0.00, 0.15, 0.28 and 0.50. Particles were levitated in an electrodynamic balance (EDB) and their dry diameters were recorded after drying at low RH (<5%). Each particle was then equilibrated at a specified RH value (RH < 5% and RH = 10, 20, 30 and 70%) in the EDB at a temperature of 297±1 K. Initial particle diameters were in the range of 37–71 μm. Output from the EDB was recorded during exposure to a constant flow of dimethylamine (DMA, 1 ppm) gas to determine changes in particle mass, size, phase state and chemical composition due to DMA uptake. Particles were characterized with a Raman spectroscopic system coupled to the EDB. After each experimental run, particles were dried and visually inspected under a microscope.

3.2.2: Model description

Kinetic modeling was utilized to investigate the reactive uptake of DMA by AS and mixed AS–sucrose particles. The change in mass of each particle, expressed as the ratio of the particle mass at each time point relative to its initial mass, was simulated using the kinetic multi-layer model of gas–particle interactions in aerosols and clouds (KM-GAP).[4] Schematics of the kinetic model are provided in Figure 3.1. For the simulation of single particle experiments from Chu and Chan, a spherical geometry was applied.[12] The model treats the gas phase with two layers: a quasi–continuous gas phase and a near–surface gas phase layer. Multiple layers represent the condensed phase: sorption layer, surface layer, and a variable number of bulk layers. KM–GAP treats the following mass transport processes explicitly: gas–phase diffusion, adsorption and desorption, surface–bulk exchange, and bulk diffusion. The chemical reaction (**1**)

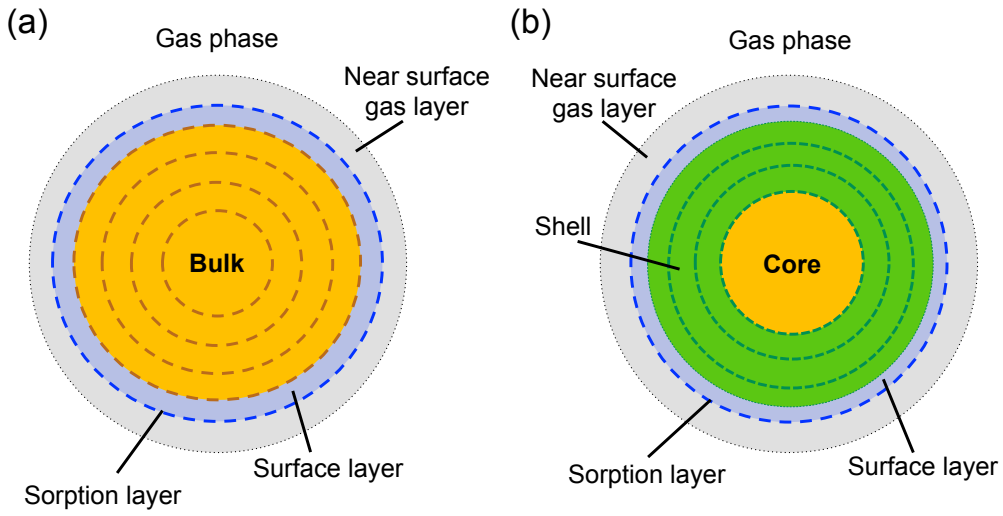

Figure 3.1. Schematics of the kinetic multilayer model of gas–particle interactions (KM–GAP) for (a) ammonium sulfate (AS) particles and (b) mixed AS–sucrose particles. The sorption layer is represented by the blue dashed line. In the mixed particles, the core is treated with an AS–rich phase that is either crystalline or aqueous depending on RH and the shell is initialized as a sucrose–rich phase based on phases and composition data from experiments as well as predictions from AIOMFAC–based equilibrium thermodynamics.

was treated in the surface and bulk layers. The model layer thicknesses changed as the simulation experiment proceeded due to solvation of DMA, mass transport between layers, and the conversion of reactants into products, leading to particle growth.

Model components and treatment of particulate water

For the pure AS particles (Figure 3.1a), the model treats the reactants and products (ammonia and dimethylaminium sulfate (DMAS)) of the DMA/AS exchange reaction. For the mixed particles, sucrose is also included. AS, DMAS and sucrose are hygroscopic.[14] The number of associated water molecules is related to the amount of each component present and remains constant at each RH. Since water molecules are expected to remain closely associated with specific components in the model, we chose to associate the mass and volume of water in non–crystalline layers with these components for simplicity rather than treating water explicitly. The amounts of associated water for AS, DMAS and sucrose are summarized in Table 3.1. AS and DMAS associated water values were optimized for the pure AS particles using the approach from Chu and Chan as a starting point.[12] The same values were also used for the mixed particles. For the mixed AS–sucrose particles, water associated with sucrose was constrained to

Table 3.1. Associated water expressed as the ratio of water molecules to each molecule of indicated component used in KM–GAP modeling for species in non-crystalline layers. The same AS and DMAS associated water values were used for both AS–only and AS–sucrose mixed particles. For the AS-sucrose mixed particles, water associated with sucrose was calculated to be consistent with mole fractions predicted by AIOMFAC.[13]

RH	1%	10%	20%	30%	70%
AS	1.0×10^{-2}	0.1	0.2	0.8	6.4
DMAS	0.1	1.0	2.1	3.7	11.8
Sucrose	5.5×10^{-2}	0.6	1.1	1.8	6.1

be consistent with mole fractions determined by the Aerosol Inorganic–Organic Mixtures Functional groups Activity Coefficients (AIOMFAC) based equilibrium model.[13]

Ammonium sulfate only particles

At RH < 70%, the initial AS particles were observed to exist in crystalline form.[12] Previous studies have shown that there are surface–adsorbed water molecules on AS particles below the deliquescence RH.[14, 235, 236] The initial thickness of this layer can range from less than one monolayer (on average) to multiple monolayers depending on RH as summarized in Table 3.2 and implemented in KM–GAP.

Table 3.2. Monolayers of water present on ammonium sulfate at different RH values.[14]

RH (%)	1	10	20	30	70
Monolayers of H_2O	0.01	0.6	2.6	4.6	3.4

After particle equilibration, the adsorbed water layer would be saturated with AS. Using the associated water ratios in Table 3.1 with the volume of the surface layer, the initial amount of dissolved AS was calculated. For simplicity, mass transport to and from the bulk was allowed only for AS, so the particle bulk decreased in size as AS reacted and DMAS formed in the surface layer. At 70% RH the initial phase of the particle was observed to be liquid in experiments. The volumes of the associated water and the measured dry particle radius were combined to determine the initial aqueous particle volume and diameter.

Kinetic parameters are summarized in Tables 3.3–3.5 that include the gas-phase diffusion coefficient (D_g), surface accommodation coefficient on a free substrate (α_0), desorption lifetime (τ_d), second-order surface (k_{sslr}) and bulk (k_{br}) reaction rate coefficients for reaction (**1**), Henry's law coefficient of DMA in water (5.0×10^{-2} mol cm^3 atm^{-1})[237], and bulk diffusion coefficients

(D_b) for DMA, AS, NH_3 and DMAS. We assumed α_0 of unity and τ_d of nanoseconds for DMA. A first–order approximation of Fick's diffusion equation using bulk diffusion coefficients was utilized to describe mass transport fluxes between the layers. D_b were varied to optimize the model predictions in comparison to the experimental data. For an initially aqueous particle at 70% RH, the chemical reaction would take place in both surface and bulk layers. A second–order reaction rate coefficient between DMA and NH_4^+ of 1.0×10^{-15} cm^3 s^{-1} was used, but predicted

Table 3.3. General parameters used for KM–GAP. Values are for all species unless otherwise indicated.

Parameter	Description	Units	Value	Range	Source
D_g	Gas diffusion coefficient	cm^2 s^{-1}	0.1	-	EPA tools for online site assessment
α_0	Surface accommodation coefficient on free substrate	-	1	-	Shiraiwa et al., Nat. Commun., 8, 150021-150027 (2017)
T_d	Desorption lifetime	s	(DMA) $1.00x10^{-9}$ (NH_3) insensitive	-	Shiraiwa et al., Nat. Commun., 8, 150021-150027 (2017)
k_{sslr} and k_{br}	reaction rate constant for reaction **(1)**	cm3 s-1	$1.00x10^{-15}$	$1.00x10^{-10}$–$1.00x10^{-17}$	fitting parameter
H	Henry's law coefficient	mol cm^3 atm^{-1}	$5.00x10^{-2}$	$4.75x10^{-2}$–$5.25x10^{-2}$	Sander, Atmos. Chem. Phys., 15, 4399-4981 (2015)

Table 3.4. Input parameters for ammonium sulfate only particles.

	Initial dry radius (cm)	Bulk diffusion coeff (cm^2 s^{-1})
Fsu=0.00 (AS only)		
1%	$2.8x10^{-3}$	$1.25x10^{-11}$
10%	$2.35x10^{-3}$	$6.25x10^{-11}$
20%	$2.35x10^{-3}$	$1.50x10^{-10}$
30%	$2.00x10^{-3}$	$1.50x10^{-10}$
70%	$2.45x10^{-3}$	$5.00x10^{-6}$

Table 3.5. Input parameters for mixed AS–sucrose particles.

	Initial dry radius (cm)	Bulk diffusion coeff. ($cm^2\ s^{-1}$)		n_delta** (mol/m^3)	n_alpha** (mol/m^3)	n_beta** (mol/m^3)	[AS] core (mol/cm^3)	[AS] shell (mol/cm^3)	[Sucrose] core (mol/cm^3)	[Sucrose] shell (mol/cm^3)
F_{su}=0.15										
1%	2.1×10^{-3}	1.20×10^{-10}	AS	8.49×10^{-8}	0	7.72×10^{-11}	4.56×10^{21}	9.01×10^{18}	0	1.75×10^{21}
			Su	0	0	1.50×10^{-8}				
			H_2O	0	0	8.33×10^{-10}				
10%	2.25×10^{-3}	1.70×10^{-9}	AS	8.49×10^{-8}	0	9.48×10^{-11}	4.56×10^{21}	1.08×10^{19}	0	1.70×10^{21}
			Su	0	0	1.50×10^{-8}				
			H_2O	0	0	8.38×10^{-9}				
20%	2.15×10^{-3}	4.00×10^{-9}	AS	8.49×10^{-8}	0	1.22×10^{-10}	4.56×10^{21}	1.35×10^{19}	0	1.65×10^{21}
			Su	0	0	1.50×10^{-8}				
			H_2O	0	0	1.72×10^{-8}				
30%	3.55×10^{-3}	7.00×10^{-9}	AS	8.48×10^{-8}	0	1.65×10^{-10}	4.56×10^{21}	1.76×10^{19}	0	1.60×10^{21}
			Su	0	0	1.50×10^{-8}				
			H_2O	0	0	2.70×10^{-8}				
70%	2.5×10^{-3}	1.00×10^{-6}	AS	0	8.01×10^{-8}	4.89×10^{-9}	2.44×10^{21}	3.69×10^{20}	6.49×10^{16}	1.13×10^{21}
			Su	0	2.13×10^{-12}	1.50×10^{-8}				
			H_2O	0	5.08×10^{-7}	1.22×10^{-7}				
F_{su}=0.28										
1%	2.55×10^{-3}	2.00×10^{-10}	AS	7.19×10^{-8}	0	1.44×10^{-10}	4.56×10^{21}	9.01×10^{18}	0	1.75×10^{21}
			Su	0	0	2.80×10^{-8}				
			H_2O	0	0	1.56×10^{-9}				
10%	1.85×10^{-3}	1.50×10^{-9}	AS	7.18×10^{-8}	0	1.77×10^{-10}	4.56×10^{21}	1.03×10^{19}	0	1.64×10^{21}
			Su	0	0	2.80×10^{-8}				

	Initial dry radius (cm)	Bulk diffusion coeff. ($cm^2\ s^{-1}$)		n_delta** (mol/m^3)	n_alpha** (mol/m^3)	n_beta** (mol/m^3)	[AS] core (mol/cm^3)	[AS] shell (mol/cm^3)	[Sucrose] core (mol/cm^3)	[Sucrose] shell (mol/cm^3)
			H_2O	0	0	3.85×10^{-8}				
20%	2.25×10^{-3}	4.50×10^{-9}	AS	7.18×10^{-8}	0	2.29×10^{-10}	4.56×10^{21}	1.35×10^{19}	0	1.65×10^{21}
			Su	0	0	2.80×10^{-8}				
			H_2O	0	0	3.21×10^{-8}				
30% (b)	2.70×10^{-3}	1.00×10^{-8}	AS	7.17×10^{-8}	0	3.08×10^{-10}	4.56×10^{21}	1.76×10^{19}	0	1.60×10^{21}
			Su	0	0	2.80×10^{-8}				
			H_2O	0	0	5.05×10^{-8}				
30% (a)	2.15×10^{-3}	1.00×10^{-8}	AS	7.17×10^{-8}	0	3.08×10^{-10}	4.56×10^{21}	1.76×10^{19}	0	1.60×10^{21}
			Su	0	0	2.80×10^{-8}				
			H_2O	0	0	5.05×10^{-8}				
70%	2.15×10^{-3}	1.00×10^{-6}	AS	0	6.29×10^{-8}	9.13×10^{-9}	2.44×10^{21}	3.69×10^{20}	6.49×10^{16}	1.13×10^{21}
			Su	0	1.67×10^{-12}	2.80×10^{-8}				
			H_2O	0	3.99×10^{-7}	2.27×10^{-7}				
F_{su}=0.50										
1%	2.30×10^{-3}	2.30×10^{-3}	AS	4.97×10^{-8}	0	2.58×10^{-10}	4.56×10^{21}	9.01×10^{18}	0	1.75×10^{21}
			Su	0	0	5.00×10^{-8}				
			H_2O	0	0	2.78×10^{-9}				
10%	2.05×10^{-3}	2.05×10^{-3}	AS	4.97×10^{-8}	0	3.16×10^{-10}	4.56×10^{21}	1.08×10^{19}	0	1.70×10^{21}
			Su	0	0	5.00×10^{-8}				
			H_2O	0	0	2.79×10^{-8}				
20%	1.85×10^{-3}	1.85×10^{-3}	AS	4.96×10^{-8}	0	4.08×10^{-10}	4.56×10^{21}	1.35×10^{19}	0	1.65×10^{21}
			Su	0	0	5.00×10^{-8}				

			H_2O	0	0	5.74×10^{-8}				
30%	$2.05\text{x}10^{-3}$	$2.05\text{x}10^{-3}$	AS	4.95×10^{-8}	0	5.49×10^{-10}	4.56×10^{21}	1.76×10^{19}	0	1.60×10^{21}
			Su	0	0	5.00×10^{-8}				
			H_2O	0	0	9.01×10^{-8}				
70%	$2.55\text{x}10^{-3}$	$2.55\text{x}10^{-3}$	AS	0	3.37×10^{-8}	1.63×10^{-8}	2.44×10^{21}	3.69×10^{20}	6.49×10^{16}	1.13×10^{21}
			Su	0	8.94×10^{-13}	5.00×10^{-8}				
			H_2O	0	2.14×10^{-7}	4.06×10^{-7}				
Source	Chu & Chan, J Phys Chem A, 121, 206 (2017)	fitting parameter		AIOMFAC	AIOMFAC	AIOMFAC	AIOMFAC	AIOMFAC	AIOMFAC	AIOMFAC

**Initial moles of indicated component in the indicated phase before DMA uptake predicted by the AIOMFAC-LLE model. Delta phase corresponds to the solid phase in the hydration case. Beta phase and alpha phase correspond to the sucrose–rich and AS–rich phases, respectively, that are predicted to form in both the hydration and dehydration cases by the thermodynamic model. For further information, please refer to the main article text.

mass ratios were found to be insensitive between the range of 1.0×10^{-10} to 9.0×10^{-17} cm^3 s^{-1}. A single bulk layer was sufficient to describe the solid AS particles (RH<70%), while multiple layers were used for the aqueous bulk at 70% RH. The number of layers was increased until model predictions converged. At 70% RH, experimental data were fitted with a bulk diffusion coefficient of 5.0×10^{-6} cm^2 s^{-1} for DMA and AS. For RH < 70%, experimental data were fitted with DMA and AS bulk diffusion coefficients ranging from 1.5×10^{-10} –1.25×10^{-11} cm^2 s^{-1}.

Ammonium sulfate-sucrose mixed particles

Figure 3.1b shows a schematic of the modeling approach used for the mixed AS–sucrose particles. The modeling approach is consistent with visual observations and Raman spectroscopic data reported by Chu and Chan, implying the presence of a sucrose–rich shell phase in some of these particles.[12] Thermodynamic model predictions also suggest that AS–sucrose particles would be phase–separated (see results section), as also discussed in a previous study.[238] Thus, AS–sucrose particles were modeled assuming a viscous, multi–layered, sucrose–rich, outer shell and a monolayered AS core at RH < 70% (Figure 3.1b). Activity coefficients from a thermodynamic model prediction of particle hydration were used to set initial conditions for a solid AS core and semi–solid sucrose shell containing a small amount of dissolved AS. At 70% RH, activity coefficients from the dehydration case (AIOMFAC–based prediction) were used to set initial conditions for a homogeneously mixed aqueous ammonium sulfate core and the viscous, aqueous sucrose shell in KM–GAP. At all RH values below 70%, the DMA/ammonium exchange reaction (**1**) was considered in the sucrose–rich shell phase and mass transport from/to the core was only considered for ammonium sulfate. For 70% RH, the chemical reaction and diffusion of all components were considered throughout the particle.

Kinetic parameters are listed in Tables 3.3–3.5. The number of layers in the shell was increased until model predictions converged. For the mixed ammonium sulfate–sucrose particles, initial particle diameters ranged from 37–71 μm. The bulk diffusion coefficients at 70% RH for F_{Su} = 0.15, 0.28 and 0.50 were set to 1.0×10^{-6} cm^2 s^{-1}, consistent with an aqueous particle.[1] For RH<70%, experimental data were fit well with bulk diffusion coefficients ranging from 2.0×10^{-10} – 1.0×10^{-8} cm^2 s^{-1}.

3.2.3: Thermodynamic Modeling

The Aerosol Inorganic-Organic Mixtures Functional groups Activity Coefficients (AIOMFAC) thermodynamic group-contribution model, described elsewhere in detail,[13, 239] was used to estimate the degree of non–ideal mixing among condensed–phase species in liquid/amorphous phases and to consider the potential for liquid–liquid phase separation within the AS–sucrose system as a function of equilibrium relative humidity. The AIOMFAC–based model employed in this study included a version of the liquid–liquid equilibrium (LLE) algorithm by Zuend and Seinfeld,[240] which predicts the phase compositions of up to two liquid phases for a given overall composition of a mixture based on the activity coefficients computed by AIOMFAC for the variable composition of each individual phase. Furthermore, the solid–liquid equilibrium of crystalline AS with AS dissolved in an aqueous (sucrose–rich) phase was also solved numerically based on the method described in Hodas et al.[239] The molar input concentrations were determined using the mole fractions of sucrose and ammonium sulfate in the dry particles, and the relative humidity at which each particle was equilibrated before exposure to DMA were used to specify the initial mixture composition. The equilibrium computations were carried out for a constant temperature of 297.15 K, representative of the experimental

conditions. The AIOMFAC–based LLE model predictions for the equilibrium phase compositions of liquid particle phases α and β, and solid AS phase δ (where applicable), as well as associated component activity coefficients were then used as input parameters to constrain the kinetic model simulations with KM–GAP.

3.2.4: Field measurements

We analyzed particle and gas phase concentrations of ammonia and amines measured during the Holistic Interactions of Shallow Clouds, Aerosols and Land Ecosystems (HI–SCALE) field campaign in north–central Oklahoma in the summer of 2016.[241] Gas phase amines were measured by ambient pressure proton transfer mass spectrometry.[242] Concomitant measurements of size-resolved nanoparticle composition were performed during HI-SCALE by Thermal Desorption Chemical Ionization Mass Spectrometry (TDCIMS).[78] Calibrations were performed during the campaign using either atomized ammonium sulfate or dimethylaminium sulfate particles to associate signal intensity to collected sample mass. The average relative humidity measured during this campaign was 72 ± 18% (1σ), with peaks in relative humidity at night.

3.3: Results and Discussion

3.3.1: Pure ammonium sulfate particles

Figure 3.2a shows experimental data from Chu and Chan and modeled particle mass ratio for the pure ammonium sulfate particles as a function of exposure time to DMA. The particle mass ratio is defined as the mass of the particle at time t relative to that at time 0 (t_0). Particle mass ratios increase at different rates depending on RH until they reach a plateau at the completion of the DMA/ammonium displacement reaction. The rate of particle growth was

fastest for the aqueous particle at 70% RH and sensitivity studies revealed that for this condition, growth is limited only by gas–phase diffusion of DMA.[243] The bulk diffusion coefficients of DMA increase as RH increases, leading to higher rates of reaction and particle growth rates. The model simulations reveal that predicted mass ratios are sensitive to the Henry's law coefficient, the bulk diffusion coefficient of DMA, and the initial concentration of AS in the surface layer. Therefore, the availability of DMA and AS in the surface layer during the initial stages of DMA uptake controls the rate of particle growth. At 30% RH the particle mass ratio reaches a plateau at a high value, as the particle undergoes a phase transition from solid to liquid due to DMAS

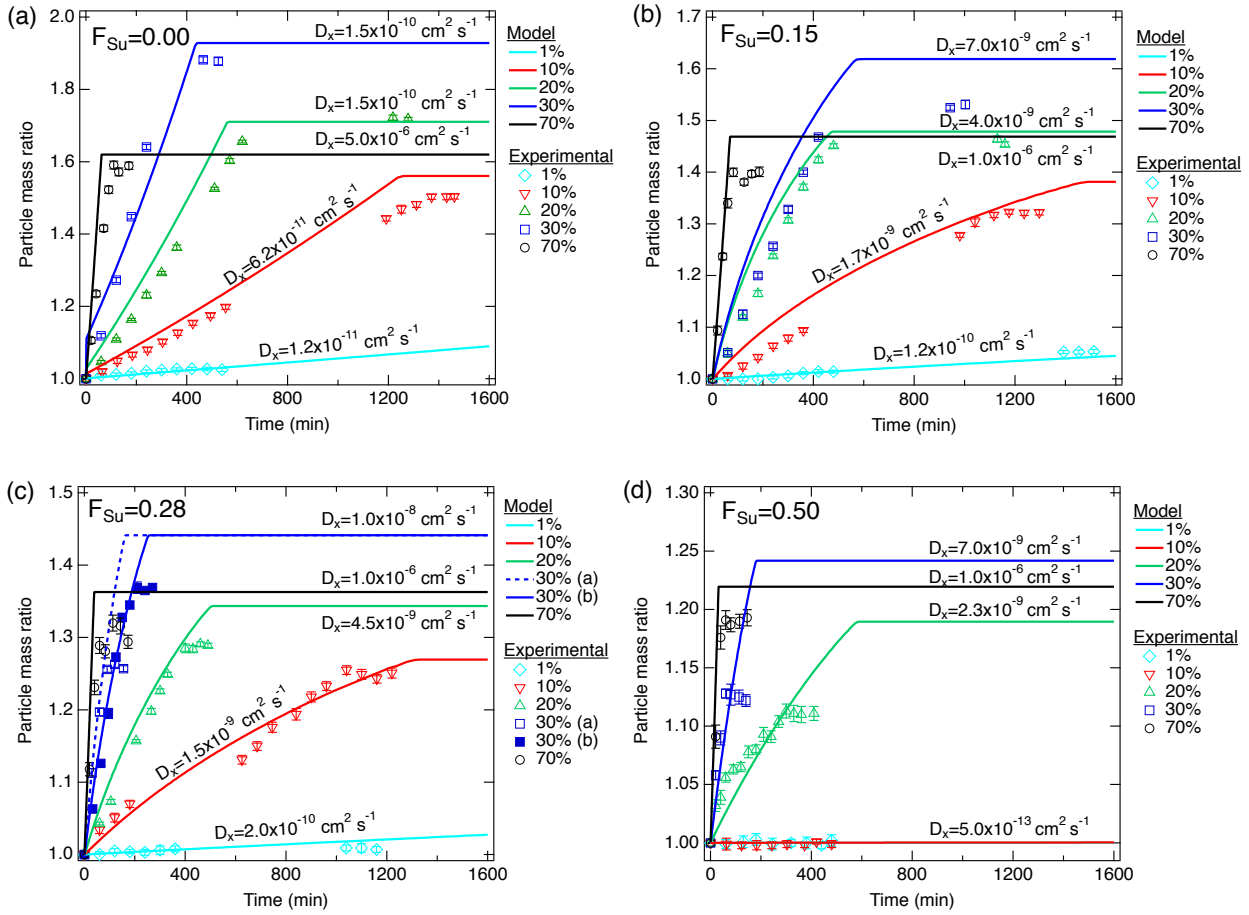

Figure 3.2. Temporal evolution of particle mass ratio upon DMA exposure as measured by Chu and Chan[12] (markers) and simulated by KM-GAP (solid lines). The sucrose fraction in an AS–sucrose particle is (a) F_{Su} = 0.00 (AS only), (b) F_{Su} = 0.15, (c) F_{Su} = 0.28, and (d) F_{Su} = 0.50 at different RH levels of 1% (cyan), 10% (red), 20% (green), 30% (blue), and 70% (black) and a temperature of 297.15 K.

formation and associated water uptake. This phase transition leads to an enhancement in the liquid particle mass relative to the dry mass at time zero, which is different from the case

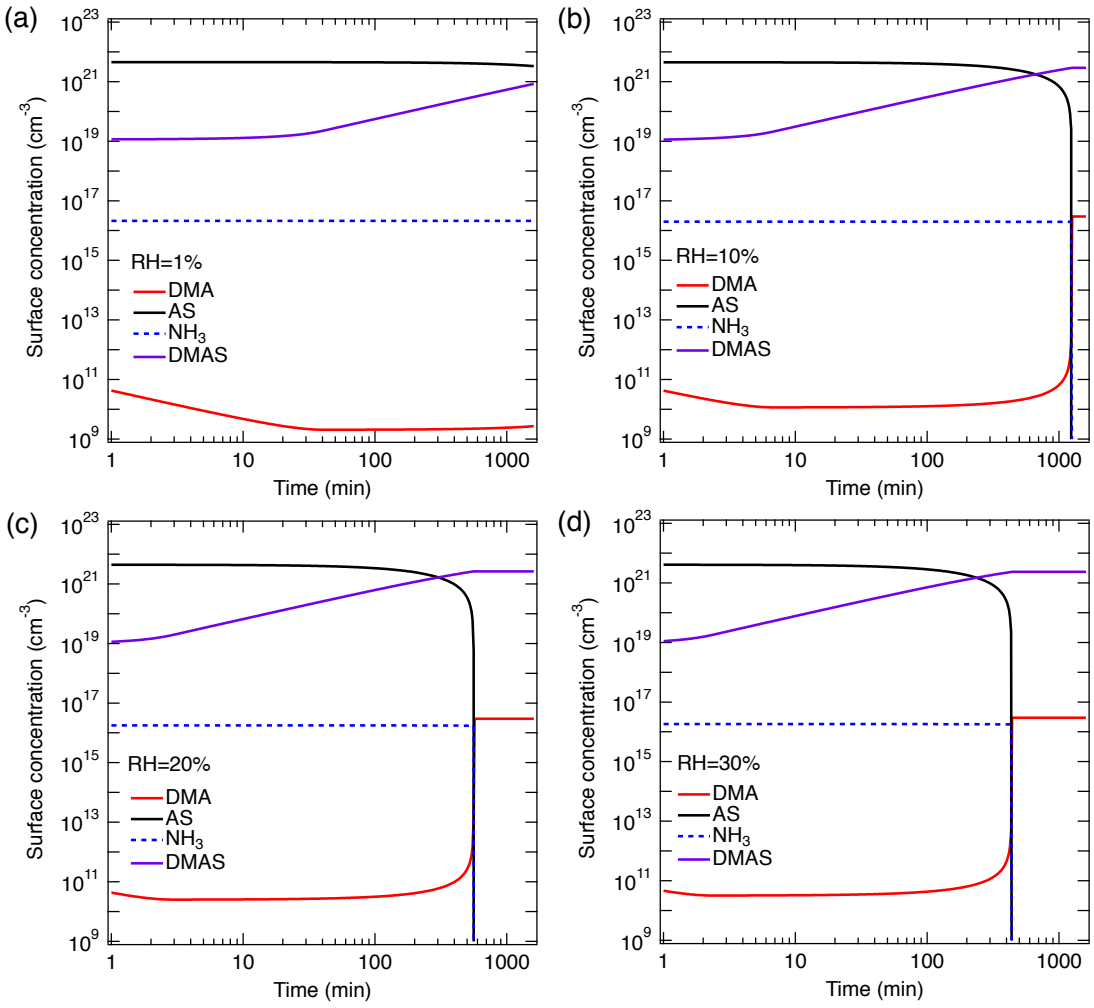

Figure 3.3. Concentrations (molecules per cm^3) of DMA (red), AS (black), NH_3 (dashed blue) and DMAS (purple) in the surface layer during DMA uptake by an AS particle at RH of (a) 1%, (b) 10%, (c) 20% and (d) 30%.

at 70 % RH, in which no phase transition occurs. Chu and Chan observed that the particle phase gradually transformed from crystalline solid into liquid during DMA uptake judging from the 90° Mie scattering pattern and Raman spectrum of the particle.[12]

The temporal evolution of concentration of each component over time in the surface layer is shown in Fig. 3.3. While a minimal decrease in AS concentration is observed for RH < 5%

(Fig. 3.3a), the reaction proceeds to completion at all other RH values and the AS concentration drops to zero as the DMAS concentration plateaus. A drop in DMA concentration (red line) may be observed while the exchange reaction proceeds due to the volume of the surface layer growing, while the rate of DMA accommodation to this layer remains relatively constant. Once the reaction reaches completion in Figs. 3.3b–d, the DMA concentration begins to increase until it reaches the saturation concentration. The concentration of NH_3 in the surface layer (dotted blue

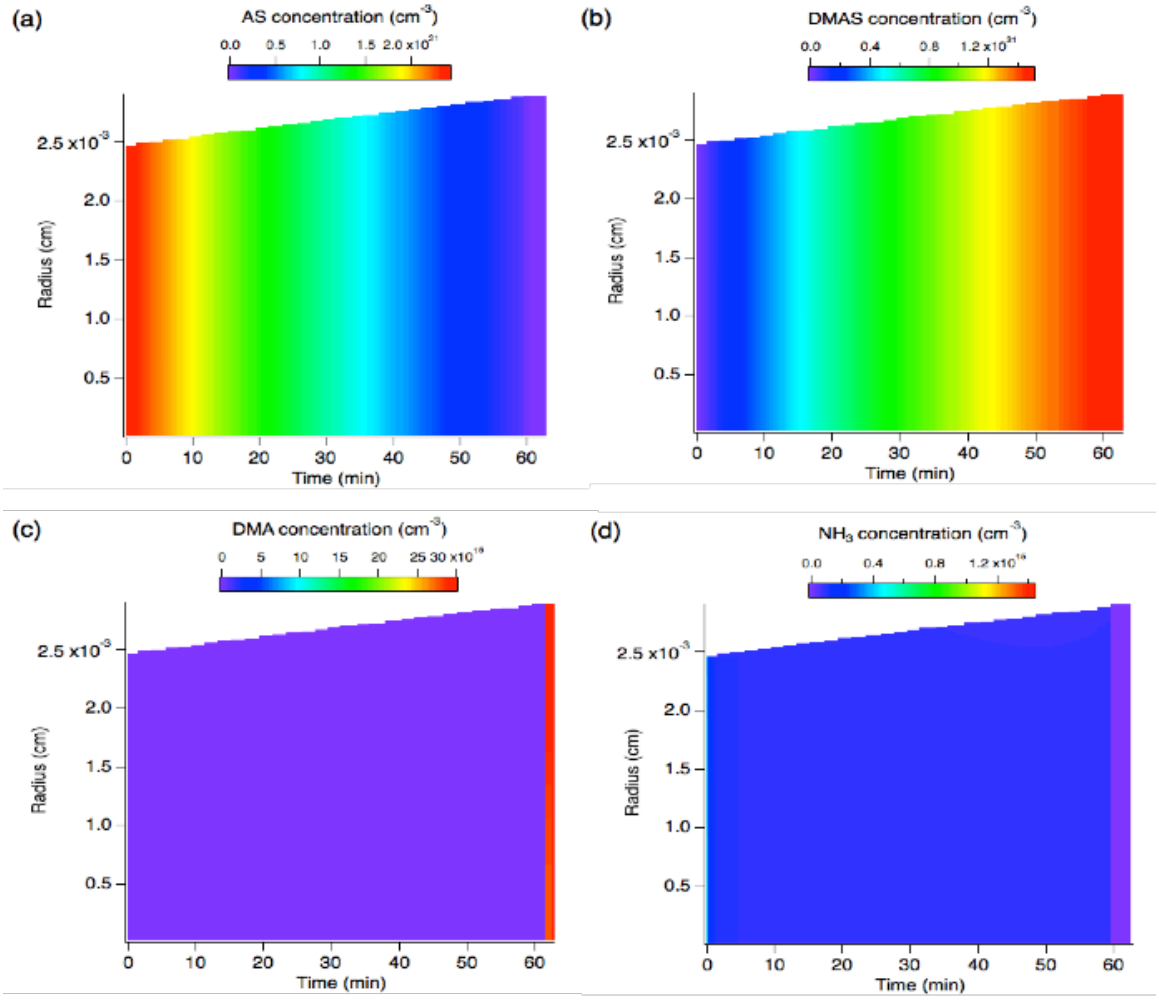

Figure 3.4. Bulk concentration profiles of (a) AS, (b) DMAS, (c) DMA and (d) NH_3 when an AS particle is exposed to DMA at 70% RH.

line) remains constant while the reaction is occurring as determined by the balance between formation and evaporation but drops to zero due to particle–to–gas partitioning once the reaction has reached completion.

The temporal evolution of bulk concentration profiles of components for the aqueous particle at 70% RH is provided in Fig. 3.4 as a function of reaction time (x–axis) and distance from the particle center (y–axis). The concentration of AS (Fig. 3.4a) decreases commensurate with an increase in the concentration of DMAS (Fig. 3.4b). Since the particle is initially aqueous, all AS is dissolved and no diffusion limitation is observed. A low concentration of DMA is present until the reaction reaches completion, as DMA diffusing into the particle bulk is rapidly consumed by the exchange (Fig. 3.4c). The concentration of NH_3 (Fig. 3.4d) in the particle is constant until the reaction completes. It then drops due to particle–to–gas partitioning as observed in the surface layer.

3.3.2: Mixed ammonium sulfate–sucrose particles

Fig. 3.5 shows the mass fractions of the components in the AS/sucrose/water system at time zero as predicted by the AIOMFAC–LLE model for the case with a dry molar sucrose fraction of F_{Su} = 0.15. Thermodynamic equilibrium computations were conducted for both dehydration and hydration cases. In the dehydration case starting from high RH conditions with all components in a liquid/amorphous phase, a metastable, supersaturated salt solution is considered and crystallization suppressed in the calculations (Fig. 3.5b), while in the hydration case, starting at low RH, AS is allowed to adopt a crystalline physical state below its predicted complete deliquescence at ~79% RH (Fig. 3.5a). In the hydration case, AS is predominantly partitioned to the solid phase (δ) while sucrose is found in a separate amorphous/liquid phase

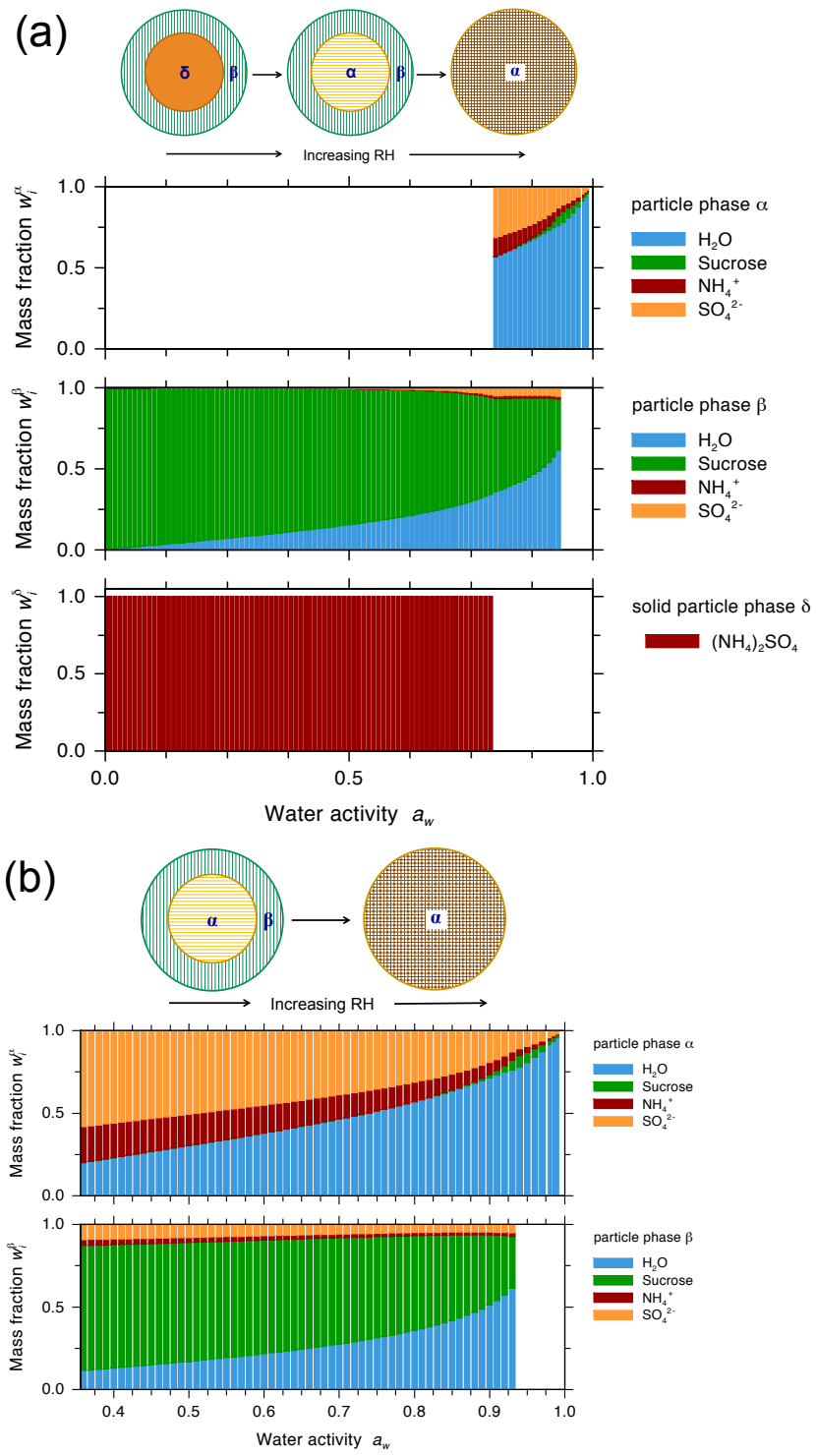

Figure 3.5. Predicted equilibrium phase compositions in mass fractions for aqueous mixtures of AS and sucrose as a function of water activity (equilibrium RH) at 297.15 K. (a) Hydration case: a solid–liquid equilibrium is predicted between a solid AS phase (δ; lowest panel) and an aqueous, sucrose–rich phase (β; middle panel) up to 70% RH, followed by liquid–liquid phase separation (coexisting phases α and β) and merging into a single liquid phase at RH > 93% (b) In the dehydration case, formation of solid AS is suppressed, extending the liquid–liquid phase separation range to lower RH, with both phases becoming AS–supersaturated below 79% RH.

that further contains water and small amounts of dissolved AS (in solid–liquid equilibrium) up to the complete AS deliquescence at ~79% RH. Two liquid phases, one AS–rich (α) phase and one sucrose–rich (β) phase are predicted to coexist between 79% < RH < 94% in the hydration case. For the dehydration case, liquid–liquid phase separation leads to the formation of AS–rich (α) and sucrose–rich (β) phases at RH < 94% (before AS is expected to crystallize spontaneously at RH ~<36%, not shown in Fig. 3.5b). In the phase–separated regime, a non–negligible fraction of AS is predicted to partition into the sucrose–rich (aqueous) phase, while the aqueous AS–rich phase α is virtually sucrose–free. The exception is the RH range from ~84% – 93%, close to the upper limit of phase separation, in which at least 1% of the total sucrose amount partitions into phase α.

These predicted compositions were used to constrain the initial partitioning of components in KM-GAP. Based on experimental data on aerosol morphologies,[12] KM-GAP treats the AS–rich phase as the core and the sucrose–rich phase as the shell (Fig. 3.1b) and the predicted activity coefficients of the different species in each phase were used to constrain bulk diffusion. For RH < 70%, values from the hydration branch (Fig. 3.5a) were used, while activity coefficients from the dehydration branch (Fig. 3.5b) were used for 70% RH. It should be noted, however, that some of the particles at RH < 70% were observed to remain water–bound and amorphous in the experiment. Figures 3.2b–d show the experimental measurements and modeling results with KM-GAP for the mixed AS–sucrose particles. The particle growth of aqueous mixed particles at 70% RH at all mole fractions of sucrose was limited by gas–phase diffusion. For RH < 70%, the mixed AS–sucrose particles differed from the pure AS particles in that the mixed particles exhibited no sensitivity to the value of the Henry's law coefficient.

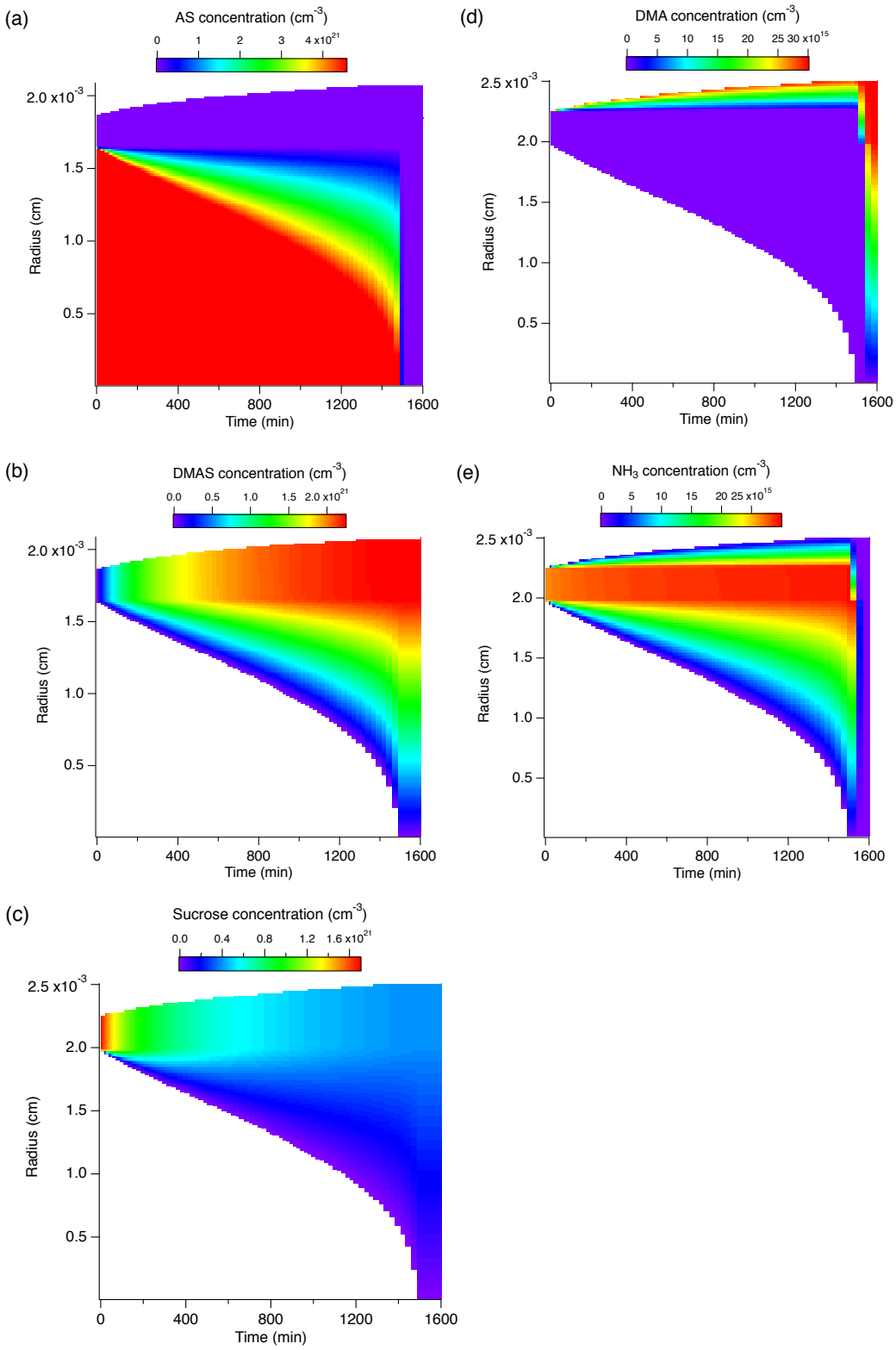

Figure 3.6. (F_{Su} = 0.15, RH = 10%) Concentration (molecules per cm^3) of components in the core and shell of the particle as a function of time (x–axis) and distance from the particle center (y–axis). (a) AS; (b) DMAS; (c) Sucrose; (d) DMA; (e) NH_3. Color bar indicates concentration (molecules cm^{-3}) with red indicating areas of high concentration and blue indicating low concentration.

Instead, the growth of the mixed particles is limited only by the bulk diffusion coefficients of DMA and AS through the sucrose–rich shell.

Figure 3.6 shows bulk concentration profiles of the model components for the particle with $F_{Su} = 0.15$ at 10% RH. The concentration of AS in the sucrose-rich particle shell (Fig. 3.6a) remains low due to slow transport of AS from the AS–rich core to the sucrose–rich shell and loss by the displacement reaction. As the reaction progresses and the particle grows, the AS core decreases in size and the shell volume increases, as exhibited by the plots of DMAS, sucrose and ammonia concentration (Figs. 3.6b, c, e, respectively). The reaction products (e.g., DMAS, NH_3) are mostly concentrated in the outer portion of the particle shell throughout the reaction. Sucrose does not react with DMA so the number of sucrose molecules does not change as the reaction proceeds and the molecular concentration of sucrose decreases due to dilution as the shell volume grows. The concentration of DMA is highest near the surface of the particle, before it encounters AS as it diffuses into the shell. The reaction reaches completion over the experimental time period for all conditions apart from RH < 5% and 10% RH when $F_{Su} = 0.50$. With $F_{Su} = 0.50$ at 10% RH, the increase in particle mass ratio is severely diminished and becomes almost indistinguishable from the RH < 5% case due to strong kinetic limitations of bulk diffusion (with bulk diffusivity < 5.0×10^{-13} cm^2 s^{-1}) in a glassy sucrose–rich shell.

Further indications of kinetic limitations can be found by comparing values of the uptake coefficient for each particle. DMA uptake coefficients (the ratio between net uptake rates to molecular collision rates) calculated from the model are summarized in Table 3.6. It also includes effective uptake coefficients, which are calculated without considering gas–phase diffusion (i.e., collision rates were calculated using average gas–phase concentrations). A large difference between the true and effective uptake coefficients at 70% RH demonstrates the

importance of gas–phase diffusion at high RH, where near–surface gas–phase concentrations are reduced due to large uptake. The order of magnitude values for the effective uptake coefficients (Table 3.6) are consistent with those derived from laboratory experiments, with the largest discrepancy within one order of magnitude.[12] DMA uptake coefficients range from 7.8×10^{-5} to 2.6×10^{-3} for initially solid particles at RH < 70%, while they are 0.70–0.82 for initially aqueous particles at 70% RH.

The modeled uptake coefficients follow similar trends as the reported, experimentally derived values: DMA uptake increases as RH increases for all molar fractions of sucrose. An examination of AS concentrations in the modeled particles reveals that the concentration of AS in the shell increases with increasing RH. The higher AS concentration is consistent with increased solvation of AS with higher water content (as shown in Fig. 3.5), resulting in higher DMA uptake. In general uptake coefficients decrease as the molar fraction of sucrose increases. The plausible explanation for the effect of sucrose is a change in viscosity of the shell layer. The higher viscosity of sucrose–containing aqueous solutions at intermediate and low RH has been well-documented.[121] As the relative amount of sucrose in the particle increases, the higher viscosity of the sucrose–rich layers would affect bulk diffusion of DMA.

Table 3.6. Modeled true and effective (in brackets) uptake coefficients (γ) for dimethylamine.

	Relative humidity (%)				
F_{Su}	**1**	**10**	**20**	**30**	**70**
0.00	7.75×10^{-5} (7.59×10^{-5})	3.87×10^{-4} (3.54×10^{-4})	9.27×10^{-4} (7.68×10^{-4})	9.28×10^{-4} (7.86×10^{-4})	0.82 (4.18×10^{-3})
0.15	3.41×10^{-5} (3.38×10^{-5})	3.87×10^{-4} (3.57×10^{-4})	1.23×10^{-3} (0.95×10^{-3})	2.54×10^{-3} (1.27×10^{-3})	0.80 (3.47×10^{-3})
0.28	2.74×10^{-5} (2.71×10^{-5})	2.05×10^{-4} (1.97×10^{-4})	7.08×10^{-4} (7.08×10^{-4})	(a) 2.60×10^{-3} (1.64×10^{-3}) (b) 2.19×10^{-3} (1.37×10^{-3})	0.75 (4.13×10^{-3})
0.50	1.42×10^{-7} (1.42×10^{-7})	1.00×10^{-6} (1.00×10^{-6})	2.78×10^{-4} (2.64×10^{-4})	9.84×10^{-4} (8.18×10^{-4})	0.70 (3.61×10^{-3})

3.4: Atmospheric implications and conclusion

Using the kinetic model, we sought to extrapolate to particle sizes and DMA mixing ratios representative of ambient conditions to assess atmospheric implications. The experiments conducted by Chu and Chan were performed on particles with diameters in the micron range (37–71 μm) at a DMA mixing ratio of 1 ppm. Analysis of particle and gas-phase concentrations of ammonia and amines measured during the Holistic Interactions of Shallow Clouds, Aerosols and Land Ecosystems (HI-SCALE) field campaign in north-central Oklahoma in the summer of 2016 provided values for use as reference.[241] The average mixing ratios of ammonia, DMA and methylamine were 245 ± 47 ppt, 0.813 ± 0.670 ppt and 0.601 ± 0.480 ppt, respectively and significant amounts of aminium salts were detected in 20–40 nm particles.

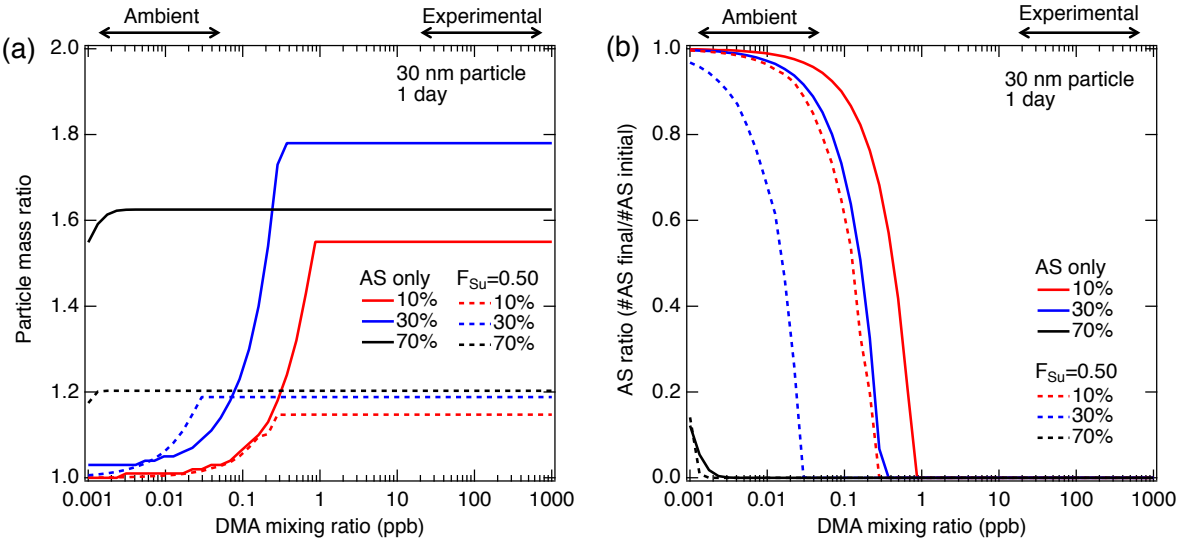

Figure 3.7. (a) Predicted particle mass ratios (particle mass after exposure to DMA divided by initial particle mass) and (b) molar AS ratio (number of AS molecules after DMA exposure divided by initial number of AS molecules) as a function of DMA mixing ratio. Kinetic modeling was used to simulate DMA uptake by pure AS or AS–sucrose (F_{su} = 0.50) particles with 30 nm diameter over 1 day at varying DMA mixing ratios. DMA mixing ratios range from ppt levels found in the atmosphere to ppm levels used in experimental data. A reaction rate coefficient of 1×10^{-15} cm^3 s^{-1} was used for the simulations.

Given this information, we simulated the growth of a 30 nm AS particle over 1 day upon exposure to DMA at mixing ratios varying from typical levels of 1 ppm in laboratory

experiments to the 1 ppt range observed in the HI-SCALE field measurements. The predicted mass ratios as a function of DMA mixing ratio are shown in Fig. 3.7a. Also included is the predicted ratio of remaining AS to initial AS for the same conditions (Fig. 3.7b). Unlike the simulations corresponding to the experimental data, for the significantly smaller atmospherically relevant particle sizes, DMA uptake is sensitive to the reaction rate coefficient as shown by sensitivity tests in Figs. 3.8–3.11. Growth is likely to be limited for atmospherically relevant DMA mixing ratios at lower RH values (Figs. 3.7, 3.8 and 3.10). However in the presence of hydrophilic organics and with a high reaction rate coefficient (~10^{-13} cm^3 s^{-1}) substantial growth would occur (Fig. 3.10). Significant growth is predicted at 70% RH under atmospheric conditions (Figs. 3.7, 3.9 and 3.11) unless the rate coefficient is low (~10^{-17} cm^3 s^{-1}). For the 30 nm particles used for these simulations the increase in mass ratio is no longer limited by gas–phase diffusion at 70% RH; therefore, if we assume a fast reaction rate, the reaction proceeds

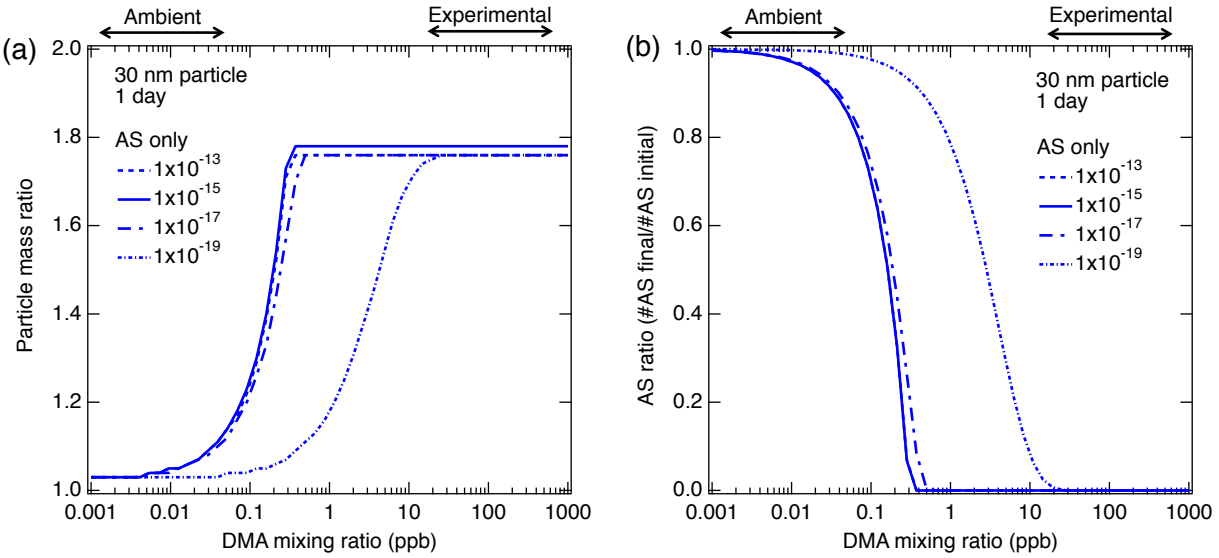

Figure 3.8. Sensitivity of (a) predicted particle mass ratios (particle mass after exposure to DMA divided by initial particle mass) and (b) AS ratio (number of AS after DMA exposure divided by initial number of AS) to variation in the reaction rate coefficient at RH=30%. Kinetic modeling was used to simulate DMA uptake by pure AS particles with 30 nm diameter over 1 day at varying DMA mixing ratios. DMA mixing ratios range from ppt levels found in the atmosphere to ppm levels used in experimental data.

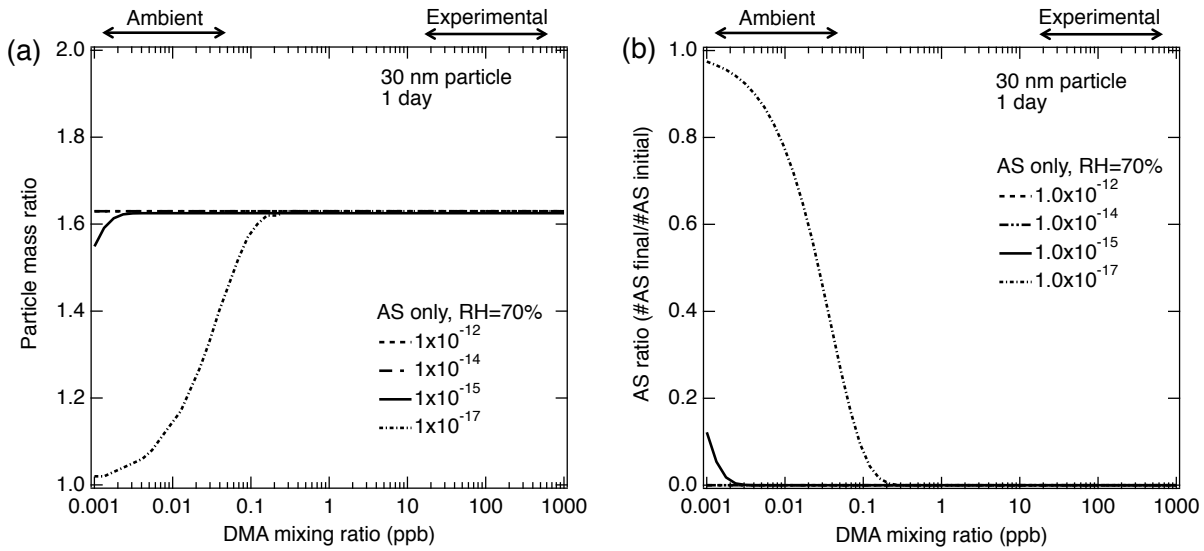

Figure 3.9. Sensitivity of (a) predicted particle mass ratios (particle mass after exposure to DMA divided by initial particle mass) and (b) AS ratio (number of AS after DMA exposure divided by initial number of AS) to variation in the reaction rate coefficient at RH = 70%. Kinetic modeling was used to simulate DMA uptake by pure AS particles with 30 nm diameter over 1 day at varying DMA mixing ratios. DMA mixing ratios range from ppt levels found in the atmosphere to ppm levels used in experimental data.

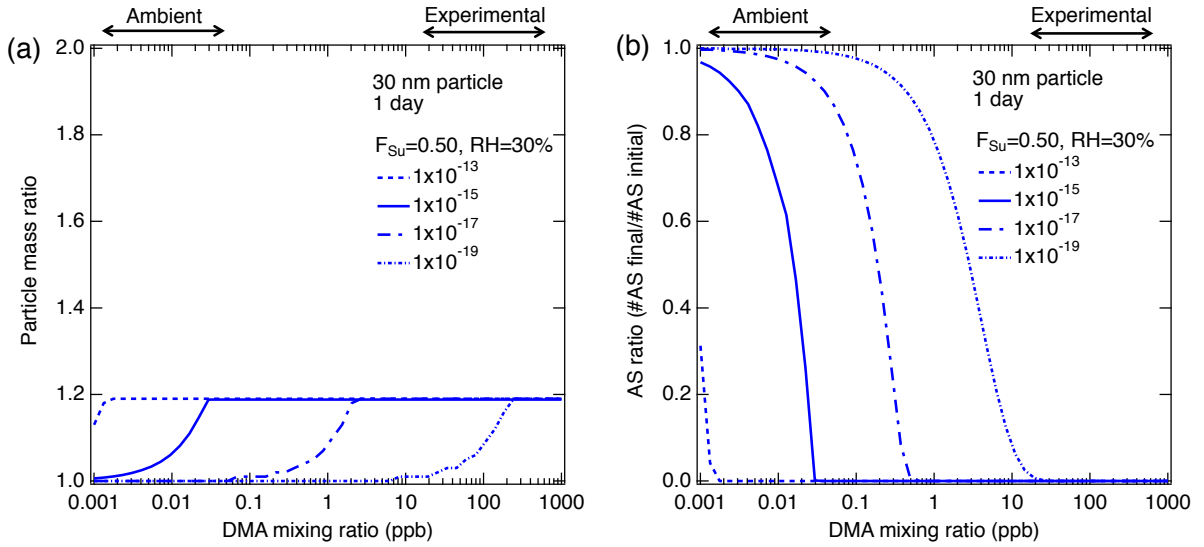

Figure 3.10. Sensitivity of (a) predicted particle mass ratios (particle mass after exposure to DMA divided by initial particle mass) and (b) AS ratio (number of AS after DMA exposure divided by initial number of AS) to variation in the reaction rate coefficient at RH = 30%. Kinetic modeling was used to simulate DMA uptake by AS–sucrose (F_{su} = 0.50) particles with 30 nm diameter over 1 day at varying DMA mixing ratios. DMA mixing ratios range from ppt levels found in the atmosphere to ppm levels used in experimental data.

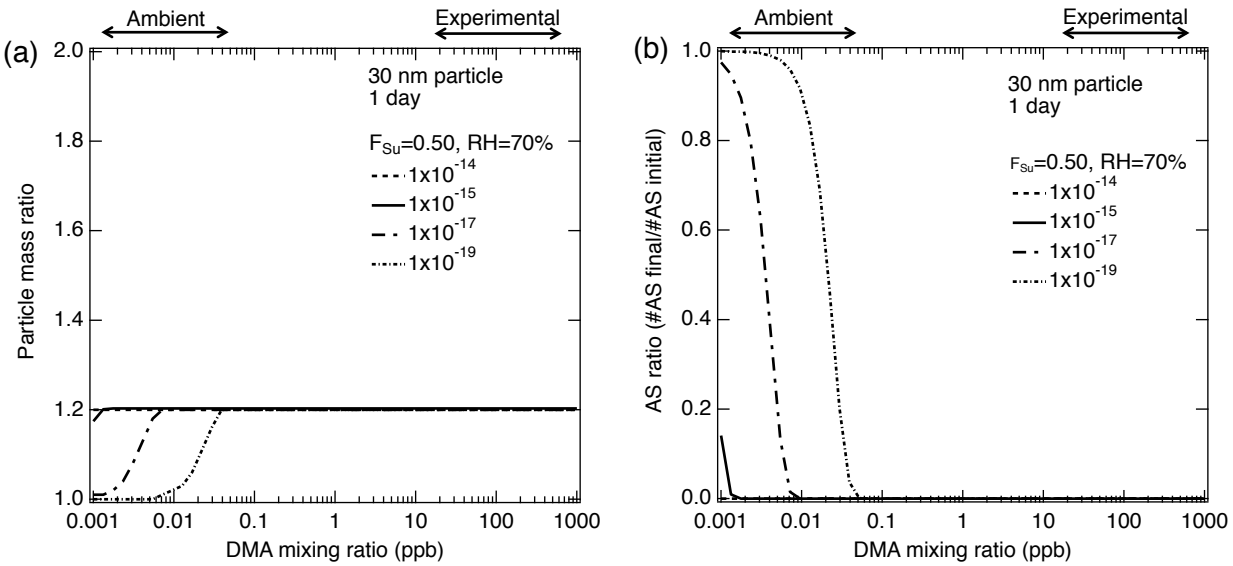

Figure 3.11. Sensitivity of (a) predicted particle mass ratios (particle mass after exposure to DMA divided by initial particle mass) and (b) AS ratio (number of AS after DMA exposure divided by initial number of AS) to variation in the reaction rate coefficient at RH = 70%. Kinetic modeling was used to simulate DMA uptake by AS–sucrose (F_{su} = 0.50) particles with 30 nm diameter over 1 day at varying DMA mixing ratios. DMA mixing ratios range from ppt levels found in the atmosphere to ppm levels used in experimental data.

quickly and reaches completion after one day even at low DMA mixing ratios.[244] This observation also applies to the mixed AS–sucrose particles modeled at a sucrose mole fraction of F_{Su} = 0.50. These results suggest that in locations of high RH, when aerosol particles are in the liquid phase state, amine uptake could result in a mass increase by approximately 20 – 60%, depending on the composition of the particle. However, given the sensitivity of the kinetic model to the reaction rate constant at ambient conditions, measurements of smaller particles are needed to better constrain the reaction rate coefficient in the model.

Further work on smaller particles is required to fully understand the importance of aminium formation on particle growth. The kinetic model described in this paper was motivated by experimental work on simplified mixed particles containing only ammonium sulfate and one organic compound. In contrast, TDCIMS measurements of particulate ammonium in 20–40 nm particles during HI-SCALE found that ~47 wt% of the detected ammonium can be attributed to

ammonium sulfate, suggesting that other counter ions for ammonium exist in particles such as nitrate or deprotonated organic acids. TDCIMS measurements also determined that amine salts could be important constituents of ambient particles. Applying the assumption that the measured DMA and methylamine form neutralized salts with sulfuric acid, HI-SCALE measurements determined that DMA sulfate comprises 20.0 ± 36.8 wt% (uncertainties here indicate standard deviation and not measurement uncertainty) and methylaminium sulfate comprises 20.1 ± 38.1 wt% of 20-40 nm particles, although it is also likely that these strong bases form salts with other particulate anions. These findings from HI–SCALE are consistent with previous field measurements in which 10–47% of TDCIMS–detected positive ions were attributed to aminium salts depending on location.[76] Thus, while the amine/ammonium exchange reaction could contribute to formation of ambient particles, HI–SCALE measurements suggest other ammonium salts are also present in ambient particles and must be considered in future investigations.

It should also be noted that all experiments were conducted at a temperature near 298K. Seasonal fluctuations lead to lower and higher temperatures throughout the world. At lower temperatures, viscosity will increase so particles are expected to become more viscous and kinetic limitations are more likely for DMA uptake, whereas kinetic limitations are not expected at higher temperatures.[34] In addition, geographic location and atmospheric altitude are important as SOA are predicted to be liquid in regions of high RH, semi–solid in the mid–latitudes areas and solid over dry lands, and in the middle and upper troposphere.[34]

CHAPTER 4

LIQUID-LIQUID PHASE SEPARATION AND VISCOSITY WITHIN SECONDARY ORGANIC AEROSOL GENERATED FROM DIESEL FUEL VAPORS

Portions of this chapter are reproduced with permission from: Song, M.; Maclean, A. M.; Huang, Y.; Smith, N. R.; Blair, S. L.; Laskin, J.; Laskin, A.; DeRieux, W. S. W.; Li, Y.; Shiraiwa, M.; Nizkorodov, S. A.; Bertram, A. K., Liquid-liquid phase separation and viscosity within secondary organic aerosol generated from diesel fuel vapors. *Atmospheric Chemistry and Physics Discussions* **2019**, 1-37.

4.1: Introduction

Despite the importance of SOA, many of the physicochemical properties of SOA remain poorly understood, such as viscosity. Viscosity together with the Stokes-Einstein equation can be used to predict diffusion rates of organics within SOA, which can critically impact a number of processes involving SOA. Studies that quantify the viscosity of SOA generated from a complex mixture of VOCs of atmospheric relevance are needed. Methods have been developed to predict the glass transition temperature and viscosity within an organic matrix of atmospheric relevance using molar mass and oxygen to carbon elemental ratio (O:C) or the number of carbon, hydrogen and oxygen atoms of the organic compounds within the organic matrix.[34, 61] In the following, viscosity within SOA particles generated by photooxidation of diesel fuel vapors are predicted based on the methods developed by Shiraiwa et al. (2017)[34] and DeRieux Li et al. (2018)[61] and compared with measured viscosity. [34, 61]

4.2: Predictions of viscosity based on high-resolution mass spectrometry

Viscosity of the diesel fuel SOA was predicted using the elemental composition of the SOA and the methods developed by Shiraiwa et al. (2017)[34] and DeRieux Li et al. (2018).[61] The elemental composition of the diesel fuel SOA were taken from a previous study (Blair et al., 2017)[85] using of SOA generated with identical conditions (DSL/NO_x Table 1 of Blair et al. (2017)). In the previous study by Blair et al. (2017) high-resolution nanospray desorption electrospray ionization mass spectrometry[210] was used to determine the elemental composition.

Shiraiwa et al. (2017) reported a parameterization (Eq. 1) to estimate the glass transition temperature (T_g) of individual CH or CHO compounds with molar mass < ~450 g mol^{-1}.

$$T_g = A + BM + CM^2 + D\,(O{:}C) + E\,M\,(O{:}C) \quad (1)$$

where M is the molar mass and O:C is the ratio of oxygen to carbon atoms. The coefficients are: A = -21.57 (K), B = 1.51 (K mol g^{-1}), C = -1.7×10^{-3} (K mol^2 g^{-2}), D = 131.4 (K) and E = -0.25 (K mol g^{-1}). DeRieux Li et al. (2018)[61] reported another parameterization (Eq. 2) to predict T_g of CH and CHO compounds with molar mass up to ~1100 g mol^{-1} using the number of carbon (n_C), hydrogen (n_H), and oxygen atoms (n_O):

$$T_g = (n_C^0 + ln(n_C))\, b_C + ln(n_H)\, b_H + ln(n_C)\, ln(n_H)\, b_{CH} + ln(n_O)\, b_O + ln(n_C)\, ln(n_O)\, b_{CO} \quad (2)$$

Values of the coefficients [n_C^0, b_C, b_H, b_{CH}, b_O, and b_{CO}] are [1.96, 61.99, -113.33, 28.74, 0, 0] for CH compounds and [12.13, 10.95, -41.82, 21.61, 118.96, -24.38] for CHO compounds.[61] To estimate the T_g for a dry organic mixture ($T_{g,org}$), the relative mass concentration of each compound was assumed to be proportional to its relative abundance in the mass spectrum and the Gordon-Taylor mixing rule was employed with a Gordon-Taylor coefficient (k_{GT}) value of 1 [6].

For the T_g of a mixture of organics and water ($T_{g,mix}$), the effective hygroscopicity parameter (κ) was applied to calculate the mass fraction of water in the SOA particles [162]. A κ value of 0.1 was used for the diesel fuel SOA based on an average O:C of 0.45 for diesel fuel-derived SOA (Fig. S1 and Table S3 in Blair et al. (2017)) and the relationship between O:C and κ reported in Lambe et al. (2011, Fig. 7)[207] and Massoli et al. (2010, Fig. 2)[245]. To estimate the $T_{g,mix}$, the Gordon-Taylor equation was applied with k_{GT} set to 2.5, based on previous studies that suggested 2.5 ± 1.0.[5, 32, 37] Once $T_{g,mix}$ was determined, viscosity was estimated using the

modified Vogel-Tammann-Fulcher (VTF) equation and an assumed viscosity of 10^{12} Pa s at the glass transition temperature ($T = T_g$) and an assumed viscosity of 10^{-5} Pa s at a very high temperature [48, 165]:

$$\log \eta = -5 + 0.434 \frac{T_0 D_f}{T - T_0} \qquad (3)$$

$$\text{where } T_0 = \frac{39.17\, T_g}{D_f + 39.17} \qquad (4)$$

In these equations, D_f is the fragility parameter and T_0 is the Vogel temperature. In our calculations, we assume D_f equal to 10 based on previous studies that showed a lower limit of ~10 (±1.7) as the molar mass increases.[61]

4.3: Comparison with previous measurements and predictions

In Fig. 4.1 the measured viscosities determined from individual poke-and-flow experiments are grouped by RH and compared with the viscosity of SOA generated by the photooxidation of toluene. Toluene SOA is commonly used as a proxy of anthropogenic SOA.[9, 10, 135, 246, 247] The viscosities of the toluene SOA and the diesel fuel SOA are similar. At RH values between 38 and 50 % both have viscosities in the range of approximately 10^4 to 10^8 Pa s while at ≤ 10 % RH, both have viscosities ≥ 1×10^8 Pa s.

In Fig. 4.1, the viscosity of diesel fuel SOA is also compared with predicted viscosities based on O:C and molar mass (Eq. 1) and the number of carbon, hydrogen, and oxygen atoms (Eq. 2). Within the uncertainty of the measurements, the predicted viscosities are consistent with the measured viscosities (Fig. 4.1). Measurements of viscosity with reduced uncertainties would be useful to better test the predictions. Common methods used to measure viscosities (i.e., bulk

viscometers) are more precise than the poke-and-flow technique, but require more material than is typically produced in environmental chambers.[36]

Interestingly, predictions based on the number of carbon, hydrogen, and oxygen atoms (Eq. 2) are almost 3 orders of magnitude higher than predictions based on O:C and molar mass

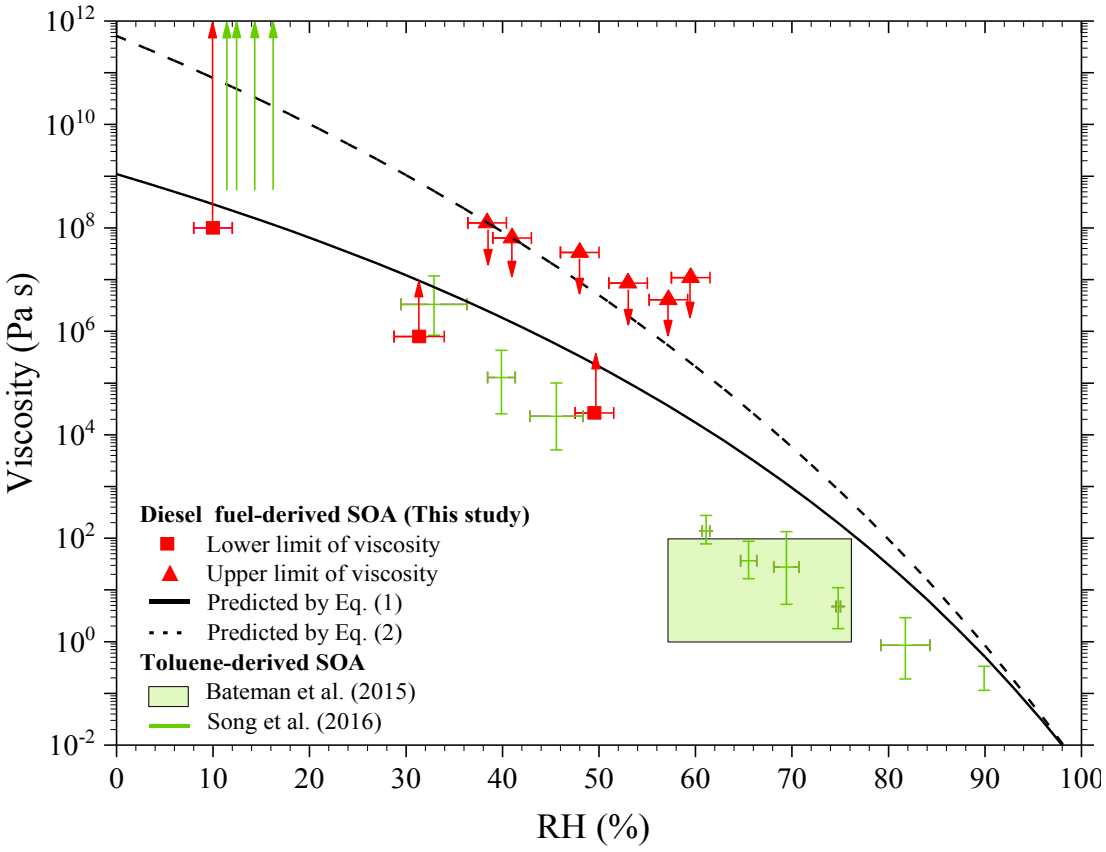

Figure 4.1. Viscosities of diesel fuel-derived SOA with the viscosities from individual poke-and-flow experiments grouped by RH. Each data point corresponds to a viscosity determined from a single poke-and-flow experiment. The lower limit to the viscosities and the upper limit to the viscosities represent the lowest and the highest viscosities in the group, respectively. At least two data points were included in each group. The *x* error bars represent the lowest and highest RH ranges in the group and the uncertainty in the RH measurements. Also included are viscosities of toluene SOA from Bateman et al. (2015) (green box) and Song et al. (2016) (green bar) and predicted viscosities of the diesel fuel SOA using Eq. (1) (black solid line) and Eq. (2) (black dashed line).[9, 10]

(Eq. 1) for dry conditions (i.e. 0 % RH) (Fig. 4.1). Eq. 2 was applied to molar masses up to ~1100 g mol^{-1} while Eq. 1 was applied to molar masses < 450 g mol^{-1}. If Eq. 2 was limited to molar mass < 450 g mol^{-1}, the predicted viscosities would only decrease by a factor of ≤ 1.3 (Fig. 4.2). The difference in the predictions based on Eq. 2 and Eq. 1 shown in Fig. 4.1 is due to the uncertainties in those two parameterizations. More comprehensive experimental T_g datasets are needed to further refine the T_g parameterizations. The predicted viscosities shown in Fig. 4.1 only consider CH and CHO compounds. For the diesel fuel SOA studied here, 257 compounds (~36% of the intensity weighted peaks) were CHON compounds.[85] A comprehensive

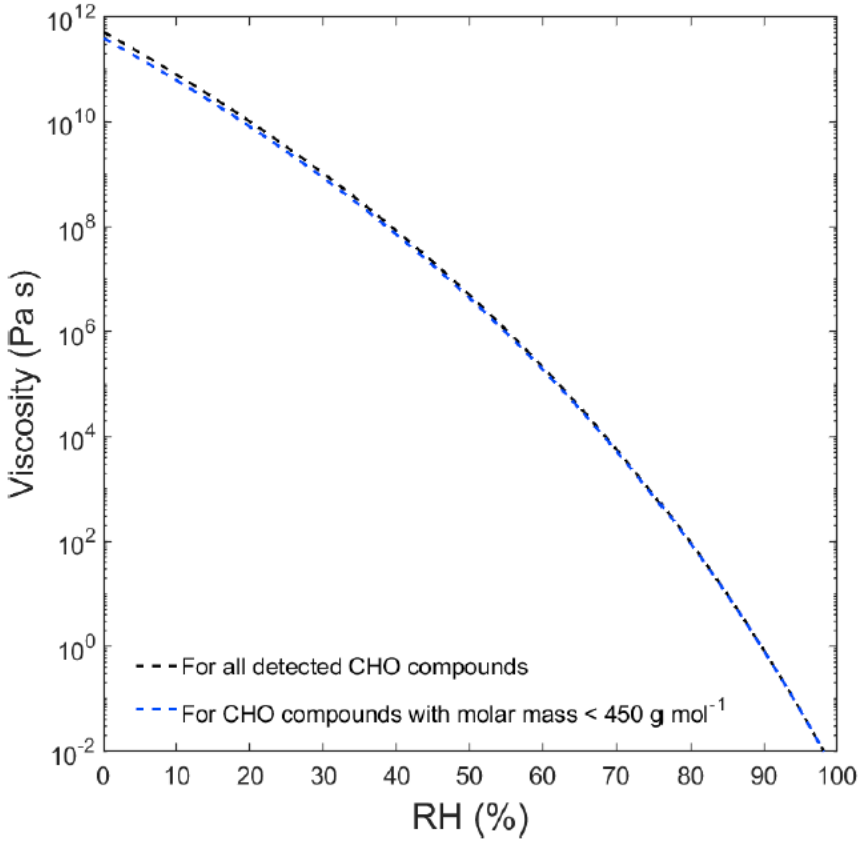

Figure 4.2: Predicted viscosities of the diesel-derived SOA using Eq. (2) for all the detected CHO compounds (black dashed line, same as that shown in Fig. 4.1), and CHO compounds with molar mass < 450 g mol^{-1} (blue dashed line).

experimental T_g dataset for organic compounds containing nitrogen atoms is required to improve the viscosity predictions of diesel fuel SOA.

4.4: Conclusion

The measured viscosities were consistent with predictions based on molar mass and O:C and predictions based on the number of carbon, hydrogen, and oxygen atoms of identified SOA compounds. Additional measurements of viscosity of diesel fuel SOA with reduced uncertainties would be useful to better test the predictions. Furthermore, additional comprehensive experimental T_g datasets are needed to further refine the parameterizations.

References

1. Shiraiwa, M.; Ammann, M.; Koop, T.; Pöschl, U., Gas uptake and chemical aging of semisolid organic aerosol particles. *Proceedings of the National Academy of Sciences* **2011,** *108* (27), 11003.
2. Hinks, M. L.; Montoya-Aguilera, J.; Ellison, L.; Lin, P.; Laskin, A.; Laskin, J.; Shiraiwa, M.; Dabdub, D.; Nizkorodov, S. A., Effect of relative humidity on the composition of secondary organic aerosol from the oxidation of toluene. *Atmos. Chem. Phys.* **2018,** *18* (3), 1643-1652.
3. Davidovits, P.; Kolb, C. E.; Williams, L. R.; Jayne, J. T.; Worsnop, D. R., Mass Accommodation and Chemical Reactions at Gas-Liquid Interfaces. *Chem. Rev. (Washington, DC, U. S.)* **2006,** *106* (4), 1323-1354.
4. Shiraiwa, M.; Pfrang, C.; Koop, T.; Poeschl, U., Kinetic multi-layer model of gas-particle interactions in aerosols and clouds (KM-GAP): linking condensation, evaporation and chemical reactions of organics, oxidants and water. *Atmos. Chem. Phys.* **2012,** *12* (5), 2777-2794.
5. Koop, T.; Bookhold, J.; Shiraiwa, M.; Poeschl, U., Glass transition and phase state of organic compounds: dependency on molecular properties and implications for secondary organic aerosols in the atmosphere. *Phys. Chem. Chem. Phys.* **2011,** *13* (43), 19238-19255.
6. Dette, H. P.; Qi, M.; Schröder, D. C.; Godt, A.; Koop, T., Glass-Forming Properties of 3-Methylbutane-1,2,3-tricarboxylic Acid and Its Mixtures with Water and Pinonic Acid. *The Journal of Physical Chemistry A* **2014,** *118* (34), 7024-7033.
7. Rothfuss, N. E.; Petters, M. D., Influence of Functional Groups on the Viscosity of Organic Aerosol. *Environ. Sci. Technol.* **2017,** *51* (1), 271-279.
8. Shiraiwa, M.; Berkemeier, T.; Schilling-Fahnestock, K. A.; Seinfeld, J. H.; Poeschl, U., Molecular corridors and kinetic regimes in the multiphase chemical evolution of secondary organic aerosol. *Atmos. Chem. Phys.* **2014,** *14* (16), 8323-8341.
9. Song, M.; Liu, P. F.; Hanna, S. J.; Zaveri, R. A.; Potter, K.; You, Y.; Martin, S. T.; Bertram, A. K., Relative humidity-dependent viscosity of secondary organic material from toluene photo-oxidation and possible implications for organic particulate matter over megacities. *Atmos. Chem. Phys.* **2016,** *16* (14), 8817-8830.
10. Bateman, A. P.; Bertram, A. K.; Martin, S. T., Hygroscopic Influence on the Semisolid-to-Liquid Transition of Secondary Organic Materials. *The Journal of Physical Chemistry A* **2015,** *119* (19), 4386-4395.
11. Li, Y. J.; Liu, P.; Gong, Z.; Wang, Y.; Bateman, A. P.; Bergoend, C.; Bertram, A. K.; Martin, S. T., Chemical Reactivity and Liquid/Nonliquid States of Secondary Organic Material. *Environmental Science & Technology* **2015,** *49* (22), 13264-13274.
12. Chu, Y.; Chan, C. K., Reactive Uptake of Dimethylamine by Ammonium Sulfate and Ammonium Sulfate-Sucrose Mixed Particles. *J. Phys. Chem. A* **2017,** *121* (1), 206-215.
13. Zuend, A.; Marcolli, C.; Booth, A. M.; Lienhard, D. M.; Soonsin, V.; Krieger, U. K.; Topping, D. O.; McFiggans, G.; Peter, T.; Seinfeld, J. H., New and extended parameterization of the thermodynamic model AIOMFAC: calculation of activity coefficients for organic-inorganic mixtures containing carboxyl, hydroxyl, carbonyl, ether, ester, alkenyl, alkyl, and aromatic functional groups. *Atmos. Chem. Phys.* **2011,** *11* (17), 9155-9206.
14. Mikhailov, E.; Vlasenko, S.; Martin, S. T.; Koop, T.; Poeschl, U., Amorphous and crystalline aerosol particles interacting with water vapor: conceptual framework and experimental evidence for restructuring, phase transitions and kinetic limitations. *Atmos. Chem. Phys.* **2009,** *9* (24), 9491-9522.
15. Akimoto, H., Global Air Quality and Pollution. *Science (Washington, DC, U. S.)* **2003,** *302* (5651), 1716-1719.
16. Wilson, S. R.; Madronich, S.; Longstreth, J. D.; Solomon, K. R., Interactive effects of changing stratospheric ozone and climate on tropospheric composition and air quality, and the consequences for human and ecosystem health. *Photochem. Photobiol. Sci.* **2019,** *18* (3), 775-803.

17. Gordon, H.; Sengupta, K.; Rap, A.; Duplissy, J.; Frege, C.; Williamson, C.; Heinritzi, M.; Simon, M.; Yan, C.; Almeida, J.; Tröstl, J.; Nieminen, T.; Ortega, I. K.; Wagner, R.; Dunne, E. M.; Adamov, A.; Amorim, A.; Bernhammer, A.-K.; Bianchi, F.; Breitenlechner, M.; Brilke, S.; Chen, X.; Craven, J. S.; Dias, A.; Ehrhart, S.; Fischer, L.; Flagan, R. C.; Franchin, A.; Fuchs, C.; Guida, R.; Hakala, J.; Hoyle, C. R.; Jokinen, T.; Junninen, H.; Kangasluoma, J.; Kim, J.; Kirkby, J.; Krapf, M.; Kürten, A.; Laaksonen, A.; Lehtipalo, K.; Makhmutov, V.; Mathot, S.; Molteni, U.; Monks, S. A.; Onnela, A.; Peräkylä, O.; Piel, F.; Petäjä, T.; Praplan, A. P.; Pringle, K. J.; Richards, N. A. D.; Rissanen, M. P.; Rondo, L.; Sarnela, N.; Schobesberger, S.; Scott, C. E.; Seinfeld, J. H.; Sharma, S.; Sipilä, M.; Steiner, G.; Stozhkov, Y.; Stratmann, F.; Tomé, A.; Virtanen, A.; Vogel, A. L.; Wagner, A. C.; Wagner, P. E.; Weingartner, E.; Wimmer, D.; Winkler, P. M.; Ye, P.; Zhang, X.; Hansel, A.; Dommen, J.; Donahue, N. M.; Worsnop, D. R.; Baltensperger, U.; Kulmala, M.; Curtius, J.; Carslaw, K. S., Reduced anthropogenic aerosol radiative forcing caused by biogenic new particle formation. *Proceedings of the National Academy of Sciences* **2016,** *113* (43), 12053.
18. Bellouin, N.; Boucher, O.; Haywood, J.; Reddy, M. S., Global estimate of aerosol direct radiative forcing from satellite measurements. *Nature* **2005,** *438* (7071), 1138-1141.
19. Finlayson-Pitts, B. J., Introductory lecture: atmospheric chemistry in the Anthropocene. *Faraday Discuss.* **2017,** *200* (Atomospheric Chemistry in the Anthropocene), 11-58.
20. Freedman, M. A., Phase separation in organic aerosol. *Chem. Soc. Rev.* **2017,** *46* (24), 7694-7705.
21. McMurry, P. H., A review of atmospheric aerosol measurements. *Atmos. Environ.* **2000,** *34* (12-14), 1959-1999.
22. Bzdek, B. R.; Reid, J. P., Perspective: Aerosol microphysics: From molecules to the chemical physics of aerosols. *J. Chem. Phys.* **2017,** *147* (22), 220901/1-220901/17.
23. Shiraiwa, M.; Ueda, K.; Pozzer, A.; Lammel, G.; Kampf, C. J.; Fushimi, A.; Enami, S.; Arangio, A. M.; Fröhlich-Nowoisky, J.; Fujitani, Y.; Furuyama, A.; Lakey, P. S. J.; Lelieveld, J.; Lucas, K.; Morino, Y.; Pöschl, U.; Takahama, S.; Takami, A.; Tong, H.; Weber, B.; Yoshino, A.; Sato, K., Aerosol Health Effects from Molecular to Global Scales. *Environmental Science & Technology* **2017,** *51* (23), 13545-13567.
24. Reinmuth-Selzle, K.; Kampf, C. J.; Lucas, K.; Lang-Yona, N.; Fröhlich-Nowoisky, J.; Shiraiwa, M.; Lakey, P. S. J.; Lai, S.; Liu, F.; Kunert, A. T.; Ziegler, K.; Shen, F.; Sgarbanti, R.; Weber, B.; Bellinghausen, I.; Saloga, J.; Weller, M. G.; Duschl, A.; Schuppan, D.; Pöschl, U., Air Pollution and Climate Change Effects on Allergies in the Anthropocene: Abundance, Interaction, and Modification of Allergens and Adjuvants. *Environmental Science & Technology* **2017,** *51* (8), 4119-4141.
25. Cao, C.; Lee, X.; Liu, S.; Schultz, N.; Xiao, W.; Zhang, M.; Zhao, L., Urban heat islands in China enhanced by haze pollution. *Nature Communications* **2016,** *7*, 12509.
26. Guo, S.; Hu, M.; Zamora, M. L.; Peng, J.; Shang, D.; Zheng, J.; Du, Z.; Wu, Z.; Shao, M.; Zeng, L.; Molina, M. J.; Zhang, R., Elucidating severe urban haze formation in China. *Proceedings of the National Academy of Sciences* **2014,** *111* (49), 17373.
27. Pilinis, C., Pandis, Spyros N., Seinfeld, John H., Sensitivity of direct climate forcing by atmospheric aerosols to aerosol size and composition. *Journal of Geophysical Research: Atmospheres* **1995,** *100* (D9), 18739-18754.
28. Lin, P.; Aiona, P. K.; Li, Y.; Shiraiwa, M.; Laskin, J.; Nizkorodov, S. A.; Laskin, A., Molecular Characterization of Brown Carbon in Biomass Burning Aerosol Particles. *Environ. Sci. Technol.* **2016,** *50* (21), 11815-11824.
29. Laskin, A.; Laskin, J.; Nizkorodov, S. A., Chemistry of Atmospheric Brown Carbon. *Chemical Reviews* **2015,** *115* (10), 4335-4382.
30. Andreae, M. O.; Gelencsér, A., Black carbon or brown carbon? The nature of light-absorbing carbonaceous aerosols. *Atmos. Chem. Phys.* **2006,** *6* (10), 3131-3148.
31. Charnawskas, J. C.; Alpert, P. A.; Lambe, A.; Berkemeier, T.; O'Brien, R. E.; Massoli, P.; Onasch, T. B.; Shiraiwa, M.; Moffet, R. C.; Gilles, M. K.; Davidovits, P.; Worsnop, D.; Knopf, D. A., Condensed-phase biogenic-anthropogenic interactions with implications for cold cloud formation. *Faraday Discuss.* **2017**, *200*, 165-194.

32. Berkemeier, T.; Shiraiwa, M.; Poeschl, U.; Koop, T., Competition between water uptake and ice nucleation by glassy organic aerosol particles. *Atmos. Chem. Phys.* **2014,** *14* (22), 12513-12531.
33. Liu, P.; Zhao, T.; Gunthe, S. S.; He, Y.; Qin, Y. M.; Gong, Z.; Amorim, J. C.; Martin, S. T.; Song, M.; Bertram, A. K.; Song, M.; Ham, S.; Gunthe, S. S.; He, Y.; Martin, S. T., Resolving the mechanisms of hygroscopic growth and cloud condensation nuclei activity for organic particulate matter. *Nat Commun* **2018,** *9* (1), 4076.
34. Shiraiwa, M.; Shiraiwa, M.; Li, Y.; Berkemeier, T.; Poschl, U.; Li, Y.; Li, Y.; Tsimpidi, A. P.; Karydis, V. A.; Lelieveld, J.; Berkemeier, T.; Pandis, S. N.; Lelieveld, J.; Koop, T., Global distribution of particle phase state in atmospheric secondary organic aerosols. *Nat Commun* **2017,** *8*, 15002.
35. Jimenez, J. L.; Canagaratna, M. R.; Donahue, N. M.; Prevot, A. S. H.; Zhang, Q.; Kroll, J. H.; DeCarlo, P. F.; Allan, J. D.; Coe, H.; Ng, N. L.; Aiken, A. C.; Docherty, K. S.; Ulbrich, I. M.; Grieshop, A. P.; Robinson, A. L.; Duplissy, J.; Smith, J. D.; Wilson, K. R.; Lanz, V. A.; Hueglin, C.; Sun, Y. L.; Tian, J.; Laaksonen, A.; Raatikainen, T.; Rautiainen, J.; Vaattovaara, P.; Ehn, M.; Kulmala, M.; Tomlinson, J. M.; Collins, D. R.; Cubison, M. J.; Dunlea, J.; Huffman, J. A.; Onasch, T. B.; Alfarra, M. R.; Williams, P. I.; Bower, K.; Kondo, Y.; Schneider, J.; Drewnick, F.; Borrmann, S.; Weimer, S.; Demerjian, K.; Salcedo, D.; Cottrell, L.; Griffin, R.; Takami, A.; Miyoshi, T.; Hatakeyama, S.; Shimono, A.; Sun, J. Y.; Zhang, Y. M.; Dzepina, K.; Kimmel, J. R.; Sueper, D.; Jayne, J. T.; Herndon, S. C.; Trimborn, A. M.; Williams, L. R.; Wood, E. C.; Middlebrook, A. M.; Kolb, C. E.; Baltensperger, U.; Worsnop, D. R., Evolution of Organic Aerosols in the Atmosphere. *Science (Washington, DC, U. S.)* **2009,** *326* (5959), 1525-1529.
36. Reid, J. P.; Bertram, A. K.; Topping, D. O.; Laskin, A.; Martin, S. T.; Petters, M. D.; Pope, F. D.; Rovelli, G., The viscosity of atmospherically relevant organic particles. *Nature Communications* **2018,** *9* (1), 956.
37. Zobrist, B.; Marcolli, C.; Pedernera, D. A.; Koop, T., Do atmospheric aerosols form glasses? *Atmos. Chem. Phys.* **2008,** *8* (17), 5221-5244.
38. Renbaum-Wolff, L.; Grayson, J. W.; Bateman, A. P.; Kuwata, M.; Sellier, M.; Murray, B. J.; Shilling, J. E.; Martin, S. T.; Bertram, A. K., Viscosity of α-pinene secondary organic material and implications for particle growth and reactivity. *Proceedings of the National Academy of Sciences* **2013,** *110* (20), 8014-8019.
39. Song, M.; Liu, P. F.; Hanna, S. J.; Li, Y. J.; Martin, S. T.; Bertram, A. K., Relative humidity-dependent viscosities of isoprene-derived secondary organic material and atmospheric implications for isoprene-dominant forests. *Atmos. Chem. Phys.* **2015,** *15* (9), 5145-5159.
40. Zhang, Y.; Sanchez, M. S.; Douet, C.; Wang, Y.; Bateman, A. P.; Gong, Z.; Kuwata, M.; Renbaum-Wolff, L.; Sato, B. B.; Liu, P. F.; Bertram, A. K.; Geiger, F. M.; Martin, S. T., Changing shapes and implied viscosities of suspended submicron particles. *Atmos. Chem. Phys.* **2015,** *15* (14), 7819-7829.
41. Grayson, J. W.; Zhang, Y.; Mutzel, A.; Renbaum-Wolff, L.; Böge, O.; Kamal, S.; Herrmann, H.; Martin, S. T.; Bertram, A. K., Effect of varying experimental conditions on the viscosity of α-pinene derived secondary organic material. *Atmos. Chem. Phys.* **2016,** *16* (10), 6027-6040.
42. Shiraiwa, M.; Seinfeld, J. H., Equilibration timescale of atmospheric secondary organic aerosol partitioning. *Geophys. Res. Lett.* **2012,** *39* (Dec.), L24801.
43. Donahue, N. M.; Robinson, A. L.; Stanier, C. O.; Pandis, S. N., Coupled Partitioning, Dilution, and Chemical Aging of Semivolatile Organics. *Environ. Sci. Technol.* **2006,** *40* (8), 2635-2643.
44. Tsigaridis, K.; Daskalakis, N.; Kanakidou, M.; Adams, P. J.; Artaxo, P.; Bahadur, R.; Balkanski, Y.; Bauer, S. E.; Bellouin, N.; Benedetti, A.; Bergman, T.; Berntsen, T. K.; Beukes, J. P.; Bian, H.; Carslaw, K. S.; Chin, M.; Curci, G.; Diehl, T.; Easter, R. C.; Ghan, S. J.; Gong, S. L.; Hodzic, A.; Hoyle, C. R.; Iversen, T.; Jathar, S.; Jimenez, J. L.; Kaiser, J. W.; Kirkevag, A.; Koch, D.; Kokkola, H.; Lee, Y. H.; Lin, G.; Liu, X.; Luo, G.; Ma, X.; Mann, G. W.; Mihalopoulos, N.; Morcrette, J. J.; Muller, J. F.; Myhre, G.; Myriokefalitakis, S.; Ng, N. L.; O'Donnell, D.; Penner, J. E.; Pozzoli, L.; Pringle, K. J.; Russell, L. M.; Schulz, M.; Sciare, J.; Seland, O.; Shindell, D. T.; Sillman,

S.; Skeie, R. B.; Spracklen, D.; Stavrakou, T.; Steenrod, S. D.; Takemura, T.; Tiitta, P.; Tilmes, S.; Tost, H.; van Noije, T.; van Zyl, P. G.; von Salzen, K.; Yu, F.; Wang, Z.; Zaveri, R. A.; Zhang, H.; Zhang, K.; Zhang, Q.; Zhang, X., The AeroCom evaluation and intercomparison of organic aerosol in global models. *Atmos. Chem. Phys.* **2014,** *14* (19), 10845-10895.
45. Pöschl, U.; Shiraiwa, M., Multiphase Chemistry at the Atmosphere–Biosphere Interface Influencing Climate and Public Health in the Anthropocene. *Chemical Reviews* **2015,** *115* (10), 4440-4475.
46. Dette, H. P.; Koop, T., Glass Formation Processes in Mixed Inorganic/Organic Aerosol Particles. *J. Phys. Chem. A* **2015,** *119* (19), 4552-4561.
47. Angell, C. A., Formation of glasses from liquids and biopolymers. *Science (Washington, D. C.)* **1995,** *267* (5206), 1924-35.
48. Angell, C. A., Relaxation in liquids, polymers and plastic crystals - strong/fragile patterns and problems. *J. Non-Cryst. Solids* **1991,** *131-133* (Pt. 1), 13-31.
49. Boehmer, R.; Ngai, K. L.; Angell, C. A.; Plazek, D. J., Nonexponential relaxations in strong and fragile glass formers. *J. Chem. Phys.* **1993,** *99* (5), 4201-9.
50. Angell, C. A., Entropy and fragility in supercooling liquids. *J. Res. Natl. Inst. Stand. Technol.* **1997,** *102* (2), 171-185.
51. Angell, C. A.; Bressel, R. D.; Green, J. L.; Kanno, H.; Oguni, M.; Sare, E. J., Liquid Fragility and the Glass Transition in Water and Aqueous Solutions. In *Water in Foods*, Fito, P.; Mulet, A.; McKenna, B., Eds. Pergamon: Amsterdam, 1994; pp 115-142.
52. Song, M.; Maclean, A. M.; Huang, Y.; Smith, N. R.; Blair, S. L.; Laskin, J.; Laskin, A.; DeRieux, W. S. W.; Li, Y.; Shiraiwa, M.; Nizkorodov, S. A.; Bertram, A. K., Liquid-liquid phase separation and viscosity within secondary organic aerosol generated from diesel fuel vapors. *Atmos. Chem. Phys. Discuss.* **2019,** *2019*, 1-37.
53. Song, M.; Ham, S.; Andrews, R. J.; You, Y.; Bertram, A. K., Liquid-liquid phase separation in organic particles containing one and two organic species: importance of the average O : C. *Atmos. Chem. Phys.* **2018,** *18* (16), 12075-12084.
54. Kalume, A.; Wang, C.; Santarpia, J.; Pan, Y.-L., Liquid-liquid phase separation and evaporation of a laser-trapped organic-organic airborne droplet using temporal spatial-resolved Raman spectroscopy. *Phys. Chem. Chem. Phys.* **2018,** *20* (28), 19151-19159.
55. Wu, F.-M.; Wang, X.-W.; Jing, B.; Zhang, Y.-H.; Ge, M.-F., Liquid-liquid phase separation in internally mixed magnesium sulfate/glutaric acid particles. *Atmos. Environ.* **2018,** *178*, 286-292.
56. Gorkowski, K.; Donahue, N. M.; Sullivan, R. C., Emulsified and Liquid-Liquid Phase-Separated States of α-Pinene Secondary Organic Aerosol Determined Using Aerosol Optical Tweezers. *Environ. Sci. Technol.* **2017,** *51* (21), 12154-12163.
57. Drozd, G. T.; Woo, J. L.; McNeill, V. F., Self-limited uptake of α-pinene oxide to acidic aerosol: the effects of liquid-liquid phase separation and implications for the formation of secondary organic aerosol and organosulfates from epoxides. *Atmos. Chem. Phys.* **2013,** *13* (16), 8255-8263.
58. Zhang, Y.; Chen, Y.; Lambe, A. T.; Olson, N. E.; Lei, Z.; Craig, R. L.; Zhang, Z.; Gold, A.; Onasch, T. B.; Jayne, J. T.; Worsnop, D. R.; Gaston, C. J.; Thornton, J. A.; Vizuete, W.; Ault, A. P.; Surratt, J. D., Effect of the Aerosol-Phase State on Secondary Organic Aerosol Formation from the Reactive Uptake of Isoprene-Derived Epoxydiols (IEPOX). *Environ. Sci. Technol. Lett.* **2018,** *5* (3), 167-174.
59. Shiraiwa, M.; Zuend, A.; Bertram, A. K.; Seinfeld, J. H., Gas-particle partitioning of atmospheric aerosols: interplay of physical state, non-ideal mixing and morphology. *Phys. Chem. Chem. Phys.* **2013,** *15* (27), 11441-11453.
60. Zaveri, R. A.; Shilling, J. E.; Zelenyuk, A.; Liu, J.; Bell, D. M.; D'Ambro, E. L.; Gaston, C. J.; Thornton, J. A.; Laskin, A.; Lin, P.; Wilson, J.; Easter, R. C.; Wang, J.; Bertram, A. K.; Martin, S. T.; Seinfeld, J. H.; Worsnop, D. R., Growth Kinetics and Size Distribution Dynamics of Viscous Secondary Organic Aerosol. *Environ. Sci. Technol.* **2018,** *52* (3), 1191-1199.

61. DeRieux, W.-S. W.; Li, Y.; Lin, P.; Laskin, J.; Laskin, A.; Bertram, A. K.; Nizkorodov, S. A.; Shiraiwa, M., Predicting the glass transition temperature and viscosity of secondary organic material using molecular composition. *Atmos. Chem. Phys.* **2018,** *18* (9), 6331-6351.
62. Shrivastava, M.; Cappa, C. D.; Fan, J.; Goldstein, A. H.; Guenther, A. B.; Jimenez, J. L.; Kuang, C.; Laskin, A.; Martin, S. T.; Ng, N. L.; Petaja, T.; Pierce, J. R.; Rasch, P. J.; Roldin, P.; Seinfeld, J. H.; Shilling, J.; Smith, J. N.; Thornton, J. A.; Volkamer, R.; Wang, J.; Worsnop, D. R.; Zaveri, R. A.; Zelenyuk, A.; Zhang, Q., Recent advances in understanding secondary organic aerosol: Implications for global climate forcing. *Reviews of Geophysics* **2017,** *55* (2), 509-559.
63. Randall, D.; Khairoutdinov, M.; Arakawa, A.; Grabowski, W., Breaking the Cloud Parameterization Deadlock. *Bulletin of the American Meteorological Society* **2003,** *84* (11), 1547-1564.
64. Li, Y.; Poeschl, U.; Shiraiwa, M., Molecular corridors and parameterizations of volatility in the chemical evolution of organic aerosols. *Atmos. Chem. Phys.* **2016,** *16* (5), 3327-3344.
65. The Concept of Model. In *Modeling of Atmospheric Chemistry*, Jacob, D. J.; Brasseur, G. P., Eds. Cambridge University Press: Cambridge, 2017; pp 1-20.
66. Arangio, A. M.; Slade, J. H.; Berkemeier, T.; Poeschl, U.; Knopf, D. A.; Shiraiwa, M., Multiphase Chemical Kinetics of OH Radical Uptake by Molecular Organic Markers of Biomass Burning Aerosols: Humidity and Temperature Dependence, Surface Reaction, and Bulk Diffusion. *J. Phys. Chem. A* **2015,** *119* (19), 4533-4544.
67. Chemical Processes in the Atmosphere. In *Modeling of Atmospheric Chemistry*, Jacob, D. J.; Brasseur, G. P., Eds. Cambridge University Press: Cambridge, 2017; pp 54-83.
68. Berkemeier, T.; Ammann, M.; Mentel, T. F.; Pöschl, U.; Shiraiwa, M., Organic Nitrate Contribution to New Particle Formation and Growth in Secondary Organic Aerosols from α-Pinene Ozonolysis. *Environmental Science & Technology* **2016,** *50* (12), 6334-6342.
69. Numerical Methods for Chemical Systems. In *Modeling of Atmospheric Chemistry*, Jacob, D. J.; Brasseur, G. P., Eds. Cambridge University Press: Cambridge, 2017; pp 253-274.
70. Danckwerts, P. V., Absorption by simultaneous diffusion and chemical reaction into particles of various shapes and into falling drops. *Trans. Faraday Soc.* **1951,** *47*, 1014-23.
71. Steimer, S. S.; Berkemeier, T.; Gilgen, A.; Krieger, U. K.; Peter, T.; Shiraiwa, M.; Ammann, M., Shikimic acid ozonolysis kinetics of the transition from liquid aqueous solution to highly viscous glass. *Phys. Chem. Chem. Phys.* **2015,** *17* (46), 31101-31109.
72. Xiao, S.; Bertram, A. K., Reactive uptake kinetics of NO3 on multicomponent and multiphase organic mixtures containing unsaturated and saturated organics. *Phys. Chem. Chem. Phys.* **2011,** *13* (14), 6628-6636.
73. Shiraiwa, M.; Garland, R. M.; Poeschl, U., Kinetic double-layer model of aerosol surface chemistry and gas-particle interactions (K2-SURF): degradation of polycyclic aromatic hydrocarbons exposed to O3, NO2, H2O, OH and NO3. *Atmos. Chem. Phys.* **2009,** *9* (24), 9571-9586.
74. Shiraiwa, M.; Pfrang, C.; Poeschl, U., Kinetic multi-layer model of aerosol surface and bulk chemistry (KM-SUB): the influence of interfacial transport and bulk diffusion on the oxidation of oleic acid by ozone. *Atmos. Chem. Phys.* **2010,** *10* (8), 3673-3691.
75. Poeschl, U.; Rudich, Y.; Ammann, M., Kinetic model framework for aerosol and cloud surface chemistry and gas-particle interactions - part 1: general equations, parameters, and terminology. *Atmos. Chem. Phys.* **2007,** *7* (23), 5989-6023.
76. Smith, J. N.; Barsanti, K. C.; Friedli, H. R.; Ehn, M.; Kulmala, M.; Collins, D. R.; Scheckman, J. H.; Williams, B. J.; McMurry, P. H., Observations of aminium salts in atmospheric nanoparticles and possible climatic implications. *Proc. Natl. Acad. Sci. U. S. A.* **2010,** *107* (15), 6634-6639.
77. Krieger, U. K.; Marcolli, C.; Reid, J. P., Exploring the complexity of aerosol particle properties and processes using single particle techniques. *Chem. Soc. Rev.* **2012,** *41* (19), 6631-6662.
78. Smith, J. N.; Moore, K. F.; McMurry, P. H.; Eisele, F. L., Atmospheric measurements of sub-20 nm diameter particle chemical composition by thermal desorption chemical ionization mass spectrometry. *Aerosol Sci. Technol.* **2004,** *38* (2), 100-110.

79. Ge, X.; Wexler, A. S.; Clegg, S. L., Atmospheric amines - Part I. A review. *Atmos. Environ.* **2011,** *45* (3), 524-546.
80. MÄKelÄ, J. M.; Yli-Koivisto, S.; Hiltunen, V.; Seidl, W.; Swietlicki, E.; TeinilÄ, K.; SillanpÄÄ, M.; Koponen, I. K.; Paatero, J.; Rosman, K.; HÄMeri, K., Chemical composition of aerosol during particle formation events in boreal forest. *Tellus B* **2001,** *53* (4), 380-393.
81. Chan, L. P.; Chan, C. K., Displacement of Ammonium from Aerosol Particles by Uptake of Triethylamine. *Aerosol Sci. Technol.* **2012,** *46* (2), 236-247.
82. Zordan, C. A.; Wang, S.; Johnston, M. V., Time-Resolved Chemical Composition of Individual Nanoparticles in Urban Air. *Environmental Science & Technology* **2008,** *42* (17), 6631-6636.
83. Bzdek, B. R.; Ridge, D. P.; Johnston, M. V., Amine exchange into ammonium bisulfate and ammonium nitrate nuclei. *Atmos. Chem. Phys.* **2010,** *10* (8), 3495-3503.
84. Liu, Y.; Han, C.; Liu, C.; Ma, J.; Ma, Q.; He, H., Differences in the reactivity of ammonium salts with methylamine. *Atmos. Chem. Phys.* **2012,** *12* (11), 4855-4865.
85. Blair, S. L.; MacMillan, A. C.; Drozd, G. T.; Goldstein, A. H.; Chu, R. K.; Paša-Tolić, L.; Shaw, J. B.; Tolić, N.; Lin, P.; Laskin, J.; Laskin, A.; Nizkorodov, S. A., Molecular Characterization of Organosulfur Compounds in Biodiesel and Diesel Fuel Secondary Organic Aerosol. *Environmental Science & Technology* **2017,** *51* (1), 119-127.
86. Goldstein, A. H.; Galbally, I. E., Known and Unexplored Organic Constituents in the Earth's Atmosphere. *Environmental Science & Technology* **2007,** *41* (5), 1514-1521.
87. Huang, W.; Saathoff, H.; Pajunoja, A.; Shen, X.; Naumann, K. H.; Wagner, R.; Virtanen, A.; Leisner, T.; Mohr, C., α-Pinene secondary organic aerosol at low temperature: chemical composition and implications for particle viscosity. *Atmos. Chem. Phys.* **2018,** *18* (4), 2883-2898.
88. Virtanen, A.; Joutsensaari, J.; Koop, T.; Kannosto, J.; Yli-Pirilae, P.; Leskinen, J.; Maekelae, J. M.; Holopainen, J. K.; Poeschl, U.; Kulmala, M.; Worsnop, D. R.; Laaksonen, A., An amorphous solid state of biogenic secondary organic aerosol particles. *Nature (London, U. K.)* **2010,** *467* (7317), 824-827.
89. Saukko, E.; Lambe, A. T.; Massoli, P.; Koop, T.; Wright, J. P.; Croasdale, D. R.; Pedernera, D. A.; Onasch, T. B.; Laaksonen, A.; Davidovits, P.; Worsnop, D. R.; Virtanen, A., Humidity-dependent phase state of SOA particles from biogenic and anthropogenic precursors. *Atmos. Chem. Phys.* **2012,** *12* (16), 7517-7529.
90. Jain, S.; Petrucci, G. A., A New Method to Measure Aerosol Particle Bounce Using a Cascade Electrical Low Pressure Impactor. *Aerosol Science and Technology* **2015,** *49* (6), 390-399.
91. Bateman, A. P.; Gong, Z.; Liu, P.; Sato, B.; Cirino, G.; Zhang, Y.; Artaxo, P.; Bertram, A. K.; Manzi, A. O.; Rizzo, L. V.; Souza, R. A. F.; Zaveri, R. A.; Martin, S. T., Sub-micrometre particulate matter is primarily in liquid form over Amazon rainforest. *Nature Geoscience* **2015,** *9*, 34.
92. Cappa, C. D.; Wilson, K. R., Evolution of organic aerosol mass spectra upon heating: implications for OA phase and partitioning behavior. *Atmos. Chem. Phys.* **2011,** *11* (5), 1895-1911.
93. Vaden, T. D.; Imre, D.; Beránek, J.; Shrivastava, M.; Zelenyuk, A., Evaporation kinetics and phase of laboratory and ambient secondary organic aerosol. *Proceedings of the National Academy of Sciences* **2011,** *108* (6), 2190.
94. Yli-Juuti, T.; Pajunoja, A.; Tikkanen, O.-P.; Buchholz, A.; Faiola, C.; Väisänen, O.; Hao, L.; Kari, E.; Peräkylä, O.; Garmash, O.; Shiraiwa, M.; Ehn, M.; Lehtinen, K.; Virtanen, A., Factors controlling the evaporation of secondary organic aerosol from α-pinene ozonolysis. *Geophysical Research Letters* **2017,** *44* (5), 2562-2570.
95. Roldin, P.; Eriksson, A. C.; Nordin, E. Z.; Hermansson, E.; Mogensen, D.; Rusanen, A.; Boy, M.; Swietlicki, E.; Svenningsson, B.; Zelenyuk, A.; Pagels, J., Modelling non-equilibrium secondary organic aerosol formation and evaporation with the aerosol dynamics, gas- and particle-phase chemistry kinetic multilayer model ADCHAM. *Atmos. Chem. Phys.* **2014,** *14* (15), 7953-7993.
96. Hosny, N. A.; Fitzgerald, C.; Vysniauskas, A.; Athanasiadis, A.; Berkemeier, T.; Uygur, N.; Poschl, U.; Shiraiwa, M.; Kalberer, M.; Pope, F. D.; Kuimova, M. K., Direct imaging of changes in aerosol particle viscosity upon hydration and chemical aging. *Chem. Sci.* **2016,** *7* (2), 1357-1367.

97. Hinks, M. L.; Brady, M. V.; Lignell, H.; Song, M.; Grayson, J. W.; Bertram, A. K.; Lin, P.; Laskin, A.; Laskin, J.; Nizkorodov, S. A., Effect of viscosity on photodegradation rates in complex secondary organic aerosol materials. *Physical Chemistry Chemical Physics* **2016,** *18* (13), 8785-8793.
98. Einstein, A., The motion of elements suspended in static liquids as claimed in the molecular kinetic theory of heat. *Ann der Phys* **1905,** *17*, 549-560.
99. Atkins, P. W., *Physical Chemistry*. Oxford Unversity Press: Oxford, 1998.
100. Seinfeld, J. H. P., S. N., *Atmospheric chemistry and physics - From air pollution to climate change*. John Wiley & Sons, Inc.: New York, 2006.
101. Schmelzer, J. W. P. G., I. S., *Glasses and the Glass Transition*. Wiley-VCH: Weinheim, Germany, 2011.
102. Price, H. C.; Mattsson, J.; Murray, B. J., Sucrose diffusion in aqueous solution. *Physical Chemistry Chemical Physics* **2016,** *18* (28), 19207-19216.
103. Chenyakin, Y.; Ullmann, D. A.; Evoy, E.; Renbaum-Wolff, L.; Kamal, S.; Bertram, A. K., Diffusion coefficients of organic molecules in sucrose–water solutions and comparison with Stokes–Einstein predictions. *Atmos. Chem. Phys.* **2017,** *17* (3), 2423-2435.
104. Marshall, F. H.; Miles, R. E. H.; Song, Y.-C.; Ohm, P. B.; Power, R. M.; Reid, J. P.; Dutcher, C. S., Diffusion and reactivity in ultraviscous aerosol and the correlation with particle viscosity. *Chemical Science* **2016,** *7* (2), 1298-1308.
105. Power, R. M.; Simpson, S. H.; Reid, J. P.; Hudson, A. J., The transition from liquid to solid-like behaviour in ultrahigh viscosity aerosol particles. *Chemical Science* **2013,** *4* (6), 2597-2604.
106. Champion, D.; Le Meste, M.; Simatos, D., Towards an improved understanding of glass transition and relaxations in foods: molecular mobility in the glass transition range. *Trends in Food Science & Technology* **2000,** *11* (2), 41-55.
107. Bastelberger, S.; Krieger, U. K.; Luo, B.; Peter, T., Diffusivity measurements of volatile organics in levitated viscous aerosol particles. *Atmos. Chem. Phys.* **2017,** *17* (13), 8453-8471.
108. Slade, J. H.; Knopf, D. A., Multiphase OH oxidation kinetics of organic aerosol: The role of particle phase state and relative humidity. *Geophysical Research Letters* **2014,** *41* (14), 5297-5306.
109. Abbatt, J. P. D.; Lee, A. K. Y.; Thornton, J. A., Quantifying trace gas uptake to tropospheric aerosol: recent advances and remaining challenges. *Chemical Society Reviews* **2012,** *41* (19), 6555-6581.
110. Davies, J. F.; Wilson, K. R., Nanoscale interfacial gradients formed by the reactive uptake of OH radicals onto viscous aerosol surfaces. *Chemical Science* **2015,** *6* (12), 7020-7027.
111. Kuwata, M.; Martin, S. T., Phase of atmospheric secondary organic material affects its reactivity. *Proceedings of the National Academy of Sciences* **2012,** *109* (43), 17354.
112. Zhou, S.; Shiraiwa, M.; McWhinney, R. D.; Poeschl, U.; Abbatt, J. P. D., Kinetic limitations in gas-particle reactions arising from slow diffusion in secondary organic aerosol. *Faraday Discuss.* **2013,** *165*, 391-406.
113. Berkemeier, T.; Steimer, S. S.; Krieger, U. K.; Peter, T.; Poeschl, U.; Ammann, M.; Shiraiwa, M., Ozone uptake on glassy, semi-solid and liquid organic matter and the role of reactive oxygen intermediates in atmospheric aerosol chemistry. *Phys. Chem. Chem. Phys.* **2016,** *18* (18), 12662-12674.
114. Wang, B.; O'Brien, R. E.; Kelly, S. T.; Shilling, J. E.; Moffet, R. C.; Gilles, M. K.; Laskin, A., Reactivity of liquid and semisolid secondary organic carbon with chloride and nitrate in atmospheric aerosols. *J. Phys. Chem. A* **2015,** *119* (19), 4498-4508.
115. Pratap, V.; Chen, Y.; Yao, G.; Nakao, S., Temperature effects on multiphase reactions of organic molecular markers: A modeling study. *Atmospheric Environment* **2018,** *179*, 40-48.
116. Liu, P.; Li, Y. J.; Wang, Y.; Bateman, A. P.; Zhang, Y.; Gong, Z.; Bertram, A. K.; Martin, S. T., Highly Viscous States Affect the Browning of Atmospheric Organic Particulate Matter. *ACS Central Science* **2018,** *4* (2), 207-215.
117. Mu, Q.; Shiraiwa, M.; Octaviani, M.; Ma, N.; Ding, A.; Su, H.; Lammel, G.; Pöschl, U.; Cheng, Y., Temperature effect on phase state and reactivity controls atmospheric multiphase chemistry and transport of PAHs. *Science Advances* **2018,** *4* (3), eaap7314.

118. Lignell, H.; Hinks, M. L.; Nizkorodov, S. A., Exploring matrix effects on photochemistry of organic aerosols. *Proceedings of the National Academy of Sciences* **2014,** *111* (38), 13780.
119. Bones, D. L.; Reid, J. P.; Lienhard, D. M.; Krieger, U. K., Comparing the mechanism of water condensation and evaporation in glassy aerosol. *Proceedings of the National Academy of Sciences* **2012,** *109* (29), 11613.
120. Price, H. C. M., B. J.; Mattsson, J.; O'Sullivan, D.; Wilson, T. W.; Baustian, K. J.; Benning, L. G., Quantifying water diffusion in high-viscosity and glassy aqueous solutions using a Raman isotope tracer method. *Atmos. Chem. Phys.* **2014,** *14*, 3817-3830.
121. Zobrist, B.; Soonsin, V.; Luo, B. P.; Krieger, U. K.; Marcolli, C.; Peter, T.; Koop, T., Ultra-slow water diffusion in aqueous sucrose glasses. *Phys. Chem. Chem. Phys.* **2011,** *13* (8), 3514-3526.
122. Murray, B. J.; Wilson, T. W.; Dobbie, S.; Cui, Z.; Al-Jumur, S. M. R. K.; Möhler, O.; Schnaiter, M.; Wagner, R.; Benz, S.; Niemand, M.; Saathoff, H.; Ebert, V.; Wagner, S.; Kärcher, B., Heterogeneous nucleation of ice particles on glassy aerosols under cirrus conditions. *Nature Geoscience* **2010,** *3*, 233.
123. Schill, G. P.; De Haan, D. O.; Tolbert, M. A., Heterogeneous Ice Nucleation on Simulated Secondary Organic Aerosol. *Environmental Science & Technology* **2014,** *48* (3), 1675-1682.
124. Wang, B. B. L., A. T.; Massoli, P.; Onasch, T. B.; Davidovits, P.; Worsnop, D. R.; Knopf, D. A., The deposition ice nucleation and immersion freezing potential of amorphous secondary organic aerosol: Pathways for ice and mixed-phase cloud formation. . *Journal of Geophysical Research: Atmospheres* **2012,** *117*, D16209.
125. Ignatius, K.; Kristensen, T. B.; Järvinen, E.; Nichman, L.; Fuchs, C.; Gordon, H.; Herenz, P.; Hoyle, C. R.; Duplissy, J.; Garimella, S.; Dias, A.; Frege, C.; Höppel, N.; Tröstl, J.; Wagner, R.; Yan, C.; Amorim, A.; Baltensperger, U.; Curtius, J.; Donahue, N. M.; Gallagher, M. W.; Kirkby, J.; Kulmala, M.; Möhler, O.; Saathoff, H.; Schnaiter, M.; Tomé, A.; Virtanen, A.; Worsnop, D.; Stratmann, F., Heterogeneous ice nucleation of viscous secondary organic aerosol produced from ozonolysis of α-pinene. *Atmos. Chem. Phys.* **2016,** *16* (10), 6495-6509.
126. Baustian, K. J.; Wise, M. E.; Jensen, E. J.; Schill, G. P.; Freedman, M. A.; Tolbert, M. A., State transformations and ice nucleation in amorphous (semi-)solid organic aerosol. *Atmos. Chem. Phys.* **2013,** *13* (11), 5615-5628.
127. Lienhard, D. M. H., A. J.; Krieger, U. K.; Rudich, Y.; Marcolli, C. Luo, B. P.; Bones, D. L.; Reid, J. P.; Lambe, A. T.; Canagaratna, M. R.; Davidovits, P.; Onasch, T. B.; Worsnop, D. R.; Steimer, S. S.; Koop, T.; Peter, T., Viscous organic aerosol particles in the upper troposphere: diffusivity-controlled water uptake and ice nucleation? *Atmos. Chem. Phys.* **2015,** *15*, 13599-13613.
128. Schill, G. P. T., M. A., Heterogeneous ice nucleation on phase-separated organic-sulfate particles: effect of liquid vs. glassy coatings. *Atmos. Chem. Phys.* **2013,** *13* (9), 4681-4695.
129. Knopf, D. A.; Alpert, P. A.; Wang, B., The Role of Organic Aerosol in Atmospheric Ice Nucleation: A Review. *ACS Earth and Space Chemistry* **2018,** *2* (3), 168-202.
130. Perraud, V.; Bruns, E. A.; Ezell, M. J.; Johnson, S. N.; Yu, Y.; Alexander, M. L.; Zelenyuk, A.; Imre, D.; Chang, W. L.; Dabdub, D.; Pankow, J. F.; Finlayson-Pitts, B. J., Nonequilibrium atmospheric secondary organic aerosol formation and growth. *Proceedings of the National Academy of Sciences* **2012,** *109* (8), 2836.
131. Zaveri, R. A. E., R. C.; Shilling, J. E.; Seinfeld, J. H., Modeling kinetic partitioning of secondary organic aerosol and size distribution dynamics: representing effects of volatility, phase state, and particle-phase reaction. . *Atmos. Chem. Phys.* **2014,** *14* (10), 5153-5181.
132. Booth, A. M.; Murphy, B.; Riipinen, I.; Percival, C. J.; Topping, D. O., Connecting Bulk Viscosity Measurements to Kinetic Limitations on Attaining Equilibrium for a Model Aerosol Composition. *Environmental Science & Technology* **2014,** *48* (16), 9298-9305.
133. Shiraiwa, M.; Yee, L. D.; Schilling, K. A.; Loza, C. L.; Craven, J. S.; Zuend, A.; Ziemann, P. J.; Seinfeld, J. H., Size distribution dynamics reveal particle-phase chemistry in organic aerosol formation. *Proceedings of the National Academy of Sciences* **2013,** *110* (29), 11746.

134. Mai, H.; Shiraiwa, M.; Flagan, R. C.; Seinfeld, J. H., Under What Conditions Can Equilibrium Gas-Particle Partitioning Be Expected to Hold in the Atmosphere? *Environ. Sci. Technol.* **2015,** *49* (19), 11485-11491.
135. Liu, P.; Li, Y. J.; Wang, Y.; Gilles, M. K.; Zaveri, R. A.; Bertram, A. K.; Martin, S. T., Lability of secondary organic particulate matter. *Proceedings of the National Academy of Sciences* **2016,** *113* (45), 12643.
136. Ye, Q.; Robinson, E. S.; Ding, X.; Ye, P.; Sullivan, R. C.; Donahue, N. M., Mixing of secondary organic aerosols versus relative humidity. *Proceedings of the National Academy of Sciences* **2016,** *113* (45), 12649.
137. Ye, Q.; Upshur, M. A.; Robinson, E. S.; Geiger, F. M.; Sullivan, R. C.; Thomson, R. J.; Donahue, N. M., Following Particle-Particle Mixing in Atmospheric Secondary Organic Aerosols by Using Isotopically Labeled Terpenes. *Chem* **2018,** *4* (2), 318-333.
138. Loza, C. L.; Coggon, M. M.; Nguyen, T. B.; Zuend, A.; Flagan, R. C.; Seinfeld, J. H., On the Mixing and Evaporation of Secondary Organic Aerosol Components. *Environmental Science & Technology* **2013,** *47* (12), 6173-6180.
139. Abramson, E.; Imre, D.; Beranek, J.; Wilson, J.; Zelenyuk, A., Experimental determination of chemical diffusion within secondary organic aerosol particles. *Physical Chemistry Chemical Physics* **2013,** *15* (8), 2983-2991.
140. Sastri, S. R. S.; Rao, K. K., A new group contribution method for predicting viscosity of organic liquids. *The Chemical Engineering Journal* **1992,** *50* (1), 9-25.
141. Song, Y. C.; Haddrell, A. E.; Bzdek, B. R.; Reid, J. P.; Bannan, T.; Topping, D. O.; Percival, C.; Cai, C., Measurements and Predictions of Binary Component Aerosol Particle Viscosity. *The Journal of Physical Chemistry A* **2016,** *120* (41), 8123-8137.
142. Maclean, A. M. B., Christopher L.; Grayson, James W.; Barsanti, Kelley; Jimenez, Jose L.; Bertram, Allan K., Mixing times of organic molecules within secondary organic aerosol particles: a global planetary boundary layer perspective. *Atmos. Chem. Phys.* **2017,** 13037-13048.
143. Nizkorodov, S. A.; Laskin, J.; Laskin, A., Molecular chemistry of organic aerosols through the application of high resolution mass spectrometry. *Physical Chemistry Chemical Physics* **2011,** *13* (9), 3612-3629.
144. Nozière, B.; Kalberer, M.; Claeys, M.; Allan, J.; D'Anna, B.; Decesari, S.; Finessi, E.; Glasius, M.; Grgić, I.; Hamilton, J. F.; Hoffmann, T.; Iinuma, Y.; Jaoui, M.; Kahnt, A.; Kampf, C. J.; Kourtchev, I.; Maenhaut, W.; Marsden, N.; Saarikoski, S.; Schnelle-Kreis, J.; Surratt, J. D.; Szidat, S.; Szmigielski, R.; Wisthaler, A., The Molecular Identification of Organic Compounds in the Atmosphere: State of the Art and Challenges. *Chemical Reviews* **2015,** *115* (10), 3919-3983.
145. Tolocka, M. P.; Jang, M.; Ginter, J. M.; Cox, F. J.; Kamens, R. M.; Johnston, M. V., Formation of Oligomers in Secondary Organic Aerosol. *Environmental Science & Technology* **2004,** *38* (5), 1428-1434.
146. Gao, S.; Ng, N. L.; Keywood, M.; Varutbangkul, V.; Bahreini, R.; Nenes, A.; He, J.; Yoo, K. Y.; Beauchamp, J. L.; Hodyss, R. P.; Flagan, R. C.; Seinfeld, J. H., Particle Phase Acidity and Oligomer Formation in Secondary Organic Aerosol. *Environmental Science & Technology* **2004,** *38* (24), 6582-6589.
147. US-EPA, *Estimation programs interface suite for microsoft windows.* US Environmental Protection Agency: Washington, DC, USA, 2012.
148. Fox, T. G., Jr.; Flory, P. J., Second-order transition temperatures and related properties of polystyrene. I. Influence of molecular weight. *J. Appl. Phys.* **1950,** *21*, 581-91.
149. Matsushima, S.; Takano, A.; Takahashi, Y.; Matsushita, Y., Precise synthesis of a series of poly(4-n-alkylstyrene)s and their glass transition temperatures. *J. Polym. Sci., Part B: Polym. Phys.* **2017,** *55* (9), 757-763.
150. Montserrat, S. C., P., The effect of the molecular weight on the glass transition temperature in amorphous poly(ethyleneterephthalate). *Polymer Bulletin* **1984,** *12*.

151. Onder, K.; Peters, R. H.; Spark, L. C., Melting and transition phenomena in some polyester-urethanes. *Polymer* **1972,** *13* (3), 133-139.
152. Papadopoulos, P.; Floudas, G.; Chi, C.; Wegner, G., Molecular dynamics of oligofluorenes: A dielectric spectroscopy investigation. *J. Chem. Phys.* **2004,** *120* (5), 2368-2374.
153. Donahue, N. M.; Epstein, S. A.; Pandis, S. N.; Robinson, A. L., A two-dimensional volatility basis set: 1. organic-aerosol mixing thermodynamics. *Atmos. Chem. Phys.* **2011,** *11* (7), 3303-3318.
154. Nakanishi, M.; Nozaki, R., Systematic study of the glass transition in polyhydric alcohols. *Phys. Rev. E: Stat., Nonlinear, Soft Matter Phys.* **2011,** *83* (5-1), 051503/1-051503/5.
155. Grayson, J. W.; Evoy, E.; Song, M.; Chu, Y.; Maclean, A.; Nguyen, A.; Upshur, M. A.; Ebrahimi, M.; Chan, C. K.; Geiger, F. M.; Thomson, R. J.; Bertram, A. K., The effect of hydroxyl functional groups and molar mass on the viscosity of non-crystalline organic and organic–water particles. *Atmos. Chem. Phys.* **2017,** *17* (13), 8509-8524.
156. White, R. P.; Lipson, J. E. G., Polymer Free Volume and Its Connection to the Glass Transition. *Macromolecules (Washington, DC, U. S.)* **2016,** *49* (11), 3987-4007.
157. van der Sman, R. G. M., Predictions of Glass Transition Temperature for Hydrogen Bonding Biomaterials. *The Journal of Physical Chemistry B* **2013,** *117* (50), 16303-16313.
158. Jathar, S. H. C., C. D.; Wexler, A. S.; Seinfeld, J. H.; Kleeman, M. J., Multi-generational oxidation model to simulate secondary organic aerosol in a 3-D air quality model. *Geoscientific Model Development* **2015,** *8* (8), 2553-2567.
159. Cappa, C. D.; Wilson, K. R., Multi-generation gas-phase oxidation, equilibrium partitioning, and the formation and evolution of secondary organic aerosol. *Atmos. Chem. Phys.* **2012,** *12* (20), 9505-9528.
160. Roos, Y., Melting and glass transitions of low molecular weight carbohydrates. *Carbohydrate Research* **1993,** *238*, 39-48.
161. Hancock, B. C. Z., G., The relationship between the glass transition temperature and the water content of amorphous pharmaceutical solids. . *Pharm. Res.* **1994,** *11*.
162. Petters, M. K., S. M., A single parameter representation of hygroscopic growth and cloud condensation nucleus activity. . *Atmos. Chem. Phys.* **2007,** *7*, 1961-1971.
163. Kuwata, M.; Zorn, S. R.; Martin, S. T., Using Elemental Ratios to Predict the Density of Organic Material Composed of Carbon, Hydrogen, and Oxygen. *Environmental Science & Technology* **2012,** *46* (2), 787-794.
164. Pajunoja, A. L., A. T.; Hakala, J.; Rastak, N.; Cummings, M. J.; Brogan, J. F.; Hao, L.; Paramonov, M.; Hong, J.; Prisle, N. L., Adsorptive uptake of water by semisolid secondary organic aerosols. *Geophys. Res. Lett.* **2015,** *42* (8), 3063-3068.
165. Angell, C. A., Liquid Fragility and the Glass Transition in Water and Aqueous Solutions. *Chem. Rev. (Washington, DC, U. S.)* **2002,** *102* (8), 2627-2649.
166. Williams, M. L.; Landel, R. F.; Ferry, J. D., The Temperature Dependence of Relaxation Mechanisms in Amorphous Polymers and Other Glass-forming Liquids. *Journal of the American Chemical Society* **1955,** *77* (14), 3701-3707.
167. Huang, D.; McKenna, G. B., New insights into the fragility dilemma in liquids. *The Journal of Chemical Physics* **2001,** *114* (13), 5621-5630.
168. O'Connell, P. A.; McKenna, G. B., Arrhenius-type temperature dependence of the segmental relaxation below Tg. *The Journal of Chemical Physics* **1999,** *110* (22), 11054-11060.
169. Metatla, N.; Soldera, A., The Vogel-Fulcher-Tamman Equation Investigated by Atomistic Simulation with Regard to the Adam-Gibbs Model. *Macromolecules (Washington, DC, U. S.)* **2007,** *40* (26), 9680-9685.
170. Rothfuss, N. E.; Petters, M. D., Characterization of the temperature and humidity-dependent phase diagram of amorphous nanoscale organic aerosols. *Phys. Chem. Chem. Phys.* **2017,** *19* (9), 6532-6545.
171. Tsonos, C.; Apekis, L.; Zois, C.; Tsonos, G., Microphase separation in ion-containing polyurethanes studied by dielectric measurements. *Acta Mater.* **2004,** *52* (5), 1319-1326.

172. Casalini, R.; Roland, C. M., Thermodynamical scaling of the glass transition dynamics. *Phys. Rev. E: Stat., Nonlinear, Soft Matter Phys.* **2004,** *69* (6-1), 062501/1-062501/3.
173. Patkowski, A.; Gapinski, J.; Meier, G., Dynamics of supercooled van der Waals liquid under pressure. A dynamic light scattering study. *Colloid Polym. Sci.* **2004,** *282* (8), 874-881.
174. Ruocco, G.; Sciortino, F.; Zamponi, F.; De Michele, C.; Scopigno, T., Landscapes and fragilities. *J. Chem. Phys.* **2004,** *120* (22), 10666-10680.
175. Richert, R.; Duvvuri, K.; Duong, L.-T., Dynamics of glass-forming liquids. VII. Dielectric relaxation of supercooled tris-naphthylbenzene, squalane, and decahydroisoquinoline. *J. Chem. Phys.* **2003,** *118* (4), 1828-1836.
176. Wang, L.-M.; Angell, C. A.; Richert, R., Fragility and thermodynamics in nonpolymeric glass-forming liquids. *J. Chem. Phys.* **2006,** *125* (7), 074505/1-074505/8.
177. Tu, W.; Chen, Z.; Li, X.; Gao, Y.; Liu, R.; Wang, L.-M., Revisiting the glass transition and dynamics of supercooled benzene by calorimetric studies. *J. Chem. Phys.* **2015,** *143* (16), 164501/1-164501/8.
178. Viciosa, M. T.; Moura Ramos, J. J.; Diogo, H. P., The Slow Relaxation Dynamics in the Amorphous Pharmaceutical Drugs Cimetidine, Nizatidine, and Famotidine. *J. Pharm. Sci.* **2016,** *105* (12), 3573-3584.
179. Baghel, S.; Cathcart, H.; Redington, W.; O'Reilly, N. J., An investigation into the crystallization tendency/kinetics of amorphous active pharmaceutical ingredients: A case study with dipyridamole and cinnarizine. *Eur. J. Pharm. Biopharm.* **2016,** *104*, 59-71.
180. Duvvuri, K.; Richert, R., Dynamics of glass-forming liquids. VI. Dielectric relaxation study of neat decahydro-naphthalene. *J. Chem. Phys.* **2002,** *117* (9), 4414-4418.
181. Martinez-Garcia, J. C.; Rzoska, S. J.; Drozd-Rzoska, A.; Starzonek, S.; Mauro, J. C., Fragility and basic process energies in vitrifying systems. *Sci. Rep.* **2015,** *5*, 8314.
182. Martinez-Garcia, J. C.; Tamarit, J. L.; Capaccioli, S.; Barrio, M.; Veglio, N.; Pardo, L. C., α-Relaxation dynamics of orientationally disordered mixed crystals composed of Cl-adamantane and CN-adamantane. *J. Chem. Phys.* **2010,** *132* (16), 164516/1-164516/10.
183. Martinez-Garcia, J. C.; Tamarit, J. L.; Rzoska, S. J.; Drozd-Rzoska, A.; Pardo, L. C.; Barrio, M., Universal critical-like scaling of dynamics in plastic crystals. *J. Non-Cryst. Solids* **2011,** *357* (2), 329-333.
184. Mermet, A.; Duval, E.; Polian, A.; Krisch, M., High-frequency dynamics of the glass former dibutylphthalate under pressure. *Phys. Rev. E: Stat., Nonlinear, Soft Matter Phys.* **2002,** *66* (3-1), 031510/1-031510/8.
185. Drozd-Rzoska, A.; Rzoska, S. J., Derivative-based analysis for temperature and pressure evolution of dielectric relaxation times in vitrifying liquids. *Phys. Rev. E: Stat., Nonlinear, Soft Matter Phys.* **2006,** *73* (4-1), 041502/1-041502/6.
186. Brand, R.; Lunkenheimer, P.; Schneider, U.; Loidl, A., Excess wing in the dielectric loss of glass-forming ethanol: A relaxation process. *Phys. Rev. B: Condens. Matter Mater. Phys.* **2000,** *62* (13), 8878-8883.
187. Omara, S. S.; Abdel Rehim, M. H.; Ghoneim, A.; Madkour, S.; Thuenemann, A. F.; Turky, G.; Schoenhals, A., Structure-Property Relationships of Hyperbranched Polymer/Kaolinite Nanocomposites. *Macromolecules (Washington, DC, U. S.)* **2015,** *48* (18), 6562-6573.
188. Rodriguez-Tinoco, C.; Rafols-Ribe, J.; Gonzalez-Silveira, M.; Rodriguez-Viejo, J., Relaxation dynamics of glasses along a wide stability and temperature range. *Sci. Rep.* **2016,** *6*, 35607.
189. Sidebottom, D. L.; Rodenburg, B. V.; Changstrom, J. R., Connecting structure and dynamics in glass forming materials by photon correlation spectroscopy. *Phys. Rev. B: Condens. Matter Mater. Phys.* **2007,** *75* (13), 132201/1-132201/4.
190. Kunal, K.; Robertson, C. G.; Pawlus, S.; Hahn, S. F.; Sokolov, A. P., Role of Chemical Structure in Fragility of Polymers: A Qualitative Picture. *Macromolecules (Washington, DC, U. S.)* **2008,** *41* (19), 7232-7238.

191. Raftopoulos, K. N.; Janowski, B.; Apekis, L.; Pielichowski, K.; Pissis, P., Molecular mobility and crystallinity in polytetramethylene ether glycol in the bulk and as soft component in polyurethanes. *Eur. Polym. J.* **2011,** *47* (11), 2120-2133.
192. Dob, A.; Paluch, M.; Sillescu, H.; Hinze, G., Dynamics in supercooled polyalcohols: Primary and secondary relaxation. *J. Chem. Phys.* **2002,** *117* (14), 6582-6589.
193. Duvvuri, K.; Richert, R., Binary Glass-Forming Materials: Mixtures of Sorbitol and Glycerol. *J. Phys. Chem. B* **2004,** *108* (29), 10451-10456.
194. Rajian, J. R.; Quitevis, E. L., Translational diffusion in sucrose benzoate near the glass transition: Probe size dependence in the breakdown of the Stokes-Einstein equation. *J. Chem. Phys.* **2007,** *126* (22), 224506/1-224506/10.
195. Chua, Y. Z.; Tylinski, M.; Tatsumi, S.; Ediger, M. D.; Schick, C., Glass transition and stable glass formation of tetrachloromethane. *J. Chem. Phys.* **2016,** *144* (24), 244503/1-244503/9.
196. Mierzwa, M.; Paluch, M.; Rzoska, S. J.; Ziolo, J., The Liquid-Glass and Liquid-Liquid Transitions of TPP at Elevated Pressure. *J. Phys. Chem. B* **2008,** *112* (34), 10383-10385.
197. Kidd, C.; Perraud, V.; Wingen, L. M.; Finlayson-Pitts, B. J., Integrating phase and composition of secondary organic aerosol from the ozonolysis of α-pinene. *Proceedings of the National Academy of Sciences* **2014,** *111* (21), 7552-7557.
198. Pajunoja, A.; Malila, J.; Hao, L.; Joutsensaari, J.; Lehtinen, K. E. J.; Virtanen, A., Estimating the Viscosity Range of SOA Particles Based on Their Coalescence Time. *Aerosol Science and Technology* **2014,** *48* (2), i-iv.
199. Jain, S.; Fischer, B. K.; Petrucci, A. G., The Influence of Absolute Mass Loading of Secondary Organic Aerosols on Their Phase State. *Atmosphere* **2018,** *9* (4).
200. Chen, Q.; Liu, Y.; Donahue, N. M.; Shilling, J. E.; Martin, S. T., Particle-Phase Chemistry of Secondary Organic Material: Modeled Compared to Measured O:C and H:C Elemental Ratios Provide Constraints. *Environmental Science & Technology* **2011,** *45* (11), 4763-4770.
201. Aiken, A. C.; DeCarlo, P. F.; Kroll, J. H.; Worsnop, D. R.; Huffman, J. A.; Docherty, K. S.; Ulbrich, I. M.; Mohr, C.; Kimmel, J. R.; Sueper, D.; Sun, Y.; Zhang, Q.; Trimborn, A.; Northway, M.; Ziemann, P. J.; Canagaratna, M. R.; Onasch, T. B.; Alfarra, M. R.; Prevot, A. S. H.; Dommen, J.; Duplissy, J.; Metzger, A.; Baltensperger, U.; Jimenez, J. L., O/C and OM/OC Ratios of Primary, Secondary, and Ambient Organic Aerosols with High-Resolution Time-of-Flight Aerosol Mass Spectrometry. *Environmental Science & Technology* **2008,** *42* (12), 4478-4485.
202. Putman, A. L.; Offenberg, J. H.; Fisseha, R.; Kundu, S.; Rahn, T. A.; Mazzoleni, L. R., Ultrahigh-resolution FT-ICR mass spectrometry characterization of α-pinene ozonolysis SOA. *Atmospheric Environment* **2012,** *46*, 164-172.
203. Surratt, J. D.; Chan, A. W. H.; Eddingsaas, N. C.; Chan, M.; Loza, C. L.; Kwan, A. J.; Hersey, S. P.; Flagan, R. C.; Wennberg, P. O.; Seinfeld, J. H., Reactive intermediates revealed in secondary organic aerosol formation from isoprene. *Proc. Natl. Acad. Sci. U. S. A.* **2010,** *107* (15), 6640-6645, S6640/1-S6640/10.
204. Lin, Y.-H.; Zhang, H.; Pye, H. O. T.; Zhang, Z.; Marth, W. J.; Park, S.; Arashiro, M.; Cui, T.; Budisulistiorini, S. H.; Sexton, K. G.; Vizuete, W.; Xie, Y.; Luecken, D. J.; Piletic, I. R.; Edney, E. O.; Bartolotti, L. J.; Gold, A.; Surratt, J. D., Epoxide as a precursor to secondary organic aerosol formation from isoprene photooxidation in the presence of nitrogen oxides. *Proc. Natl. Acad. Sci. U. S. A.* **2013,** *110* (17), 6718-6723, S6718/1-S6718/16.
205. Gaston, C. J.; Riedel, T. P.; Zhang, Z.; Gold, A.; Surratt, J. D.; Thornton, J. A., Reactive Uptake of an Isoprene-Derived Epoxydiol to Submicron Aerosol Particles. *Environ. Sci. Technol.* **2014,** *48* (19), 11178-11186.
206. Gunthe, S. S. K., S. M.; Rose, D.; Chen, Q.; Roldin, P.; Farmer, D. K.; Jimenez, J. L.; Artaxo, P.; Andreae, M. O.; Martin, S. T.; Poschl, U., Cloud condensation nuclei in pristine tropical rainforest air of Amazonia: size-resolved measurements and modeling of atmospheric aerosol composition and CCN activity. *Atmos. Chem. Phys.* **2009,** *9*, 7551-7575.

207. Lambe, A. T. O., T. B.; Massoli, P.; Croasdale, D. R.; Wright, J. P.; Ahern, A. T.; Williams, L. R.; Worsnop, D. R.; Brune, W. H.; and Davidovits, P. , Laboratory studies of the chemical composition and cloud condensation nuclei (CCN) activity of secondary organic aerosol (SOA) and oxidized primary organic aerosol (OPOA). . *Atmos. Chem. Phys.* **2011,** *11* (17), 8913-8928.
208. Petters, S. S.; Pagonis, D.; Claflin, M. S.; Levin, E. J. T.; Petters, M. D.; Ziemann, P. J.; Kreidenweis, S. M., Hygroscopicity of Organic Compounds as a Function of Carbon Chain Length and Carboxyl, Hydroperoxy, and Carbonyl Functional Groups. *The Journal of Physical Chemistry A* **2017,** *121* (27), 5164-5174.
209. Roach, P. J.; Laskin, J.; Laskin, A., Nanospray desorption electrospray ionization: an ambient method for liquid-extraction surface sampling in mass spectrometry. *Analyst (Cambridge, U. K.)* **2010,** *135* (9), 2233-2236.
210. Roach, P. J.; Laskin, J.; Laskin, A., Molecular Characterization of Organic Aerosols Using Nanospray-Desorption/Electrospray Ionization-Mass Spectrometry. *Anal. Chem. (Washington, DC, U. S.)* **2010,** *82* (19), 7979-7986.
211. Nguyen, T. B.; Nizkorodov, S. A.; Laskin, A.; Laskin, J., An approach toward quantification of organic compounds in complex environmental samples using high-resolution electrospray ionization mass spectrometry. *Analytical Methods* **2013,** *5* (1), 72-80.
212. Bateman, A. P.; Laskin, J.; Laskin, A.; Nizkorodov, S. A., Applications of High-Resolution Electrospray Ionization Mass Spectrometry to Measurements of Average Oxygen to Carbon Ratios in Secondary Organic Aerosols. *Environmental Science & Technology* **2012,** *46* (15), 8315-8324.
213. Hildebrandt Ruiz, L. P., A. L.; Cerully, K. M.; Nenes, A.; Donahue, N. M.; and Pandis, S. N., Formation and aging of secondary organic aerosol from toluene: changes in chemical composition, volatility, and hygroscopicity. . *Atmos. Chem. Phys.* **2015,** *15* (14), 8301-8313.
214. Pankow, J. F., An absorption model of gas/particle partitioning of organic compounds in the atmosphere. *Atmospheric Environment* **1994,** *28* (2), 185-188.
215. Selimovic, V. Y., R. Jl; Warneke, C.; Roberts, J. M.; de Gouw, J.; Reardon, J.; Griffith, D. W. T., Aerosol optical properties and trace gas emissions by PAX and OP-FTIR for laboratory-simulated western US wildfires during FIREX. *Atmos. Chem. Phys.* **2018,** *18* (4), 2929-2948.
216. Kiontke, A.; Oliveira-Birkmeier, A.; Opitz, A.; Birkemeyer, C., Electrospray ionization efficiency is dependent on different molecular descriptors with respect to solvent ph and instrumental configuration. *PLoS One* **2016,** *11* (12), e0167502/1-e0167502/16.
217. Raffaelli, A.; Saba, A., Atmospheric pressure photoionization mass spectrometry. *Mass Spectrom. Rev.* **2003,** *22* (5), 318-331.
218. Itoh, N.; Aoyagi, Y.; Yarita, T., Optimization of the dopant for the trace determination of polycyclic aromatic hydrocarbons by liquid chromatography/dopant-assisted atmospheric-pressure photoionization/mass spectrometry. *J. Chromatogr. A* **2006,** *1131* (1-2), 285-288.
219. Finlayson-Pitts, B. J.; Pitts, J. N., Tropospheric Air Pollution: Ozone, Airborne Toxics, Polycyclic Aromatic Hydrocarbons, and Particles. *Science* **1997,** *276* (5315), 1045.
220. Ravishankara, A. R.; Rudich, Y.; Wuebbles, D. J., Physical Chemistry of Climate Metrics. *Chemical Reviews* **2015,** *115* (10), 3682-3703.
221. Silvern, R. F.; Jacob, D. J.; Kim, P. S.; Marais, E. A.; Turner, J. R.; Campuzano-Jost, P.; Jimenez, J. L., Inconsistency of ammonium-sulfate aerosol ratios with thermodynamic models in the eastern US: a possible role of organic aerosol. *Atmos. Chem. Phys.* **2017,** *17* (8), 5107-5118.
222. Arquero, K. D.; Xu, J.; Gerber, R. B.; Finlayson-Pitts, B. J., Particle formation and growth from oxalic acid, methanesulfonic acid, trimethylamine and water: a combined experimental and theoretical study. *Phys. Chem. Chem. Phys.* **2017,** *19* (41), 28286-28301.
223. Rovelli, G.; Miles, R. E. H.; Reid, J. P.; Clegg, S. L., Hygroscopic properties of aminium sulfate aerosols. *Atmos. Chem. Phys.* **2017,** *17* (6), 4369-4385.
224. Qiu, C.; Wang, L.; Lal, V.; Khalizov, A. F.; Zhang, R., Heterogeneous Reactions of Alkylamines with Ammonium Sulfate and Ammonium Bisulfate. *Environ. Sci. Technol.* **2011,** *45* (11), 4748-4755.

225. Sauerwein, M.; Chan, C. K., Heterogeneous uptake of ammonia and dimethylamine into sulfuric and oxalic acid particles. *Atmos. Chem. Phys.* **2017,** *17* (10), 6323-6339.
226. Chu, Y.; Chan, C. K., Role of oleic acid coating in the heterogeneous uptake of dimethylamine by ammonium sulfate particles. *Aerosol Sci. Technol.* **2017,** *51* (8), 988-997.
227. LI, Y. S., M., Timescales of secondary organic aerosols to reach equilibrium. *Atmos. Chem. Phys.* **2019,** *19* (9), 5959-5971.
228. Wiegel, A. A.; Liu, M. J.; Hinsberg, W. D.; Wilson, K. R.; Houle, F. A., Diffusive confinement of free radical intermediates in the OH radical oxidation of semisolid aerosols. *Physical Chemistry Chemical Physics* **2017,** *19* (9), 6814-6830.
229. Lakey, P. S. J.; Berkemeier, T.; Krapf, M.; Dommen, J.; Steimer, S. S.; Whalley, L. K.; Ingham, T.; Baeza-Romero, M. T.; Poschl, U.; Shiraiwa, M.; Ammann, M.; Heard, D. E., The effect of viscosity and diffusion on the HO2 uptake by sucrose and secondary organic aerosol particles. *Atmos. Chem. Phys.* **2016,** *16* (20), 13035-13047.
230. You, Y.; Smith, M. L.; Song, M.; Martin, S. T.; Bertram, A. K., Liquid-liquid phase separation in atmospherically relevant particles consisting of organic species and inorganic salts. *Int. Rev. Phys. Chem.* **2014,** *33* (1), 43-77.
231. Gorkowski, K.; Donahue, N. M.; Sullivan, R. C., Emerging investigator series: determination of biphasic core-shell droplet properties using aerosol optical tweezers. *Environ. Sci.: Processes Impacts* **2018,** *20* (11), 1512-1523.
232. Song, M.; Liu, P.; Martin, S. T.; Bertram, A. K., Liquid-liquid phase separation in particles containing secondary organic material free of inorganic salts. *Atmos. Chem. Phys.* **2017,** *17* (18), 11261-11271.
233. Pohlker, C.; Wiedemann, K. T.; Sinha, B.; Shiraiwa, M.; Gunthe, S. S.; Smith, M.; Su, H.; Artaxo, P.; Chen, Q.; Cheng, Y.; Elbert, W.; Gilles, M. K.; Kilcoyne, A. L. D.; Moffet, R. C.; Weigand, M.; Martin, S. T.; Poschl, U.; Andreae, M. O., Biogenic potassium salt particles as seeds for secondary organic aerosol in the Amazon. *Science* **2012,** *337* (6098), 1075-8.
234. Vander Wall, A. C.; Lakey, P. S. J.; Rossich Molina, E.; Perraud, V.; Wingen, L. M.; Xu, J.; Soulsby, D.; Gerber, R. B.; Shiraiwa, M.; Finlayson-Pitts, B. J., Understanding interactions of organic nitrates with the surface and bulk of organic films: implications for particle growth in the atmosphere. *Environ. Sci.: Processes Impacts* **2018,** *20* (11), 1593-1610.
235. Biskos, G.; Paulsen, D.; Russell, L. M.; Buseck, P. R.; Martin, S. T., Prompt deliquescence and efflorescence of aerosol nanoparticles. *Atmos. Chem. Phys.* **2007,** *6* (12, Pt. 2), 4633-4642.
236. Romakkaniemi, S.; Haemeri, K.; Vaekevae, M.; Laaksonen, A., Adsorption of water on 8-15 nm NaCl and (NH4)2SO4 aerosols measured using an ultrafine tandem differential mobility analyzer. *J. Phys. Chem. A* **2001,** *105* (35), 8183-8188.
237. Sander, R., Compilation of Henry's law constants (version 4.0) for water as solvent. *Atmos. Chem. Phys.* **2015,** *15* (8), 4399-4981.
238. Hodas, N. Z., A.; Mui, W.; Flagan, R. C.; Seinfeld, J. H., Influence of particle-phase state on the hygroscopic behavior of mixed organic–inorganic aerosols. . *Atmos. Chem. Phys.* **2015,** *15* (9), 5027-5045.
239. Hodas, N.; Zuend, A.; Schilling, K.; Berkemeier, T.; Shiraiwa, M.; Flagan, R. C.; Seinfeld, J. H., Discontinuities in hygroscopic growth below and above water saturation for laboratory surrogates of oligomers in organic atmospheric aerosols. *Atmos. Chem. Phys.* **2016,** *16* (19), 12767-12792.
240. Zuend, A.; Seinfeld, J. H., A practical method for the calculation of liquid–liquid equilibria in multicomponent organic–water–electrolyte systems using physicochemical constraints. *Fluid Phase Equilibria* **2013,** *337*, 201-213.
241. Fast, J. D.; Berg, L. K.; Alexander, L.; Bell, D.; D'Ambro, E.; Hubbe, J.; Kuang, C.; Liu, J.; Long, C.; Matthews, A.; Mei, F.; Newsom, R.; Pekour, M.; Pinterich, T.; Schmid, B.; Schobesberger, S.; Shilling, J.; Smith, J.; Springston, S.; Suski, K.; Thornton, J. A.; Tomlinson, J.; Wang, J.; Xiao, H.; Zelenyuk, A., Overview of the HI-SCALE Field Campaign: A New Perspective on Shallow Convective Clouds. *Bulletin of the American Meteorological Society* **2018**.

242. Hanson, D. R.; McMurry, P. H.; Jiang, J.; Tanner, D.; Huey, L. G., Ambient Pressure Proton Transfer Mass Spectrometry: Detection of Amines and Ammonia. *Environ. Sci. Technol.* **2011,** *45* (20), 8881-8888.
243. Berkemeier, T.; Huisman, A. J.; Ammann, M.; Shiraiwa, M.; Koop, T.; Poeschl, U., Kinetic regimes and limiting cases of gas uptake and heterogeneous reactions in atmospheric aerosols and clouds: a general classification scheme. *Atmos. Chem. Phys.* **2013,** *13* (14), 6663-6686.
244. Fuchs, N. A.; Sutugin, A. G., High-Dispersed Aerosols. In *Topics in Current Aerosol Research*, Hidy, G. M.; Brock, J. R., Eds. Pergamon: 1971; p 1.
245. Massoli, P.; Lambe, A. T.; Ahern, A. T.; Williams, L. R.; Ehn, M.; Mikkilä, J.; Canagaratna, M. R.; Brune, W. H.; Onasch, T. B.; Jayne, J. T.; Petäjä, T.; Kulmala, M.; Laaksonen, A.; Kolb, C. E.; Davidovits, P.; Worsnop, D. R., Relationship between aerosol oxidation level and hygroscopic properties of laboratory generated secondary organic aerosol (SOA) particles. *Geophysical Research Letters* **2010,** *37* (24).
246. Pandis, S. N.; Harley, R. A.; Cass, G. R.; Seinfeld, J. H., Secondary organic aerosol formation and transport. *Atmospheric Environment. Part A. General Topics* **1992,** *26* (13), 2269-2282.
247. Robinson, E. S.; Saleh, R.; Donahue, N. M., Organic Aerosol Mixing Observed by Single-Particle Mass Spectrometry. *The Journal of Physical Chemistry A* **2013,** *117* (51), 13935-13945.